DEVELOPMENT OF MULTI-LAYERED CIRCUIT ANALOG RADAR ABSORBING STRUCTURES

A THESIS SUBMITTED TO
THE GRADUATE SCHOOL OF NATURAL AND APPLIED SCIENCES
OF
MIDDLE EAST TECHNICAL UNIVERSITY

BY

EGEMEN YILDIRIM

IN PARTIAL FULFILLMENT OF THE REQUIREMENTS
FOR
THE DEGREE OF MASTER OF SCIENCE
IN
ELECTRICAL AND ELECTRONICS ENGINEERING

MAY 2012

Approval of the thesis:

DEVELOPMENT OF MULTI-LAYERED CIRCUIT ANALOG RADAR ABSORBING STRCUTURES

submitted by **EGEMEN YILDIRIM** in partial fulfillment of the requirements for the degree of **Master of Science in Electrical and Electronics Engineering Department, Middle East Technical University** by,

Prof. Dr. Canan Özgen
Dean, Graduate School of **Natural and Applied Sciences** ________________

Prof. Dr. İsmet Erkmen
Head of Department, **Electrical and Electronics Eng. Dept.** ________________

Prof. Dr. Özlem Aydın Çivi
Supervisor, **Electrical and Electronics Eng. Dept.,METU** ________________

Examining Committee Members:

Prof. Dr. Gülbin Dural
Electrical and Electronics Eng. Dept.,METU ________________

Prof. Dr. Özlem Aydın Çivi
Electrical and Electronics Eng. Dept.,METU ________________

Prof. Dr. S. Sencer Koç
Electrical and Electronics Eng. Dept.,METU ________________

Assoc. Prof. Dr. Lale Alatan
Electrical and Electronics Eng. Dept.,METU ________________

Assoc. Prof. Dr. Vakur Behçet Ertürk
Electrical and Electronics Eng. Dept., Bilkent University ________________

Date: **16.05.2012**

I hereby declare that all information in this document has been obtained and presented in accordance with academic rules and ethical conduct. I also declare that, as required by these rules and conduct, I have fully cited and referenced all material and results that are not original to this work.

Name, Last name: Egemen YILDIRIM

Signature:

ABSTRACT

DEVELOPMENT OF MULTI-LAYERED CIRCUIT ANALOG RADAR ABSORBING STRUCTURES

Yıldırım, Egemen
M. Sc. Department of Electrical and Electronics Engineering
Supervisor: Prof. Dr. Özlem Aydın Çivi

May 2012, 157 pages

A fast and efficient method for the design of multi-layered circuit analog absorbing structures is developed. The method is based on optimization of specular reflection coefficient of a multi-layered absorbing structure comprising of lossy FSS layers by using Genetic Algorithm and circuit equivalent models of FSS layers. With the introduced method, two illustrative absorbing structures are designed with -15 dB reflectivity for normal incidence case in the frequency bands of 10-31 GHz and 5-46 GHz, respectively. To the author's knowledge, designed absorbers are superior in terms of frequency bandwidth to similar studies conducted so far in the literature. For broadband scattering characterization of periodic structures, numerical codes are developed. The introduced method is improved with the employment of developed FDTD codes to the proposed method. By taking the limitations regarding production facilities into consideration, a five-layered circuit analog absorber is designed and manufactured. It is shown that the manufactured structure is capable of 15 dB reflectivity minimization in a frequency band of 3.2-12 GHz for normal incidence case with an overall thickness of 14.2 mm.

KEYWORDS: Reflectivity Minimization, Circuit Analog RAM, Genetic Algorithm, Surface Resistance, Finite Difference Time Domain, Lossy Frequency Selective Surface

ÖZ

ÇOK KATMANLI DEVRE BENZERİ RADAR SÖNÜMLEYİCİ YAPI GELİŞTİRİLMESİ

Yıldırım, Egemen
Yüksek Lisans, Elektrik ve Elektronik Mühendisliği Bölümü
Tez Yöneticisi: Prof. Dr. Özlem Aydın Çivi

Mayıs 2012, 157 sayfa

Çok katmanlı devre benzeri radar sönümleyici yapıların tasarımı için hızlı ve verimli çalışan bir metot geliştirilmiştir. Temel olarak geliştirilen metot ile Genetik Algoritma ve frekans seçici yüzeylerin devre benzeri modelleri kullanılarak, kayıplı frekans seçici yüzeylerden oluşan çok katmanlı sönümleyici yapıların sönümleme oranı eniyileştirilmektedir. Geliştirilen metot ile, 10-31 GHz ve 5-46 GHz frekans bantlarında -15 dB yansıtıcılık değerine sahip iki ayrı sönümleyici yapı tasarlanmıştır. Yapılan literatür araştırmalarına göre, tasarlanan sönümleyici yapılar, frekans bandının genişliği açısından literatürde bulunan benzerlerine göre büyük bir üstünlük sergilemektedir. Periyodik yapıların geniş bir bant boyunca saçınım karakteristiklerini analiz etmek için nümerik kodlar geliştirilmiştir. Geliştirilen FDTD kodlarının önerilen sönümleyici yapı tasarım metodu ile birleştirilmesi sonucu tasarım algoritması bir adım ileriye taşınmıştır. Üretimsel kısıtlamalar göz önünde bulundurularak, 5 katmanlı sönümleyici bir yapı tasarlanmış ve üretimi gerçekleştirilmiştir. Üretilen 14.2 mm kalınlığındaki sönümleyici yapının 3.2-12 GHz bandı içinde 15 dB yansıtıcılık azaltım kabiliyetine sahip olduğu ölçüm sonuçları ile gösterilmiştir.

ANAHTAR KELİMELER: Yansıtıcılık azaltımı, Devre Benzeri Radar Sönümleyici Yapı, Genetik Algoritma, Yüzey Direnci, Zaman Uzayında Sonlu Farklar Yöntemi, Kayıplı Frekans Seçici Yüzey

ACKNOWLEDGEMENTS

I would like to express my sincere gratitude to my adviser, Prof. Dr. Özlem Aydın Çivi, for her guidance, support and technical suggestions throughout the study.

I would like to express my gratitude to Mr. Mehmet Erim İnal for proposing this topic to me and providing every support throughout the development of the conducted studies.

I would like to express my gratitude to Mr. Ali Lafcı and Mr. Anıl Akın Yıldız for providing support throughout the production steps of the study.

I am grateful to ASELSAN A.Ş. for the financial and technical opportunities provided for the completion of this thesis.

I would also like to express my sincere appreciation for Can Barış Top, Erdinç Erçil, Doğanay Doğan, Gökhan Üçüncü, Kadir İşeri, Kaan Temir, Damla Duygu Tekbaş, Ahmet Muaz Ateş, Görkem Akgül and Furkan Lüleci for their valuable friendship, motivation and help.

I would like to thank TÜBİTAK for providing financial support during the study.

For their understanding my spending lots of time on this work, my sincere thanks go to my family.

TABLE OF CONTENTS

CHAPTERS

LIST OF TABLES

TABLES

LIST OF FIGURES

FIGURES

LIST OF SYMBOLS

$\mu_r{}'$	real part of complex relative permittivity
$\mu_r{}''$	imaginary part of complex relative permittivity
$\epsilon_r{}'$	real part of complex relative permittivity
$\epsilon_r{}''$	imaginary part of complex relative permittivity
η_0	free space intrinsic impedance
R_s	surface resistance
Z_0	free space characteristic impedance
Z_{in}	input impedance
Z_l	load impedance
Z_s	surface impedance
k_0	free space wave number
v_p	phase velocity
λ_0	free space wavelength
λ_g	guided wavelength
μ_0	free space permeability
μ_r	relative permeability
ϵ_0	free space permittivity
ϵ_r	relative permittivity
$\|R\|$	reflection coefficient magnitude
Δt	time increment
Δx	spatial increment in x-direction
Δy	spatial increment in y-direction
Δz	spatial increment in z-direction
η	intrinsic impedance of the medium
A	surface area
C	lumped model capacitance
D	cell period
L	lumped model inductance

R	lumped model resistance
T	transmission coefficient
Y	admittance
c	speed of light in vacuum
f	frequency
k	wave number
l	physical length
t	thickness
t	time
$\tan\delta_e$	electric loss tangent
$\tan\delta_\mu$	magnetic loss tangent
w	angular frequency
B	magnetic flux density vector
D	electric flux density vector
E	electric field intensity vector
H	magnetic field intensity vector
J	current density vector
n	unit vector
Γ	reflection coefficient
α	attenuation constant
β	phase constant
γ	complex propagation constant
δ	skin depth
ρ	electric charge density
σ	bulk conductivity

CHAPTER 1

INTRODUCTION

1.1 Preface

In today’s military applications, the primary objective is to detect threats as early as possible in order to employ weapons effectively and to be undetectable to increase survivability. One side of the battle is the high technology radars; the other side is radar cross section reduction techniques.

The detectability of a target is a direct measure of its radar cross section (RCS). Strictly speaking, RCS is a measure of the ratio of reflected and incident power for an illuminated target. It is mainly related to object’s size, shape and material of construction.

Most often used radar cross section reduction techniques are shaping, passive and active cancellation, and use of radar absorbing materials as coverage for potential targets. Shaping is the first step in RCS reduction studies. The main idea behind shaping is to direct the incident energy to a direction other than the source location by designing the platform’s surfaces and edges in an appropriate manner. Especially for airborne targets, this technique is not suitable when aerodynamic considerations are taken into account. Moreover for bistatic radars, shaping may increase the probability of detection. In active and passive cancellation techniques, a secondary source is used on the target to deceive the radar. For passive cancellation, a modification on the target’s platform, may be a cavity on the surface, is employed and a secondary reflected signal is generated via this perturbation on the surface. The aim is to minimize the total reflection with the help of this secondary one which is tried to be made out of phase with respect to the main reflection. Passive cancellation is also known as impedance loading. Also in active cancellation, an auxiliary scattering is generated by the target. Instead of surface modifications as in passive cancellation, this time an oriented network including receiver and transmitter sub-units is responsible for signal generation. Knowledge of frequency, waveform, intensity and angle of arrival are extracted from the incident radiation and an out of phase signal is generated and transmitted to the direction of main threat for camouflage purposes. These passive and active cancellation techniques are both narrow-banded solutions for RCS reduction. Moreover, active cancellation is a challenging task for system configuration especially for high frequency applications.

Radar absorbing materials (RAMs) are used to reduce the reflected energy power by means of absorption. This technique is based on an arrangement of dielectric and/or magnetic materials that present appropriate impedance to the incident wave. The general idea is to establish an input impedance at the RAM surface that poses good matching and absorbing qualities, so that it can attenuate the radar wave once it enters the material. Radar absorbing materials have some advantages when compared to previous techniques, such as wideband of operation, wide range of incidence angle, flexibility and variety of design methods. On the other hand, added weight and requirement of maintenance are the major disadvantages of this technique.

The studies conducted in this thesis are mainly focused on development of a design method regarding wideband and multi-layered Circuit Analog (CA) absorber, which is a major type of radar absorbing materials. Beside the developed design approach, production and measurements of a five-layered wideband CA RAM are main contributions of this study to the literature.

1.2 Radar Absorbing Material (RAM) Classifications

Radar absorbing materials can be classified into four main categories, namely Graded Interfaces, Resonant Absorbers, Circuit Analogue RAMs and Magnetic RAMs [1].

For Graded Interface type absorbers, transition from the free space intrinsic impedance to that in the absorbing structure is employed gradually in order to reduce the reflections. Pyramidal absorbers [2], [3] and wedge shaped absorbers are well known examples of Graded Interface type absorbers, shown in Figure 1-1. In these absorbers, impedance transition is employed gradually by shaping the absorbing structure. For an acceptable degree of absorption, these absorbers should be long enough, one or more wavelengths in the direction of propagation. The need for this length makes these absorbers bulky, heavy and also fragile, although their absorption characteristics are superior among all the types, especially when frequency bandwidth and angular range of operation are the main considerations. These absorbers are most commonly used in anechoic chambers.

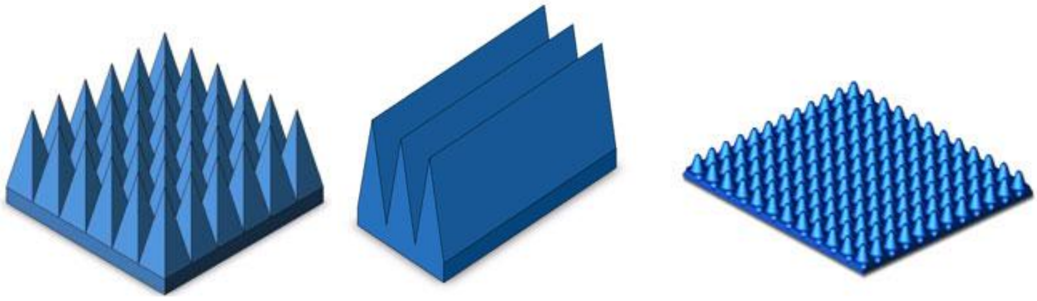

Figure 1-1 Pyramidal, wedge shaped and convoluted absorbers

Tapered Loading Absorbers are still another type of Graded Interface Absorbers. This type is typically a slab composed of a low loss material mixed with a lossy material. The ratio of mixture changes gradually from the air interface to the end of the absorber, which is shorted by a metal plate in general. Gradual change in mixture decomposition results in a gradual change of the intrinsic impedance of the absorbing medium. By this way, minimization of reflection is aimed and with enough length of the absorber, complete absorption is tried to be carried out. Since manufacturing process is very hard to realize for a continuously changing material decomposition, generally a second type which is composed of discrete homogeneous layers with increasing loading in the direction of propagation is preferred. The changing characteristic impedance for these two types is shown in Figure 1-2.

Although these absorbers could made thinner when compared to gradually shaped absorbers, thickness is still a problem and also a reproducible fabrication process is not easy to realize.

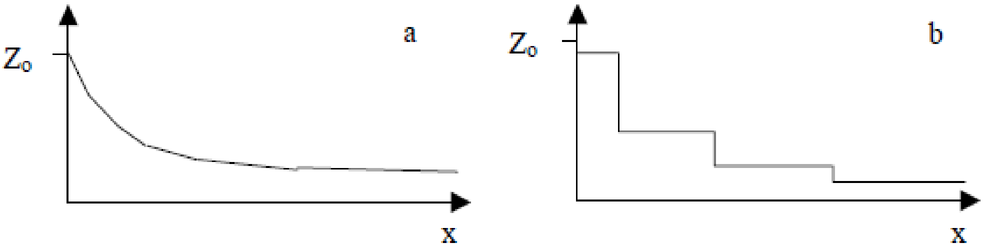

Figure 1-2 Typical Characteristic Impedance of Graded Interface Absorbers, a) smooth type b) stepped type

In resonant absorbers, different from Gradient Absorbers, the main goal is to minimize the total reflection by using multiple reflections from the absorbing structure. These absorbers are metal backed structures. When the power is incident to the material, part of the incident energy undergoes a reflection from the air interface while the remaining part penetrates into the structure. The separation between the air interface and the metal back is odd multiples of quarter wavelength at the target frequency of operation. Transmitted signal travels an effective distance of half wavelength inside the body before it reaches to the air interface back after reflection from the metal at the back of the structure. This optical distance corresponds to 180 degrees of phase shift. Meanwhile, reflection of the transmitted signal from the metal back corresponds a change in the direction of the E-field, resulting an extra phase reversal of 180 degrees. Hence the transmitted signal reaches to the air interface without a change in its phase, if we consider the periodicity of 2π. On the other hand if we consider the first reflection at the instant of incidence, there occurs a phase reversal of 180 degrees, since the incident wave is subjected to a medium whose characteristic impedance is smaller than the free space intrinsic impedance. Therefore, the reflected signal at the interface and the signal travelled in the structure will be out of phase and hence interfere in a destructive manner. If these two reflected signals have the same magnitude, then the total reflection will be zero. Salisbury Screens, Dallenbach Layers and Jaumann Absorbers are the main types of resonant absorbers.

Salisbury Screens, as shown in Figure 1-3, are composed of resistive sheet backed by a metal plate and separated usually by air with a distance of quarter wavelength at the center frequency of the absorption band, [9]. The resistance of the sheet is equal to free space intrinsic impedance, 377 ohm/sq. At the frequency in which the distance between the sheet and the metal backing corresponds to λ/4, the metal backing behaves as an open circuit, resulting an input impedance equal to that of the resistive sheet, and hence perfect absorption is realized at the center frequency. Far from the center frequency, the reflectivity characteristics degrade as shown in Figure 1-4.

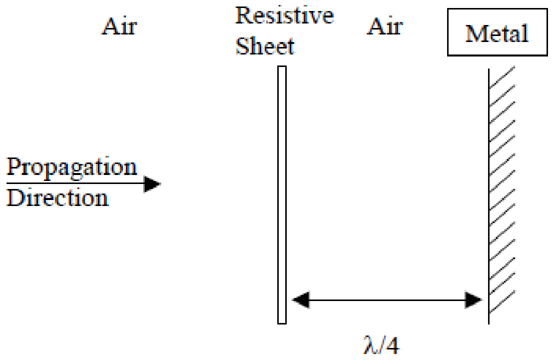

Figure 1-3 Illustration of a Salisbury Screen

As can be seen from Figure 1-4, although perfect absorption is achieved at the center frequency, the Salisbury Screens are very narrow-banded structures in terms of absorption.

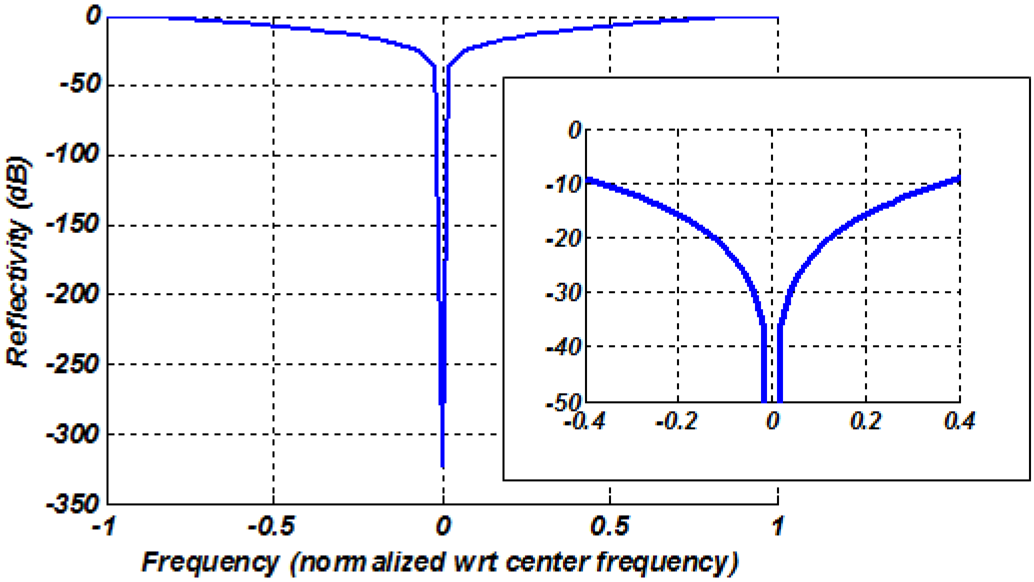

Figure 1-4 Reflectivity characteristics of a Salisbury Screen

Jaumann Layers, shown in Figure 1-5, different from Salisbury Screens, consist of more than one resistive sheets, [10], Consecutive layers are separated from each other by a distance of quarter wavelength at the center frequency.

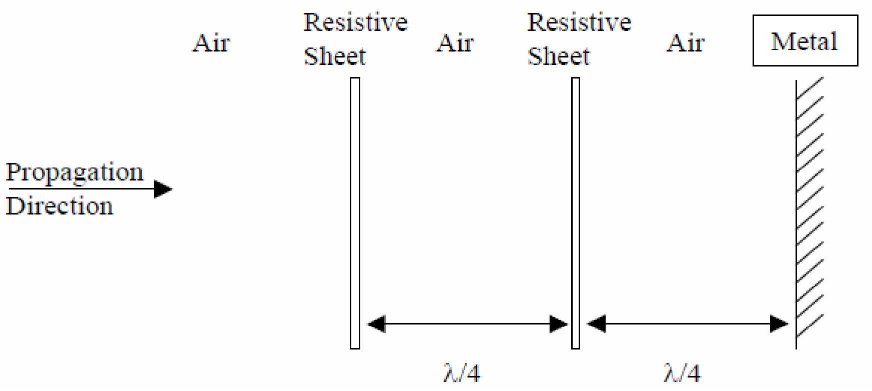

Figure 1-5 A two layered Jaumann Layer

Severin has showed that it is possible to achieve a 20 dB absorption bandwidth of one octave with 2 layers, and three octave bandwidth with 7 layers, the surface resistivity of which decreases towards the base metal plate by a constant factor from one sheet to the next [10]. A similar study has been conducted by Tuley in [15]. He has searched for achievable bandwidths with up to four layered Jaumann Absorbers. He has used quadratic resistance taper, and the spacing between the consecutive layers is quarter wavelength at the center frequency. The relationship between the number of sheets, fractional bandwidth and total thickness can be found in [15].

Even better performance is available for Jaumann absorbers with more sheets, as illustrated by a six-layer RAM in [16]. The spacing between the consecutive layers is 3.56 mm. The resistivity values for the corresponding layers are shown in Table 1-1, and the predicted reflectivity is better than -10 dB in the frequency band of 4 GHz up to 18 GHz.

Table 1-1 Resistive Sheet Values (From [16])

Resistive Sheet Values	
Layer	***Resistivity (ohm/sq.)***
Front	*9425*
2	*2513*
3	*1508*
4	*943*
5	*471*
Back	*236*

Note the large change in resistivity from front to back provided by the quadratic taper used. Besides the increased thickness, this large discrimination between the resistance values of sheets makes the absorber hard to realize.

Design process of a Jaumann Layer is based on determining the layer resistivity values. For this procedure, two analytical techniques are used, namely Maximally Flat (binomial design) and the Tschebyscheff polynomial (equal-ripple design). For these techniques to be applicable, the dielectric constant of the spacers should not be much larger than that of free space [11]. Otherwise, the techniques may come up with negative values of layer resistivity. Moreover, according to extensive numerical investigations conducted by Toit in [11], for Jaumann Absorbers with more than three layers, dielectric constant of the spacer should be smaller than a certain value which depends on the number of layers for a global optimum solution. This phenomenon is very restrictive when realizing practical multilayered absorbers owing to increased thickness. Hence, Jaumann Layers come with enhanced bandwidth when compared to Salisbury Screens at the expense of increased structure thickness.

Dallenbach Layer [12] consists of a homogeneous absorbing layer placed on a conducting plate. For reflection minimization, real and imaginary parts of both permittivity and permeability of the material together with its thickness are tried to be optimized.

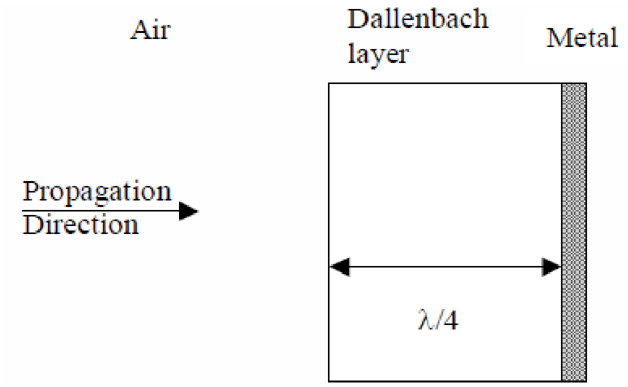

Figure 1-6 Dallenbach Layer

For a single layer Dallenbach Absorber to have wideband absorption characteristics, one of the following conditions should be satisfied by the absorbing medium [13]. The first circumstance is the equality of the permittivity and permeability values of the material together with a minimum layer thickness which depends on the operating frequency and the imaginary part of the medium’s permeability. The other condition is that the imaginary part of medium’s permeability value should be inversely proportional to the frequency. However, materials in nature do not pose such characteristics regarding their constitutive parameters and moreover, such behaviour is fundamentally impossible due to the restrictions imposed by the Kramers-Kronig relationships [13]. Taking into these considerations, in [13], Wallace has investigated the optimum bandwidth achievable with the materials satisfying Landau-Lifshitz equation, thereby restricting the corresponding constitutive parameters to values that are “reasonable” from an engineering standpoint. Under these conditions, he showed that the allowable 20 dB bandwidth is less than two and a half octaves for a single layer Dallenbach Absorber. On the other hand when more than one layer is stacked together, a 15 dB bandwidth of two decades can be obtainable by using ferrite materials [14].

Magnetic RAMs, are generally implemented by suspending carbonyl iron and ferrites in a dielectric medium, natural or synthetic rubber, ceramic materials, etc. Hence an extra degree of freedom is gained with relative permeability values other than 1+j0 when compared to dielectric absorbers. Moreover, magnetic materials, in general, tend to have high permittivity values. In other words they are not pure magnetic. Consequently, with high constitutive parameters, magnetic absorbers could be very thin when compared to dielectric absorbers, since the effective thickness of the material is much larger than its physical equivalence. This attribute of magnetic absorbers makes them attractable. The reason why magnetic RAMs are especially useful at low frequencies can be attributed to the fact that the magnetic losses are effective for low frequencies, as sketched in Figure 1-7 [15].

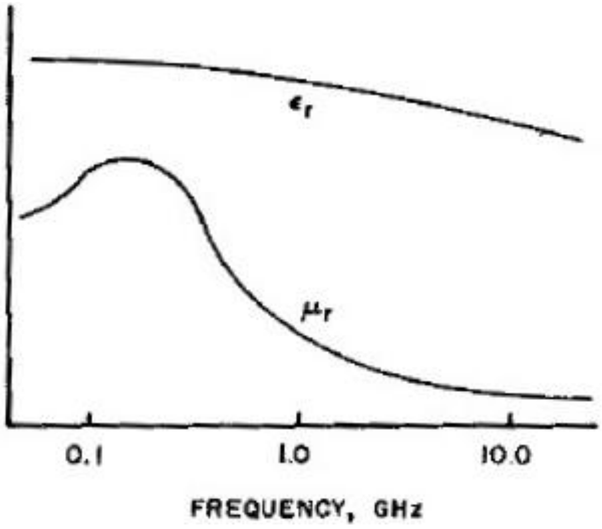

Figure 1-7 Schematic Illustration of the frequency behaviour of ferrites (From [15])

As can be seen in the Figure 1-7, permeability of the ferrites sharply decreases with increasing frequency, while permittivity tends to remain constant. As a result, at higher frequencies, magnetic losses do not contribute much to the absorption performance, and the dielectric properties now account for the corresponding losses. To clarify this point in more detail, electrical properties of a nickel-zinc ferrite are shown in Table 1-2, taken from [15]. At low frequencies, especially around 100 MHz, the electrical thickness of the material is larger than 50 times of its physical thickness owing to high constitutive parameters. Moreover since $\mu_r \approx \epsilon_r$, the reflection sourced from the air and material interface is more than 30 dB below the incident energy, giving rise to penetration of all the incident energy into the ferrite suspended material. On the other hand, with decrease in magnetic properties for higher frequencies, the electrical thickness of the material reduces together with an incline in front face reflection coefficient up to -2.1 dB with respect to incident energy at 10 GHz [15].

Table 1-2 Electrical Properties Sintered Nickel Zinc Ferrite (From [15])

	Frequency (GHz)				
	0.1	**0.5**	**1.0**	**3.0**	**10.0**
$\boldsymbol{\varepsilon_r'}$	27	24	20	18	15
$\boldsymbol{\varepsilon_r''}$	54	24	9.0	6.3	6.3
$\boldsymbol{\mu_r'}$	15	9	1.2	0.9	0.1
$\boldsymbol{\mu_r''}$	45	45	12	6.3	0.32
$\boldsymbol{\left\lvert\sqrt{\mu_r \epsilon_r}\right\rvert}$	53.5	39.5	16.3	11.0	2.3
$\boldsymbol{\lvert R\rvert}$	0.03	0.17	0.31	0.39	0.78
$\boldsymbol{\lvert R\rvert\ dB}$	-30.6	-15.4	-10.2	-8.2	-2.1

More examples for single layered magnetic absorbers can be demonstrated. In Figure 1-8, plots of reflectivity for four commercially available sintered ferrite absorbers are given, [16]. Although they are relatively heavy, they provide good absorption characteristics for low frequencies. To enhance the bandwidth achievable with magnetic absorbers, multilayered structures are preferred. The main goal is to take advantage of changes in magnetic properties between the layers. For materials such as hexagonal ferrites, the frequency at which μ_r' peaks can be controlled by doping process, [15]. By this control mechanism, different layers with distinct magnetic characteristics could be stacked to give an optimized structure in terms of absorption bandwidth. To illustrate this point, a four-layered magnetic RAM designed and optimized by Amin and James, given in [17], can be a good example. The -10 dB reflectivity band of the structure is 4 GHz up to 20 GHz, and the magnetic properties of the corresponding layers are shown in Table 1-3.

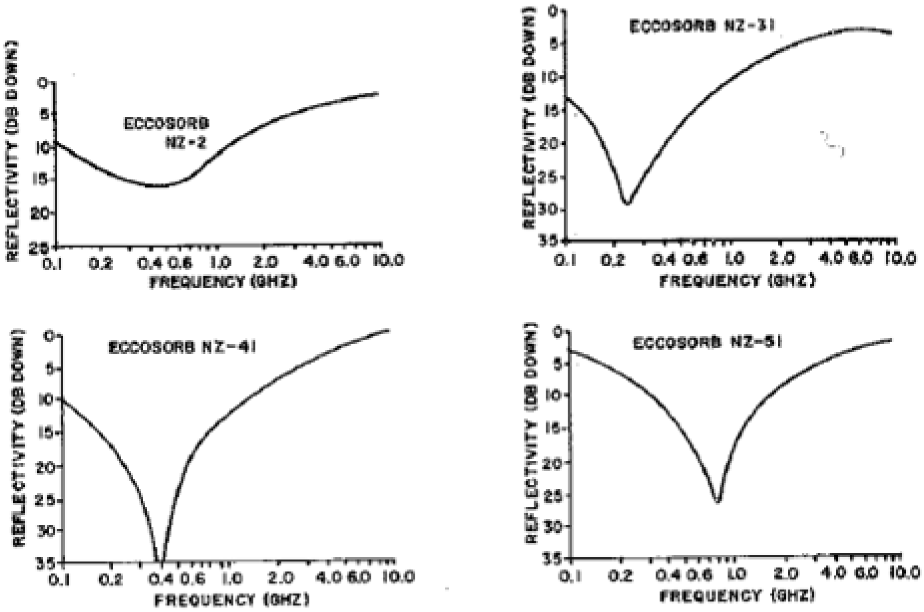

Figure 1-8 Typical sintered ferrite absorber properties (From [16])

Table 1-3 Magnetic Properties for layers of the four-layered Optimized Absorber (From [17])

Layer Number	***Resonant Frequency (GHz)***	***μ_r (peak)***	***Layer Thickness (mm)***
1	10.35	2.21	0.85
2	7.56	2.34	1.43
3	5.23	2.76	2.22
4	3.5	4.00	3.00

One of major disadvantages of magnetic RAMs is the increased weight. Still another one is the oxidation in time especially for those containing iron in some form. Also it needs improved and repeatable magnetic material production capabilities. Moreover, for applications regarding relatively high frequencies, magnetic RAMs are not suitable.

The last type of the common Radar Absorbing Materials is the Circuit Analog RAM (CA RAM). As in Salisbury Screens and Jaumann Absorbers, the main goal is to minimize the specular reflection by using the transmission line matching concepts. For the previously mentioned absorbers, loss mechanism is carried out by resistive sheets with pure real admittance values. Significant flexibility can be achieved by using resistive sheets with non-zero susceptance values. This complex admittance can be obtained by replacing the continuous resistive sheet with one whose conducting material is deposited in appropriate geometrical patterns, such as shown in Figure 1-9. These periodic patterns can be modelled with their effective inductance, capacitance and resistance values, and then the analysis and design of a Circuit Analog RAM can be carried out by using equivalent circuit techniques. This is the reason why they are known as "Circuit Analog" Absorbers.

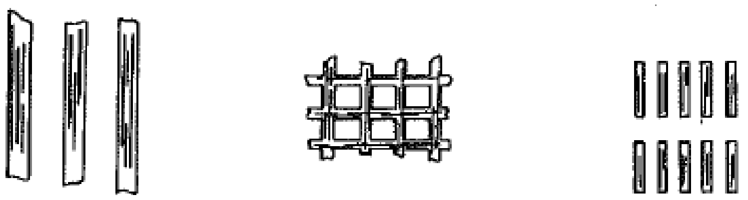

(a) STRIPS/WIRES (b) INTERSECTING WIRES (c) DIPOLES

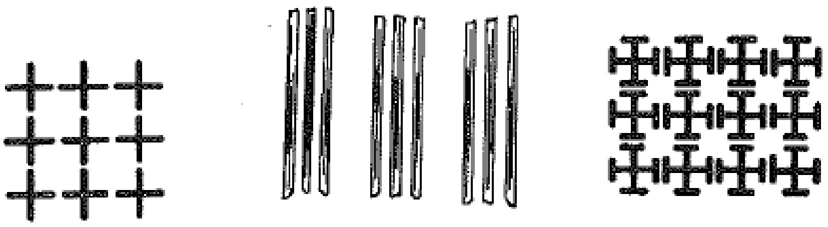

(d) CROSSED DIPOLES (e) DUAL PERIOD STRIPS (f) JERUSALEM CROSS

Figure 1-9 Typical circuit analog element geometries (From [15])

Resistive sheets, on which the conducting material deposited in geometrical patterns, have non-zero susceptance values. This susceptance value is merely determined by the shape and dimensions of the corresponding periodic pattern. This adjustable complex admittance characteristic of the lossy sheets, gives extra degree of freedom to the absorber designer and hence improved absorption characteristics together with decreased thickness values can be attainable. This claim can be testified by the studies of Alirezah and Anders conducted in 2009 [18]. They have introduced a new method, "Capacitive Circuit Method", for the design of a modified Circuit Analog Absorber which they have called as "Capacitive Circuit Absorber" (CCA) and they have compared the absorption characteristics of a one-layered CCA and the Salisbury Screen. To reveal the advantage of using geometrical patterns, they have used air as a separator for both types of absorbers. The geometrical pattern they used for the design of CCA is the square patch with a specified surface resistance value. The thickness of the ultimate one layered CCA is reduced about 27% compared to that of the Salisbury screen. Besides, comparison of frequency response of the CCA with the Salisbury screen, in [18], shows remarkable bandwidth improvement about 57%.

By the proposed design, they have verified that usage of periodic lossy patterns enhances the achievable bandwidth together with a decrease in the overall thickness. To reinforce this point, a representative single-layered RAM composed of lossy ring shaped Frequency Selective Surfaces (FSS) with an overall thickness of 5 mm can be referenced in [19]. The RAM has reflection minimization value better than -15 dB in the frequency band of 7.5-20 GHz. This performance cannot be accomplished by lightweight configurations employing optimized Jaumann screens or by other commercially available non-magnetic multilayer structures with a thickness lower than 9-10 mm.

Moreover, the bandwidth of a CA RAM can be enhanced further by increasing the number of conducting layers. With more impedance layers, designer gains more flexibility with extra control parameters resulting in improved absorption characteristics. To illustrate this point, in Figure 1-10, the frequency response of a three-layered wideband Circuit Analog Absorber designed by Alirezah and Anders is shown, [18]. The thickness of the absorber is 15.1 mm, 0.7 times the free space wavelength at center frequency. The geometrical pattern for all three conducting layers is square patch with different patch dimensions and a common period. Surface conductivities for the corresponding layers are also specified in their studies.

Although the Circuit Analog RAM is advantageous over other types of RAMs in terms of achievable bandwidth and overall thickness, optimization of variables including geometrical pattern details and surface conductivities of the lossy layers is a complicated task. Thus, current CA RAM design methodologies mostly rely on a sophisticated and usually time-consuming computer programs. Moreover, in the literature there is not much alternative method for designing multi-layered structures other than techniques using Smith Chart visualization as a matching method.

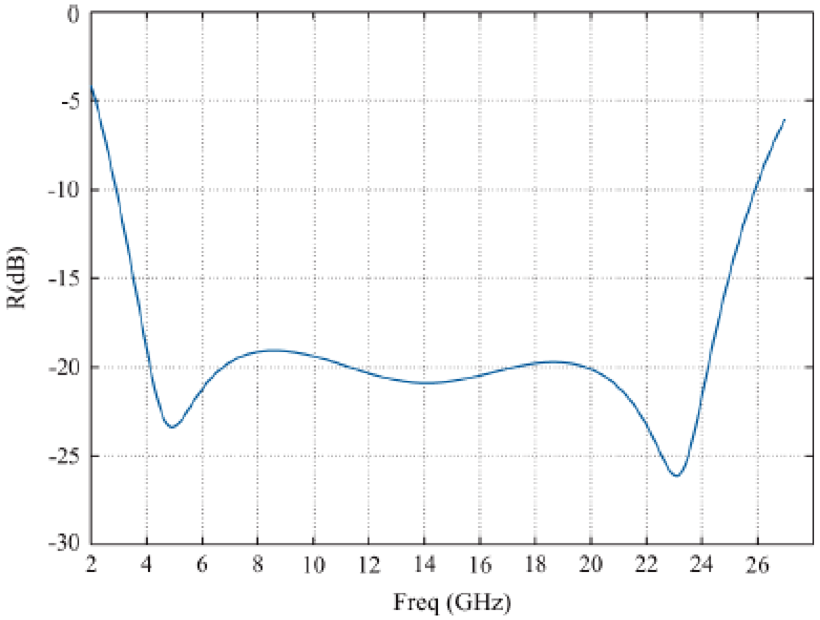

Figure 1-10 The frequency response of a three-layered capacitive circuit absorber (From [18])

1.3 Objective of the Thesis

Up to now, the types of radar absorbing materials together with their distinctive properties regarding thickness, absorption band, weight, ease of manufacture are discussed. Among the corresponding absorber types, Circuit Analog RAMs are the most favourable ones in terms of achievable bandwidth, slimness and ease of manufacture. On the other hand, in the literature, there is not adequate number of methodologies regarding multi-layered CA RAM design problem. Most of the studies concerning CA RAM design have been concentrated on discovering a geometrical pattern for single-layered structures to achieve wider bandwidths. Indeed, among the existing ones concerning multi-layered structures, it is very hard to find an efficient design method. Hence, this research is mainly devoted to develop an efficient approach for the design of a multi-layered CA RAM.

The evaluation is initiated with the introduction of the new method by explaining in a step by step manner. Illustrative examples of CA RAMs with various number of conducting layers and designed by the introduced method together with the help of full wave electromagnetic simulation tools are introduced. Absorption performance of the corresponding designs for the proposed method is compared with the CA RAM examples existing in the literature.

As a next step, an in house numerical solution code is developed for the electromagnetic characterization of periodic structures composed of lossy conductors. Then, the corresponding code is embedded into the newly introduced CA RAM design method, resulting in a compact tool for absorber design. Again, a number of CA RAMs are designed by this complete code.

For the sake of completeness of the study, a five-layered Circuit Analog RAM designed by the developed code is manufactured and consistency of the measurement results with the numerical ones is investigated.

1.4 Thesis Outline

This thesis is organized in six chapters as follows:

Chapter 2 provides an insight to the basics of Circuit Analog radar absorbing material design process. Reflection minimization techniques are explained. The fundamental blocks of a CA RAM, lossy Frequency Selective Surfaces (FSS) are introduced and impedance characterization techniques of these periodic conducting layers including full wave electromagnetic simulations are described. Common CA RAM design topologies existing in the literature are presented with illustrative designs.

In Chapter 3, a fast and efficient method for the design of multi-layered CA RAMs comprising conducting layers with arbitrary geometrical patterns is introduced. The design steps of the proposed approach are explained. Some examples of multi-layered absorbers designed by the introduced method are shown together with their reflectivity characteristics.

In Chapter 4, an in house code developed for the analysis and characterization of both single and multi-layered lossy Frequency Selective Surfaces by using Finite Difference Time Domain (FDTD) technique is described. The approximations used in the numerical solutions of the corresponding structures are explained. The verifications of the numerical codes are realized by comparing the code outputs regarding specific absorbing structures with the outputs of the full wave electromagnetic simulation tool Ansoft HFSS®, [23]. This numerical code is embedded into the introduced CA RAM design method, and to show the accuracy and efficiency of the whole technique, designed CA RAMs with altering number of layers are presented.

Chapter 5 covers the fabricated absorber design and manufacturing process with information regarding the production steps, characterization of conducting layers in free space measurement setup. Comparison and evaluation of the deviations from the designed and fabricated absorber are also discussed in scope of Chapter 5.

Finally, conclusions of this thesis work covering the future work suggestions are provided in Chapter 6.

CHAPTER 2

A CLOSER VIEW ON CIRCUIT ANALOG RADAR ABSORBING STRUCTURE DESIGN

Aim of this chapter is to give information about existing Circuit Analog RAM design methods. Before the introduction of these methods, reflection minimization topologies and periodic structure modeling techniques are explained. Related topics were examined in separate sub-chapters accordingly.

2.1 Reflection Minimization

At radar frequencies, minimization of reflection can be achieved by one of two mechanisms: (1) absorption, and (2) cancellation. Absorbing materials using cancellation technique with the help of multiple reflections inside the absorbing structure are called as resonant materials. Salisbury Screens, Jaumann Layers, Dallenbach Layers and Circuit Analog RAMs are included in this category. On the other hand, absorption technique relies on almost zero reflection at the air interface of the material for the very first reflection. After the penetration of the incident energy almost entirely into the absorbing material, attenuation is carried out by the lossy medium. Magnetic RAMs, tapered loading absorbers fall into this category.

Together with conductivity, permittivity and permeability values of the materials are responsible for the loss mechanism. When expressing these complex constitutive parameters, the relative permittivity (ε_r) and the relative permeability (μ_r) which are normalized with respect to free space values ε_0, μ_0 are used.

The complex notation for the corresponding values is normally given as

$$\varepsilon_r = \varepsilon_r{}' - j\varepsilon_r{}'' , \tag{2.1a}$$

$$\mu_r = \mu_r{}' - j\mu_r{}'' , \tag{2.1b}$$

where the real part (energy storage part) is shown as a prime, while the imaginary part (loss part) is shown as double prime.

At microwave frequencies the absorbed energy is transferred to the molecules, similar to ohmic losses for conductors. As the wave energy is transferred to the material, the molecular dipoles oscillate. They tend to orient themselves along the incident field. If the incident field changes too fast, or, the dipoles lag the impressed field variations, torque is exerted and energy is deposited in the material. The amount of loss is determined by the imaginary parts of permeability and permittivity or, equivalently, the loss tangents,

$$\tan\delta_\varepsilon = \frac{\varepsilon_r{}''}{\varepsilon_r{}'} \tag{2.2a}$$

$$\tan\delta_\mu = \frac{\mu_r{}''}{\mu_r{}'} \tag{2.2b}$$

Since they are a measure of loss in the medium, they are called as loss tangents. The loss tangent values of most materials are typically in the range of 0.001 - 0.1. So, especially for dielectric materials, attenuation owing to constitutive parameters is quite small. In the general case, the majority of loss for an electric absorber is due to the finite conductivity of the material. On the other hand, the loss for magnetic absorbers is owing to magnetization at microwave frequencies. Frequently, conduction losses are lumped together with the imaginary parts of the constitutive parameters for engineering convenience,

$$\varepsilon_r''{}_{eff} = \varepsilon_r'' + \frac{\sigma}{\omega\varepsilon_0} \tag{2.3}$$

where σ is the electrical conductivity and ω is the radian frequency. For the rest of the thesis, ε_r'' is used instead of $\varepsilon_r{}''{}_{eff}$.

In polar notation, the relative values are defined as

$$\varepsilon_r = |\varepsilon_r| e^{j\delta_\varepsilon} \tag{2.4a}$$

$$\mu_r = |\mu_r| e^{j\delta_\mu} \tag{2.4b}$$

The phase velocity of the medium with real valued constitutive parameters is

$$v_p = \frac{\omega}{\beta} = \frac{c}{\sqrt{\mu_r \varepsilon_r}} \tag{2.5}$$

where β is the wave number in the medium and c is the phase velocity in free space.

The propagation constant in the medium is,

$$\gamma = \alpha + j\beta = j\omega \frac{\sqrt{\mu_r \varepsilon_r}}{c} \tag{2.6}$$

where

$\gamma = complex\ propagation\ constant$

$\alpha = attenuation\ constant\ \left(\frac{Np}{m}\right)$

$\beta = phase\ constant\ \left(\frac{rad}{m}\right)$

$\omega = frequency\ of\ the\ excitation\ wave\ \left(\frac{rad}{\sec}\right)$

And, the intrinsic impedance of the medium is expressed in terms of ε_r and μ_r as,

$$\eta = \eta_0 \sqrt{\frac{\mu_r}{\varepsilon_r}} \tag{2.7}$$

where η_0 is the free space intrinsic impedance, which is equal to 120π, or approximately 377 Ω.

For non-resonant absorbers (Magnetic RAMs, tapered loading absorbers, etc.), the reflectivity of the structure is mostly determined by the very first reflection of the incident energy, which occurs at the material–air interface at the instant of incidence. For this type of absorbers the reflection coefficient can be written as

$$\Gamma = \frac{\eta - \eta_0}{\eta + \eta_0} \tag{2.8}$$

or, in terms of constitutive parameters of the medium

$$\Gamma = \frac{\sqrt{\frac{\mu_r}{\varepsilon_r}} - 1}{\sqrt{\frac{\mu_r}{\varepsilon_r}} + 1} \tag{2.9}$$

Hence, in order to accept the incident energy totally without any reflection, the relative permittivity and permeability values of the medium should be equal. Moreover, for a high degree of attenuation inside the material, imaginary parts of the constitutive materials should be high when compared to their real parts, in other words high loss tangent values are required for both constitutive parameters. When practical applications together with material production capabilities are taken into account, it is a very challenging task to produce materials with both desired electric and magnetic properties. Hence resonant type absorbers have always drawn the attention of designers for practical applications.

Resonant type absorbers (Salisbury Screens, Dallenbach Layers, Jaumann Layers, Circuit Analog RAMs, etc.) use the cancellation technique by employing multiple reflections inside the absorbing medium. Sources of these multiple reflections are the discontinuities inside the structure, which can be resistive sheets as well as the boundaries between discrete materials with different electromagnetic properties. For reflection coefficient calculations of these resonant absorbers, transmission line analysis together with equivalent circuit models for the lossy sheets can be used to find the effective input impedance seen at the front face of the structure.

In the scope of transmission line analysis, transformation of a load impedance by a transmitting medium with specified thickness and propagation constant is given by in [22] as follows:

$$Z_{in} = Z_c \frac{(Z_l + Z_c \tanh \gamma l)}{(Z_c + Z_l \tanh \gamma l)} \tag{2.10}$$

where

$Z_{in} = input\ impedance\ at\ the\ front\ face\ of\ the\ medium$

$Z_l = termination\ impedance\ at\ the\ end\ of\ the\ medium$

$Z_c = intrinsic\ impedance\ of\ the\ medium$

$\gamma = complex\ propagation\ constant\ of\ the\ medium$

In practical applications, the absorbing structures are backed by a metal plate to eliminate the dependence of the absorption characteristics with respect to environmental factors. In that case, a transmission line analysis can be performed to find the effective input impedance at the front face of the layer. For a flat metallic surface coated with a thin layer of dielectric material (frequently called a Dallenbach layer), the equivalent input impedance Z_{in} given by equation (2.10) can be rewritten in terms of medium's constitutive parameters as

$$Z_{in} = \eta_0 \sqrt{\frac{\mu_r}{\varepsilon_r}} \tanh(-j\gamma t\sqrt{\mu_r \varepsilon_r}) \tag{2.11}$$

where, *t* is the thickness of the dielectric coating shown in Figure 2-1.

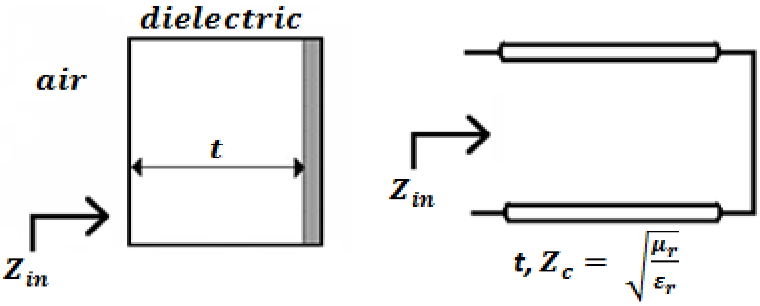

Figure 2-1 Dallenbach layer and its transmission line equivalence

To illustrate the usage of transmission line equivalence for the analysis of resonant absorbers, the equivalent circuit for the Salisbury Screen is given in Figure 2-2.

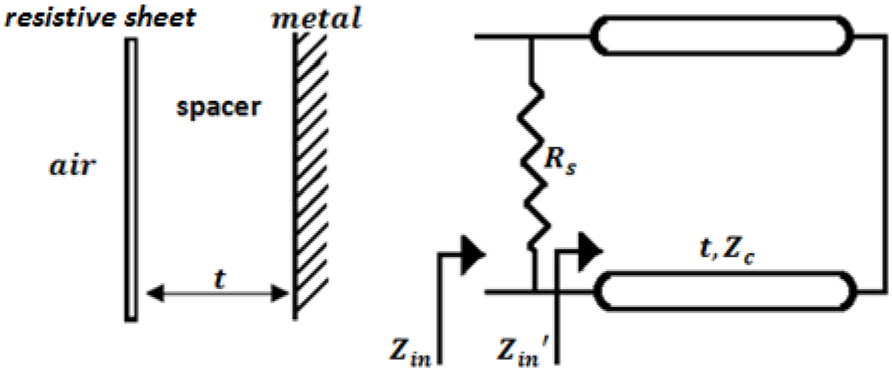

Figure 2-2 Salisbury Screen and its transmission line equivalent circuit

where

$$Z_{in}' = Z_c \tanh(\gamma t) \qquad (2.12a)$$
$$Z_{in} = Z_{in}' \,//\, R_s \qquad (2.12b)$$
$$R_s: surface\ resistance\ of\ the\ resistive\ sheet \qquad (2.12c)$$

As can be seen from Figure 2-2, the resistive sheet with a surface resistance value is modeled by a shunt resistance with the same value in the equivalent circuit model.

Surface resistance of a conductor is a function of its bulk resistivity and thickness. With the knowledge of the surface resistance, there is no need to solve electromagnetic fields inside the conductor in full wave analysis. Instead, with a simple boundary condition valid on the surface of the conductor, solution of the electromagnetic problem can be handled. However, a constant surface resistance value is valid for frequencies at which the thickness of the conductor is very thin when compared to the skin depth. For the resistive sheets used in the design of resonant absorbers, strictly speaking, since their conductivity values are very low compared to good conductors due to absorption purposes, skin depth values are large with respect to thickness of the sheets. Moreover, in order to model the sheet as a shunt component in the equivalent circuit model, the thickness already has to be thin with respect to the wavelength [15]. The skin depth of a conductor is,

$$\delta = \sqrt{\frac{2}{\omega\mu\sigma}} \tag{2.13}$$

where

σ: *conductivity of the conductor*
μ: *permeability of the conductor*
ω: *frequency of the excitation*

For thin sheets with respect to wavelength, surface resistance value can be written in terms of the conductivity and thickness of the material as follows:

$$R_s = \frac{1}{\sigma t} \tag{2.14}$$

The surface resistance boundary condition relating the electric and magnetic fields for conductors with finite conductivity values is:

$$\boldsymbol{E}_{tan} = R_s(\boldsymbol{n} \times \boldsymbol{H}_{tan}) \tag{2.15}$$

where

$\boldsymbol{n}$: *unit vector normal to the surface*
$\boldsymbol{E}_{tan}$: *the component of the E − field that is tangential to the surface*
$\boldsymbol{H}_{tan}$: *the component of the H − field that is tangential to the surface*
$\boldsymbol{R}_s$: *surface resistance in* $\frac{ohm}{sq}$

The resistance on the surface of conductors, R_s, has the unit of ohms per square (Ω/sq.). The unit Ω/sq. indicates that the surface resistance, R_s, is equal to the equivalent circuit resistance, R, measured between the edges of a *'square'* sheet of material.

For example, let a rectangle of length L and width w has a uniform current, I, applied to it. It has a voltage drop, V, across its edges and an equivalent circuit resistance of R ohms, Figure 2-3.

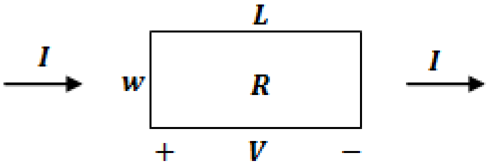

Figure 2-3 A rectangular sheet of length **L**, width **w**, and a uniform current **I** on it

If the current density, J, is uniform over the sheet then the equation (2.15)

$$E = R_s J \tag{2.16}$$

where

$E = |\boldsymbol{E}|\ on\ the\ rectangle$

$J = |\boldsymbol{J}| on\ the\ rectangle$

The circuit quantities and the fields are related to each other as:

$$V = \int_{x=0}^{L} \boldsymbol{E} \cdot \boldsymbol{dL} = EL \tag{2.17a}$$

$$I = \int_{y=0}^{w} (\boldsymbol{J} \cdot \boldsymbol{x})\, dy = Jw \tag{2.17b}$$

$$R = \frac{V}{I} = \frac{EL}{Jw} \tag{2.17c}$$

Substituting eqn. (2.16) into eqn. (2.17c) results in

$$R = R_s \frac{L}{w} \tag{2.18}$$

Thus, when $L = w$, the equivalent circuit resistance is equal to the surface resistance of the sheet. This is the reason why the unit Ω/sq is used when surface resistance is of concern [23].

For multilayered Circuit Analog absorbers, transmission line analysis together with lumped models for the lossy sheets are still valid. But this time, in order to calculate the input impedance of the absorber, more than one impedance transformation is needed, Figure 2-4.

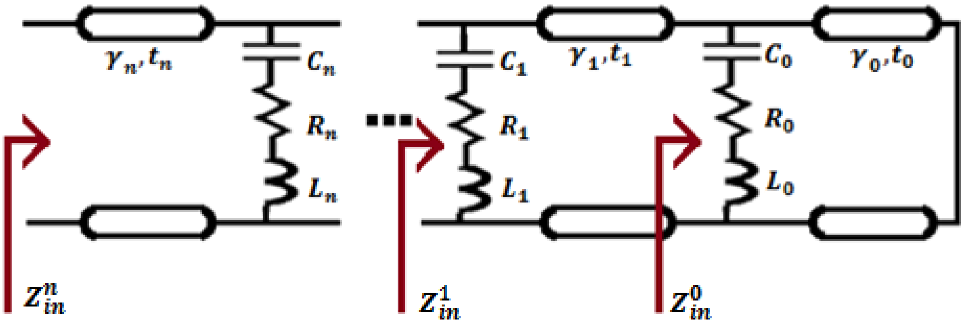

Figure 2-4 Transmission line model for an (n+1) layer Circuit Analog absorber for specular reflection case

The input impedance of the absorber can be calculated recursively as follows:

$$Z_{in}^0 = Z_l^0 \tanh(\gamma_0 t_0) \,//\, (R_0 + j\omega L_0 + \frac{1}{j\omega C_0}), \qquad (2.19a)$$

$$Z_{in}^1 = Z_l^1 \frac{(Z_{in}^0 + Z_l^1 \tanh \gamma_1 t_1)}{(Z_l^1 + Z_{in}^0 \tanh \gamma_1 t_1)} // (R_1 + j\omega L_1 + \frac{1}{j\omega C_1}), \qquad (2.19b)$$

$$\vdots$$

$$Z_{in}^n = Z_l^n \frac{(Z_{in}^{(n-1)} + Z_l^n \tanh \gamma_n t_n)}{(Z_l^n + Z_{in}^{(n-1)} \tanh \gamma_n t_n)}, \qquad (2.19c)$$

$$\Gamma = \frac{(Z_{in}^n - Z_0)}{(Z_{in}^n + Z_0)} \qquad (2.19d)$$

where

$Z_l^0, Z_l^1, \ldots, Z_{n0}^l$: $intrinsic\ impedance\ values\ of\ the\ seperating\ mediums$

Γ: $voltage\ reflection\ coefficient\ of\ the\ absorbing\ structure$

In Circuit Analog absorbers, the lossy sheets are not simple resistive sheets. Instead, the conductive material is deposited on the sheet in appropriate geometrical patterns. This patterned structure causes the equivalent impedance of the sheet used in circuit model to be complex rather than a pure resistance value. Hence most of these lossy periodic structures are modeled in the circuit analysis with a resistance, R, inductance, L, and a capacitance, C, Figure 2-5. Moreover the resistance value used in the model is different from the surface resistance value. The details of how these lossy and periodic sheets are modeled in equivalent circuits together with the determination of the corresponding model parameters will be explained in the following sub-chapter.

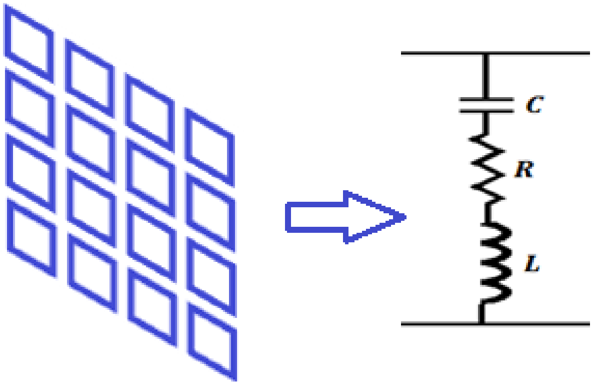

Figure 2-5 Lossy Square Loop Array and its circuit equivalent model

2.2 Circuit Equivalent Model Extraction of Conducting Periodic Sheets

As stated in the previous parts of the thesis, in Circuit Analog absorbers, absorption of the incident energy is realized by lossy sheets on which conductive material is deposited in appropriate geometrical patterns. To determine the reflectivity characteristics of the CA absorbers, these lossy sheets are modeled as lumped elements and then transmission line analysis is carried out with these circuit equivalent models. There exist two alternative methods for the extraction of the values of these lumped models. The first way is the use of analytical formulas existing in the literature for some specific Frequency Selective Surfaces.

The first study regarding the modeling of conducting periodic structures is carried out by Marcuwitz in 1951. He extracted the equivalent circuit parameters for thin, continuous, and perfectly conducting strips, [24]. But the structures he worked on are periodic in one dimension, rather than a 2D space. One of the cases he worked on is shown in Figure 2-6, the capacitive strips.

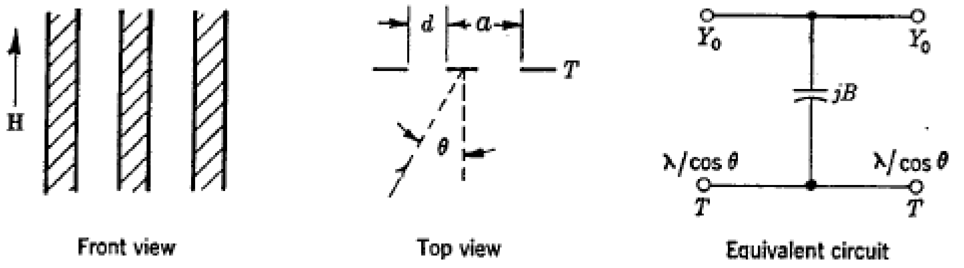

Figure 2-6 Thin, continuous, and perfectly conducting capacitive strips that Marcuwitz has modeled as lumped elements (From [24])

The value of the equivalent capacitance is given in [24]. In his studies, he also modeled the inductive strips, inductive posts and array of semi-infinite plates.

In [25], Langley and Parker have developed an equivalent circuit model for the square-loop type FSS, Figure 2-7.

In [26], Langley and Drinkwater have developed an equivalent circuit model for the Jerusalem cross, consisting of a combination of two cascaded series LC circuits, as illustrated in Figure 2-8. The details of formulas used in the calculation of reactive element values in the circuit model are given in [26].

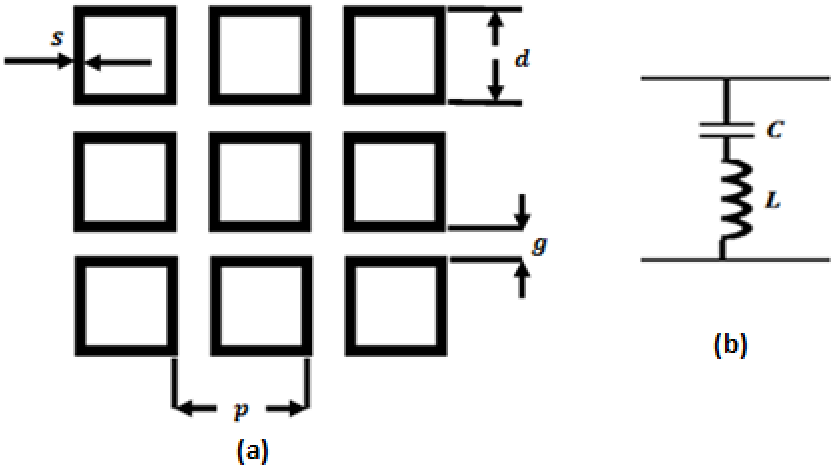

Figure 2-7 Square-loop type FSS: (a) Periodic array, (b) Equivalent circuit (From [25])

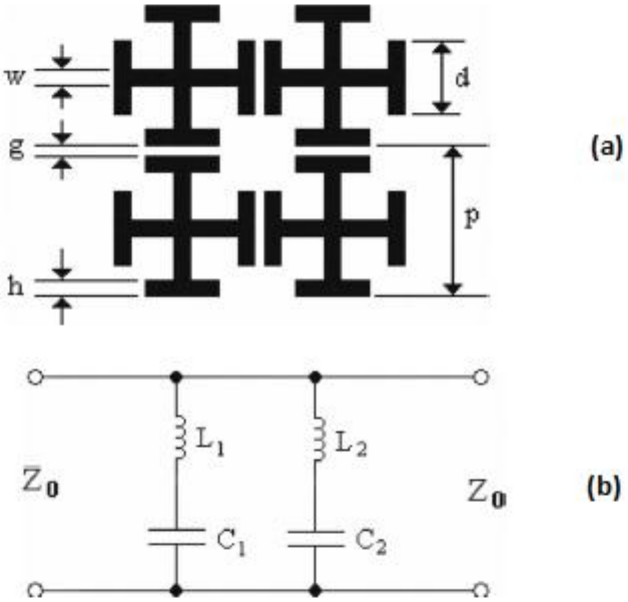

Figure 2-8 Jerusalem cross: (a) Periodic array, (b) Equivalent Circuit (From [26])

As a more specific example, the periodic arrays of double square loops, which are used for obtaining frequency selective surfaces with dual-band response, can be given. The equivalent circuit model consists of 4 reactive elements as shown in Figure 2-9. The details of analytic formulations regarding circuit equivalent parameters are given by Langley and Parker in [27].

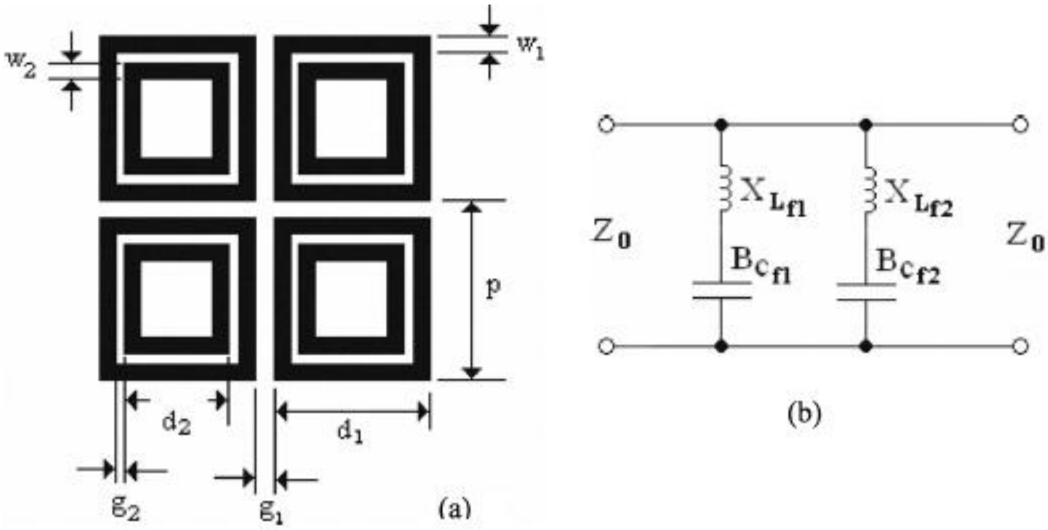

Figure 2-9 Double square loop: (a) Periodic array, (b) Equivalent circuit model (From [27])

The examples of studies concerning the analytical formulations regarding equivalent circuit modeling of frequency selective surfaces can be further extended. In [28], Savia and Parker have given the analytical modeling scheme of dipole array. Metal strips and patches have been investigated by Luukkonen, et al. in [29].

All these studies are focused on frequency selective surfaces comprising perfectly conducting metal structures. For the design of Circuit Analog absorbers, these sheets must comprise of finite conductivity materials in order to introduce attenuation to the incoming wave. The equivalent models developed for frequency selective surfaces should be modified to account for the finite conductivity. For surfaces that can be modeled by simply an inductor and a capacitor, this compensation is realized by a resistor added in series with the equivalent model. However, there is not much effort made on the analytical formulation to relate the finite conductivity with the value of lumped resistance. Roughly, the value of the resistance in the lumped model can be estimated by assuming uniform current distribution on the conducting material as follows, [19]:

$$R \approx R_s \frac{S}{A} \tag{2.20}$$

where

$S = D^2$, D $is\ the\ cell\ periodicity$

A: $effective\ surface\ area\ of\ the\ lossy\ FSS\ within\ a\ \ period$

R_s : $the\ surface\ resistance\ value\ of\ the\ lossy\ element$

R: $the\ value\ of\ the\ resistance\ used\ in\ the\ lumped\ model$

This estimation holds very well for patch type FSSs but, when resonant shapes such as rings or crosses are considered, the surface area A is represented only by the surface area of the element along the direction of the current (parallel to the incoming electric field). In a crossed dipole FSS, for instance, the corresponding area is the area of the dipole arm which is directed along the orientation of the incoming electric field. For the case of square loop type FSS, the determination of the surface area value is not well defined [19]. Furthermore, for majority of the FSS types, this surface area calculation has not been formulated. Hence exact analytical expressions regarding circuit models of frequency selective surfaces with finite conductivity are not present in the literature.

Another alternative method to determine the lumped model parameters of these periodic surfaces is the use of full wave electromagnetic solutions. Since the frequency selective surfaces are periodic in their nature, they can be modeled as infinite arrays. Hence, only a single period of the FSS, which is called as a unit cell, can be used for electromagnetic modeling. Periodic boundary conditions are used for the peripheral surfaces of the cell. In Figure 2-10, unit cell of a cross dipole array is illustrated. For the red colored dipole element, a box is drawn whose faces are the surfaces on which necessary boundary conditions are imposed.

In thesis study, for the design of Circuit Analog absorber and simulations of periodic structures, HFSS (High Frequency Structure Simulator) full wave electromagnetic solution tool is used, [30]. FEM (Finite Element Method), one of the available numeric methods provided by HFSS, is preferred for unit cell simulations. The boundary conditions and excitation of plane wave modes will be explained via screenshots of HFSS models together with the program’s own terminology.

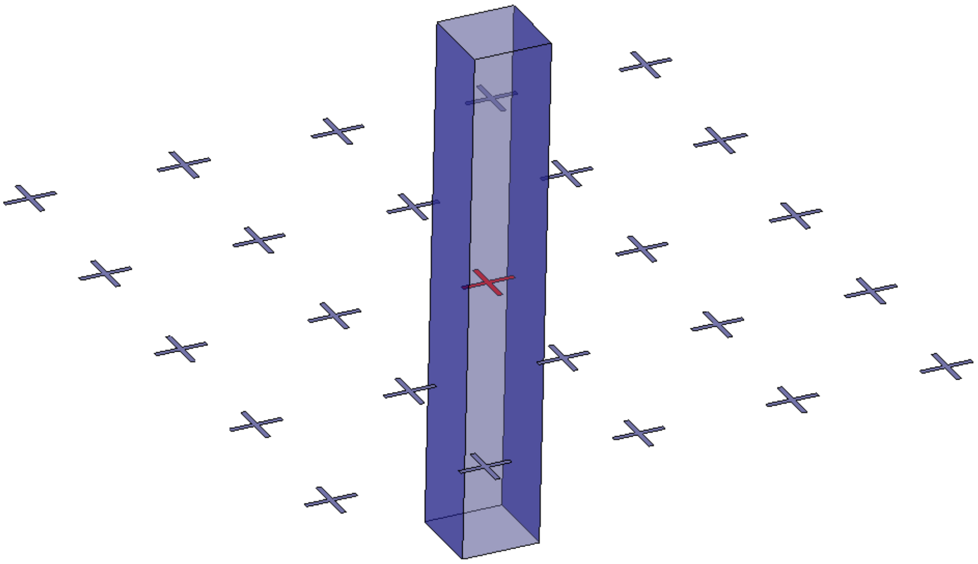

Figure 2-10 Infinite cross dipole array and unit cell for a single element

Periodicity is imposed with boundary conditions assigned on surfaces perpendicular to the plane of FSS. Periodicity in one dimension is realized by assigning ‘master’ and ‘slave’ boundaries on the surfaces facing one another and positioned perpendicular to the corresponding dimension. One dimensional periodicity together with the necessary boundary conditions is shown in Figure 2-11, a screenshot taken from HFSS.

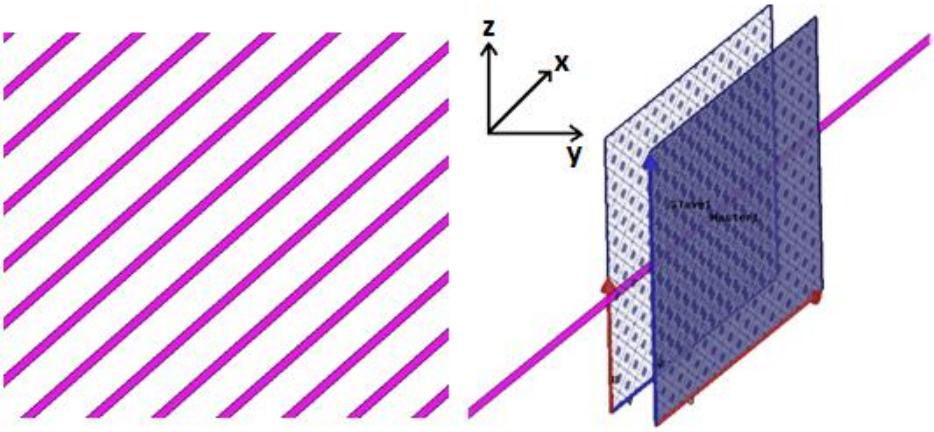

Figure 2-11 Conducting strip array with periodicity in one dimension and its unit cell equivalent

As seen from Figure 2-11, in HFSS, periodicity is imposed via using ‘master’ and ‘slave’ boundaries for the planes normal to the axis of periodicity. The use of these boundaries implies that during the solution of the electromagnetic fields, E-field on one surface matches the E-field on another to within a phase difference. They force the E-field at each point on the slave boundary match the E-field, to within a phase difference, at each corresponding point on the master boundary. The corresponding phase difference depends upon the incidence angle of the incoming wave. Let the periodicity be d, then the phase difference between the points on these surfaces and facing each other is

$$\psi = k(\boldsymbol{r_0} \cdot \boldsymbol{a_d})d \qquad (2.21a)$$

$$E_s = e^{j\psi} E_m \qquad (2.21b)$$

where

k : $wavenumber\ for\ the\ plane\ wave\ excitation$

$\boldsymbol{r_0}$: $unit\ vector\ in\ the\ direction\ of\ propagation$

$\boldsymbol{a_d}$: $unit\ vector\ from\ the\ slave\ boundary\ to\ the\ master\ boundary$

E_s : $Electric\ field\ on\ a\ point\ located\ on\ the\ slave\ boundary$

E_m : $Electric\ field\ on\ a\ point\ located\ on\ master\ boundary\ and\ exactly\ facing\ the\ one\ on\ the\ slave\ boundary$

To impose the corresponding phase difference between the points located on the two surfaces and facing each other, HFSS forces the mesh to match on each boundary. By this way point-to-point equivalence is created on the boundary surfaces.

For the case of periodicity in two dimensions, as in the case of FSS simulations, two pairs of ‘master’ and ‘slave’ boundaries are used. In Figure 2-12, the corresponding case is tried to be illustrated over a cross dipole array. Each ’master’ and ‘slave’ boundary pair is treated independently; hence a 2D infinite array can be modeled by this way.

For the electromagnetic solution of these infinite periodic arrays, at least one ‘open’ boundary condition representing the boundary to the infinite space for plane wave illumination is needed. In HFSS, to represent these boundary conditions, “Floquet” ports are used. A set of modes, “Floquet modes”, are used to represent the fields on this port boundary. These modes represent plane waves with propagation direction set by the frequency and geometry of the periodic structure. And just like the modes for the case of waveguides, these modes also have propagation constants and they experience cut-off at a sufficiently low frequency.

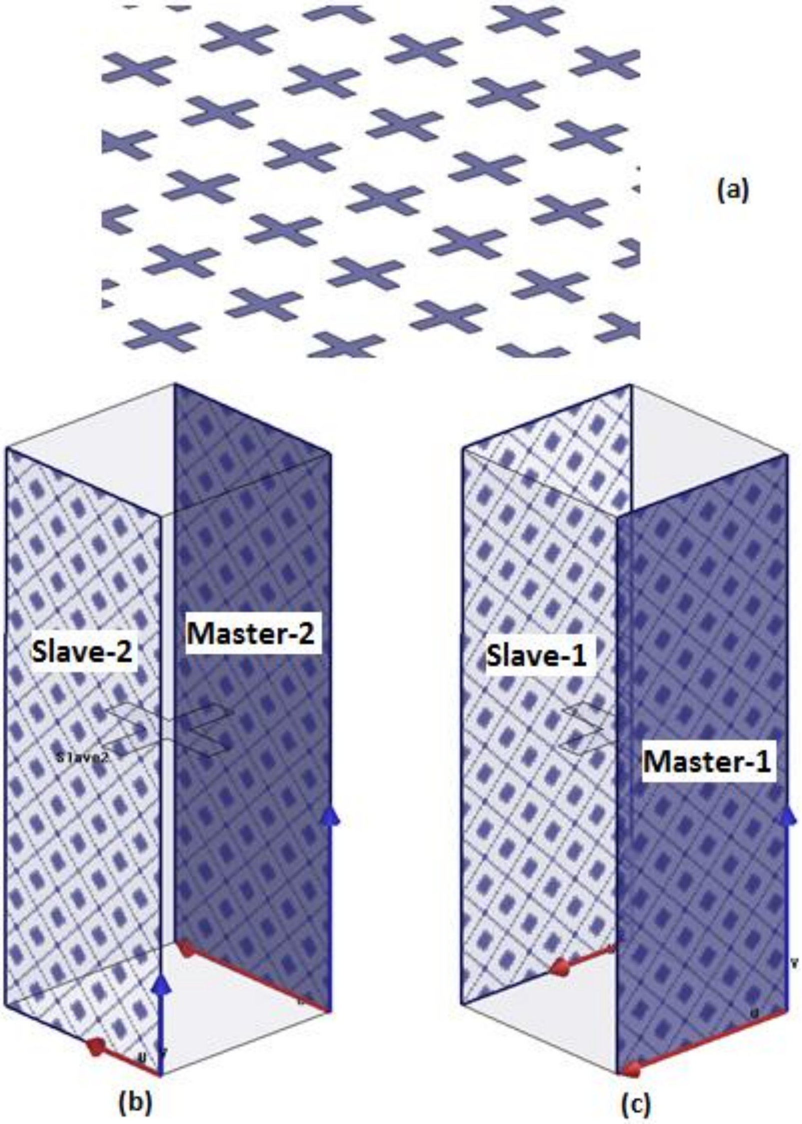

Figure 2-12 Illustration of periodicity in two dimensions: (a) infinite cross dipole array, (b) unit cell equivalent (periodicity in one dimension), (c) unit cell equivalent (periodicity in the other direction)

For simplicity, the corresponding modes will be explained by a unit cell simulation case with periodicity in one dimension. In Figure 2-13, an illustration of periodicity in one dimension is shown with master and slave boundaries separated by a distance of 1.2 wavelengths at excitation frequency.

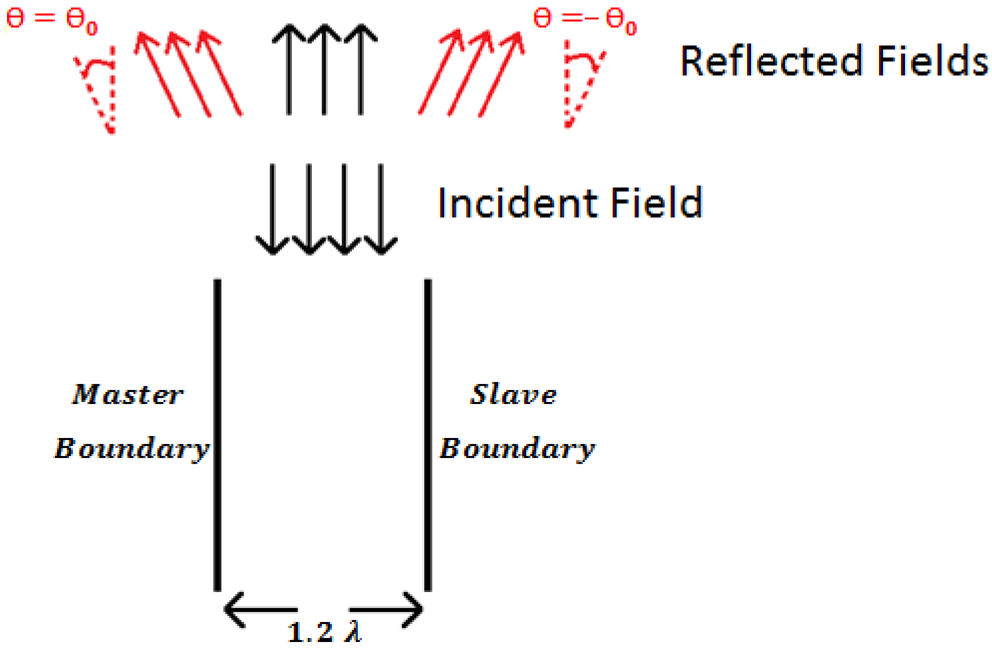

Figure 2-13 Illustration of Floquet modes over a periodicity in one dimension

In Figure 2-13, a periodic structure is illuminated with a plane wave (Incident Field) propagating in normal direction. The excitation of the frequency is such that, the periodicity is 1.2 times the wavelength at that frequency. Let the periodicity is imposed with a zero degree phase shift between the points on master and slave boundaries in order to realize the case of normal incidence. Since the simulated structure inherently has discontinuities on its surface (as in the case of FSS), when the field impinges upon this surface, it diffracts at the edges of these discontinuities. And, if the boundary conditions permit, propagations in directions different from the intended one emerge. For the illustrated case, the unintended directions are symbolized with angles of θ_0 and $-\theta_0$ with respect to surface normal. The value of

Θ_0 depends on the excitation frequency, period and imposed boundary condition, such that the following equation holds

$$kDsin(\Theta_0) = n(2\pi) + \emptyset_{imposed} \qquad (2.22a)$$

$$\Theta_0 = sin^{-1}(\frac{n(2\pi) + \emptyset_{imposed}}{kD}) \qquad (2.22b)$$

where

k: $wavenumber\ for\ the\ excitation$
D: $the\ value\ of\ the\ period$
$\emptyset_{imposed}$: $the\ intended\ direction\ of\ propagation$
n: $integer\ in\ the\ range\ of\ (-\infty\ to + \infty)$

For the illustrated case

$$\Theta_0 = sin^{-1}(\frac{n(2\pi) + 0}{\frac{2\pi}{\lambda}1.2\lambda}) = sin^{-1}(\frac{n(2\pi)}{2.4\pi})$$

for n=0 $\Theta_0 = 0^o$, which is the intended case

for n=1 $\Theta_0 = 56.44^o$

for n=-1 $\Theta_0 = -56.44^o$

Hence, the modeled structure gives chance for electromagnetic propagation in the directions of these real angle values, although the aim is to get the reflection characteristics for the case of normal incidence. As a result, reflected fields may propagate in some other directions. The plane waves propagating in these possible directions are the Floquet modes that are not exposed to attenuation. For other values of the integer 'n', the corresponding Floquet modes are in cut-off and they represents evanescent waves.

For the design of Circuit Analog absorbers, the main goal is to absorb the incident energy rather than to scatter it in other directions. Hence the designer should be aware of importance of the period determination. Let the maximum incidence angle and maximum frequency that the absorber will operate be $\Theta_{max}(in\, radians)$ and f_{max}, then the period of the structure, D, should be

$$D < \frac{2\pi - \Theta_{max}}{2\pi f_{max}\sqrt{\mu_0 \epsilon_0}} \tag{2.23}$$

In unit cell simulations, the reflection and transmission characterization of periodic structures is realized by using two Floquet ports, placed on both sides of the structure. These ports should be placed at a safe distance from the structure, to let the evanescent modes weaken sufficiently, as shown in Figure 2-14. To determine this distance, the attenuation values of the undesired higher order modes should be known. One can get these values from the HFSS, by using modes calculator property. The inputs for this evaluation are the number of modes, the frequency of interest, and the scan angles, as shown by a screenshot taken from HFSS in Figure 2-15. For the frequency value, the upper edge of the operation band which is the most probable case for the propagation of higher order modes should be entered.

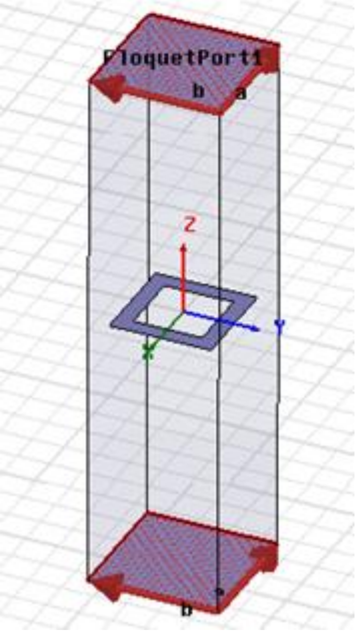

Figure 2-14 Placement of Floquet ports for rejection of undesired evanescent modes in unit cell simulations

Scan angles define the direction of intended propagation for the simulated case. For the studies conducted in the scope of thesis, the main consideration is normal incidence, hence these values are zero for theta and phi angles; note that the ports are positioned along the z-axis.

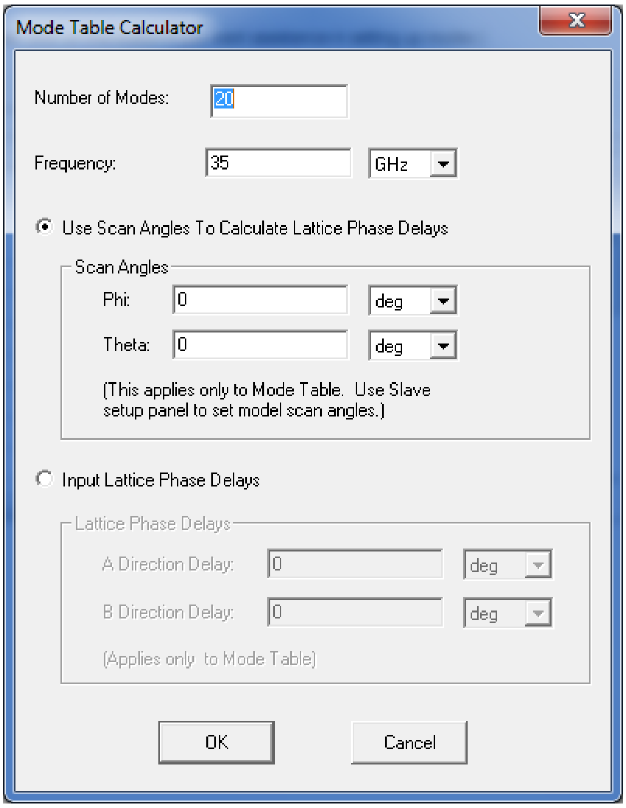

Mode Table Calculator

Number of Modes: 20

Frequency: 35 GHz

● Use Scan Angles To Calculate Lattice Phase Delays

Scan Angles

Phi: 0 deg

Theta: 0 deg

(This applies only to Mode Table. Use Slave setup panel to set model scan angles.)

○ Input Lattice Phase Delays

Lattice Phase Delays

A Direction Delay: 0 deg

B Direction Delay: 0 deg

(Applies only to Mode Table)

Figure 2-15 Modes calculator interface of the HFSS

For the number of modes, a value larger than two should be entered. According to the specified value, HFSS computes the attenuation constants for the corresponding number of modes which are most probable to propagate among all the modes. The first two modes represent the fundamental modes with parallel and perpendicular polarizations. Hence the third mode will be the first undesired mode whose attenuation constant along the surface normal is smallest in magnitude. The ports should be positioned by considering the attenuation constant of this third mode such that, at the port locations, this mode should be attenuated by a value of 40~50 dB, as a rule of thumb. For the case of an example simulation, the attenuation constants of first 12 modes are given in Figure 2-16. The attenuation constant of the most probable mode in terms of propagation is 2.44 dB, as shown in the figure. Hence to achieve an attenuation of at least 50 dB for the undesired modes, a distance of 20 mm is needed for the separation of the ports from the simulated structure.

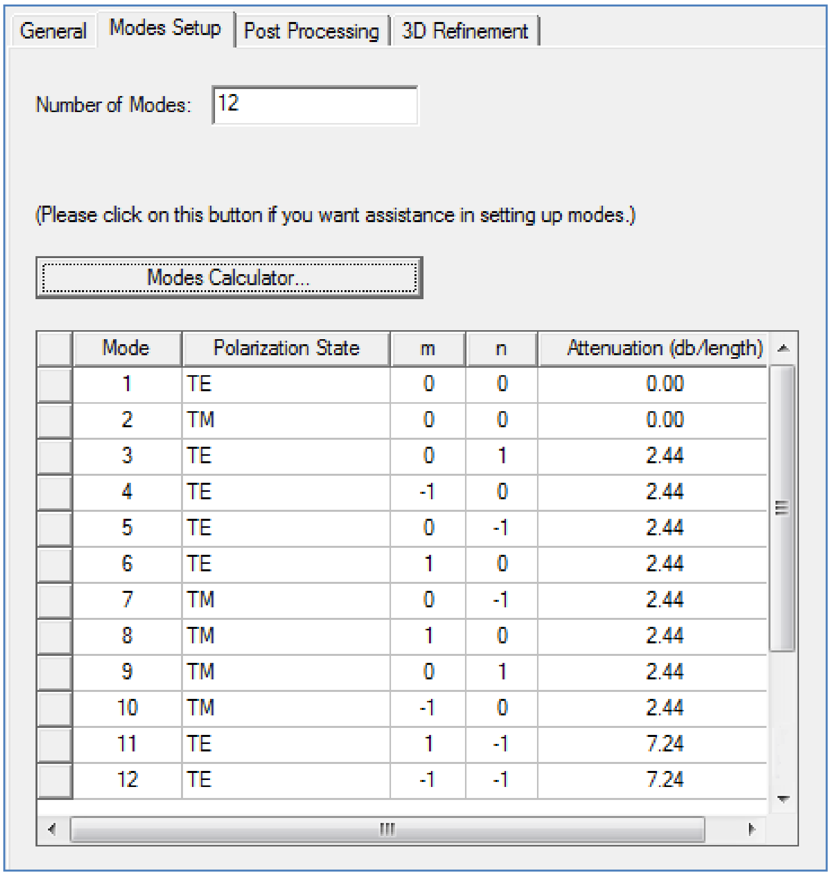

Number of Modes: 12

(Please click on this button if you want assistance in setting up modes.)

Mode	Polarization State	m	n	Attenuation (db/length)
1	TE	0	0	0.00
2	TM	0	0	0.00
3	TE	0	1	2.44
4	TE	-1	0	2.44
5	TE	0	-1	2.44
6	TE	1	0	2.44
7	TM	0	-1	2.44
8	TM	1	0	2.44
9	TM	0	1	2.44
10	TM	-1	0	2.44
11	TE	1	-1	7.24
12	TE	-1	-1	7.24

Figure 2-16 Attenuation constants of first 12 modes for an example simulation

The corresponding separation of the ports from the structure results a modification in the phase of the transmission and reflection parameters of the simulated structure, since an air line with a specified thickness is inserted between the excitation point and the structure, the structure and the observation point. Hence, this change should be compensated either by analytically (2.24a-b) or using the de-embedding property of the HFSS, shown in Figure 2-17.

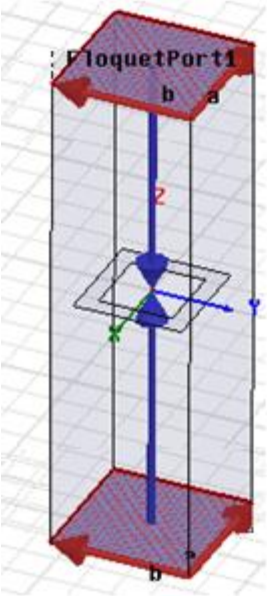

Figure 2-17 De-embedding of the S-parameters using HFSS

The circuit equivalent models of frequency selective surfaces consist of a capacitance and an inductance connected either serially or parallel. The connection type is determined by the general type of the FSS. If it is a band-pass type, then the model is represented by a parallel connection. Otherwise, if it is a band-stop type, then the corresponding connection is a serial one, Figure 2-18.

$$S_{21} = S'_{21} e^{j2kd} \qquad (2.24a)$$

$$S_{11} = S'_{11} e^{j2kd} \qquad (2.24b)$$

where

$S_{21}, S_{11}: de-embedded\ S-parameters$

$S_{21}', S_{11}': S-parameters\ of\ the\ simulated\ structure$

$d: the\ distance\ between\ the\ port\ and\ the\ FSS$

$k: the\ wave\ number$

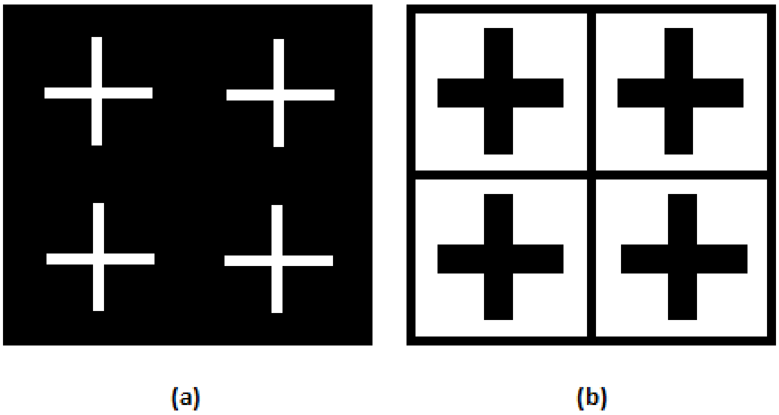

Figure 2-18 (a) Band-pass crossed dipole, (b) Band-stop crossed dipole

Band-pass frequency selective surfaces are rarely preferred for the design of circuit analog absorbers due to their high reflection characteristics. Also in the studies conducted in the scope of thesis, band-pass structures are not used. Hence the FSS types are modelled with serially connected inductors and capacitors.

By using the de-embedded S-parameters, serially connected inductance and capacitance values (LC values) for the lumped models of the FSS layers can be calculated. Firstly, the overall reactance of the shunt model of the FSS is extracted from the de-embedded S-parameters, either by using S_{11} or S_{21}, as follows:

$$Y_{shunt,t} = \frac{2(1 - S_{21})}{S_{21} Z_0} \qquad (2.25a)$$

$$Y_{shunt,r} = \frac{-2S_{11}}{Z_0(1 + S_{11})} \qquad (2.25b)$$

where

$Y_{shunt,t}$: $shunt\ model\ admittance\ extracted\ from\ transmission$

$Y_{shunt,r}$: $shunt\ model\ admittance\ extracted\ from\ reflection$

Z_0 : $characteristic\ impedance\ of\ the\ inserted\ air\ line, 376.73\ \Omega$

S_{11}, S_{21} : $de - embedded\ \ S\ parameters\ obtained\ by\ the\ unit\ cell\ simulation$

Ideally, $Y_{shunt,t}$ and $Y_{shunt,r}$ are the same. But, since the S-parameters are obtained by full wave simulation, due to numerical errors, they might differ slightly. Hence, it is more convenient to use an average shunt admittance, calculated as:

$$Y_{shunt,avg} = \frac{(Y_{shunt,t} + Y_{shunt,r})}{2} \tag{2.26}$$

By using the extracted admittance value of the shunt model, the LC values of the lumped model can be calculated by using the following equation:

$$\frac{1}{j\omega L + \frac{1}{j\omega C}} = Y_{shunt,avg} \tag{2.27}$$

Note that in the above equation, there are two unknowns namely L and C, but the known equations number is as much as the number of frequency points where the S-parameters are sampled. Therefore, this equation is an over-determined one; hence can be solved by the least squares method to get the optimum solution.

Eqn. 2.27 can be rewritten in a matrix form as:

$$\begin{bmatrix} j\omega & \frac{1}{j\omega} \end{bmatrix} * \begin{bmatrix} L_{opt} \\ \frac{1}{C_{opt}} \end{bmatrix} = \begin{bmatrix} \frac{1}{Y_{shunt,avg}} \end{bmatrix} \tag{2.28}$$

where,

$\omega \text{ and } Y_{shunt}$: $mx1 \text{ vectors } (m \text{ is the number of frequency points}),$
L_{opt}, C_{opt}: $\text{optimum } L \text{ and } C \text{ values for the lumped model of the FSS, such that}:$

$$\sum_{i=1}^{m} \left| \frac{1}{Y_{shunt,avg}(i)} - \left[j\omega(i) L_{opt} + \frac{1}{j\omega(i) C_{opt}} \right] \right|^2 , \qquad \text{is minimum.}$$

Then the solution for these optimum values is:

$$\begin{bmatrix} L_{opt} \\ \frac{1}{C_{opt}} \end{bmatrix} = \left[\begin{bmatrix} j\omega & \frac{1}{j\omega} \end{bmatrix}^H \begin{bmatrix} j\omega & \frac{1}{j\omega} \end{bmatrix} \right]^{-1} \left[\begin{bmatrix} j\omega & \frac{1}{j\omega} \end{bmatrix}^H \begin{bmatrix} \frac{1}{Y_{shunt,avg}} \end{bmatrix} \right] \tag{2.29}$$

where, the superscript ^{H} indicates complex conjugate transpose of the matrix.

2.3 Common Circuit Analog Absorber Design Techniques

In this sub-chapter, most of the Circuit Analog absorber design techniques are explained by giving examples from the literature. The advantages and disadvantages of these methodologies are discussed.

As a starting point, in [19] Costa and et al. have proposed some single-layered absorbers under narrowband and wideband classifications. For the narrowband case, they have emphasized the importance of optimum resistance value determination for the lumped model of lossy FSS layer. By using transmission line model, they have figured out a simple analytical formulation relating this optimum value to the electrical characteristics of the separating medium. And they have showed how this resistance value can be related to the surface resistance of the FSS layer. Under narrowband classification, they have designed four single-layered absorbers by using different FSS types for each structure, and they have showed the inherent narrow-band characteristics for single-layered and thin structures.

For the wideband configuration, they have designed an absorber with ring shaped FSS. Their aim is to achieve two resonances around the center frequency to achieve a wider bandwidth. To realize this characteristic, they have determined the thickness of the air slab as 5 mm, which corresponds to quarter wavelength at the center frequency. The ground plane transformed over a slab of quarter wavelength, behaves inductive at frequencies below the center frequency and capacitive for higher frequencies. With a choice of resonating FSS at center frequency also, it is possible to eliminate imaginary part of the absorber’s input impedance by achieving resonances at two points positioned at different sides of the center frequency. Moreover, if the real part of the input impedance is almost equal to free space intrinsic impedance at these points, a high degree of absorption can be achieved over a wide bandwidth. By using this approach, they have achieved -15 dB reflectivity in the frequency band of 7.5-20 GHz with their design, [19].

The methodology they used for the wideband configuration is the widely known Circuit Analog absorber design approach. The main disadvantage of this scheme is the fixed thickness of the separating slab. For lower frequency cases, this quarter wavelength thickness can be a problem for practical applications. Since multi-layered versions are out of their scope, the used approach is also not suitable for the design of multi-layered absorbers.

Another methodology for the design of wideband Circuit Analog absorber is the one proposed by Shen and et al. in [31]. They have used multiple resonances concept to achieve wide absorption bandwidths. The example absorbers they have designed are still single-layered structures. But, on a single layer, they have placed more than one conductive pattern to achieve these multiple resonances. One of the absorbers they have designed is shown in Figure 2-19. There are two dipoles in a single period with altering dimensions, and they are aimed to be effective in different frequency bands. The absorption is employed by high frequency resistors mounted between the two arms of each dipole. The -10 dB reflectivity band of the structure is 2 to 4 GHz.

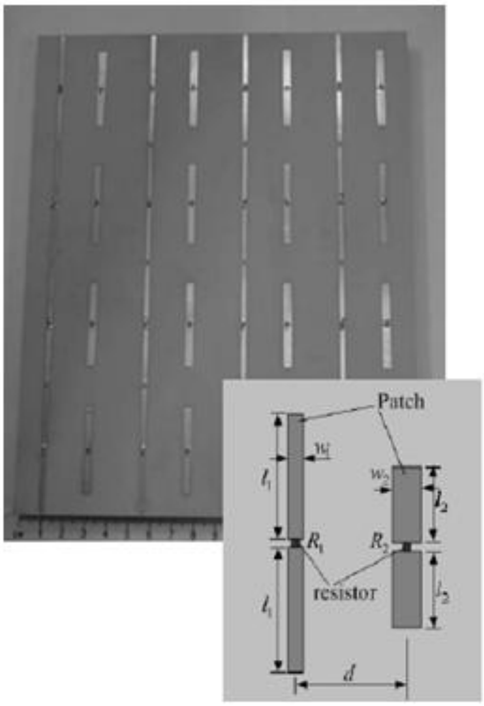

Figure 2-19 4x4 dipole array (From [31])

The main disadvantage of this approach is that the use of lumped resistors for introducing ohmic losses leads to complex and expensive structures because of the cost of high frequency resistors and complexity of manufacturing. Furthermore, this multiple resonances concept is still not applicable to multi-layered absorber design processes.

Another method for the design of Circuit Analog absorber is to use Genetic Algorithm (GA) to determine the shape of FSS layers. In this method, a single period of the FSS layer is subdivided into many number of squares with equal dimensions, and each square is assigned a value as ‘1’ or ‘0’ during the optimization process. If a square is represented by ‘1’, then it means the corresponding region is filled with conductor, otherwise it is a conductor free region as illustrated in Figure 2-20. By representing the surface with this coding scheme, optimum shape for the FSS region is tried to be found. To explain the case in more detail, an example absorber designed by Wang and et al. in [32], is discussed. The corresponding example is not a precedent for Circuit Analog absorber design in that the loss mechanism is realized by the lossy separating substrates rather than lossy FSS layers. In their work, the FSS layers are in the form of perfect conductors. The reason for the reference to this study is to illustrate the optimization of FSSs via GA. Moreover, any printed study regarding Circuit Analog absorber sheet design with the help of GA does not exist in the literature.

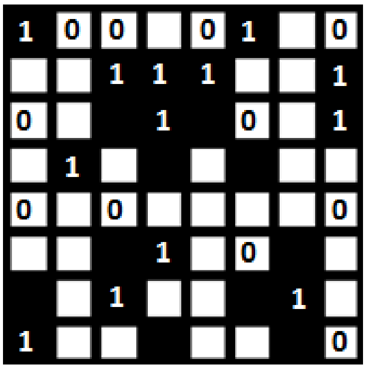

Figure 2-20 Illustration of GA binary coding scheme for a single period of an arbitrary FSS layer

In their study, Wang and et al. have designed a three-layered absorber by using the FR4 substrate with a loss tangent value of 0.025. The top-view of absorber's model together with its reflection characteristics is shown in Figure 2-21.

Although the overall thickness of the absorber is 1.28 mm, very thin when compared to in-band wavelength values, the absorption performance is not acceptable. There are frequency points in the band of operation where reflection minimization value is only 4 dB. Moreover, the bandwidth of operation is very narrow when compared to most of the absorber examples in the literature. In addition, manufacturing of these perforated structures is another problem. When all these factors come together, it can be said that use of Genetic Algorithm for optimization of periodic surfaces without any physical constraints is not an effective method.

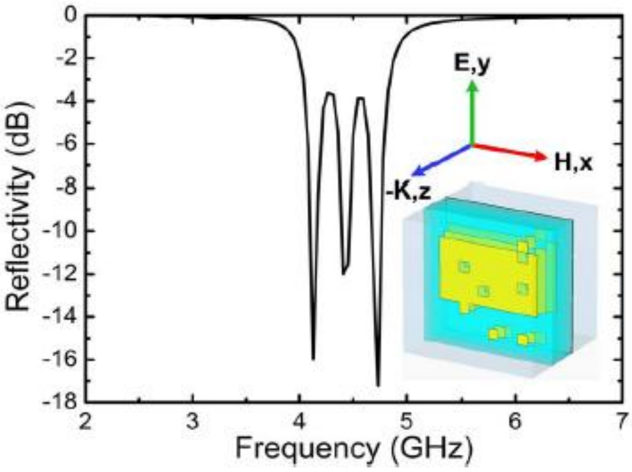

Figure 2-21 A three-layered absorber whose layers are designed by GA, and its reflectivity characteristics (From [32])

A final method from the literature and used for the design of Circuit Analog absorbers which is named after the studies conducted by Alirezah and Anders in [18], is the 'Capacitive Circuit Method'. The authors do not call the absorbers designed by this method as Circuit Analog RAM; rather they use the terminology 'Capacitive Circuit Absorber'. The reason for this refusal of common categorization is that the spacing between the layers of their absorbers is smaller than the classical separation of quarter wavelength. Moreover, in their designs, they do not use resonating elements for the FSS layers; instead they use only the square patches adjusted in proper dimensions (patch size is nearly equal to the period of the layer) to stay far away from resonance. By this way, they model the lossy patches with a capacitance and resistance. This is the origin of the terminology Capacitive Circuit Absorber'. In their study, they claim that the optimum candidate for the design of circuit analog absorber is the square patch type FSS layers with a ratio of $w/a > 0.7$, where w is the edge length of the patch and a is the period. And they have shown reflectivity characteristics of an absorber with 3 layers of square patch type FSS and a total thickness of 15.1 mm which they call as ultra-wideband absorber. The reflectivity of the absorber is shown in Figure 2-22.

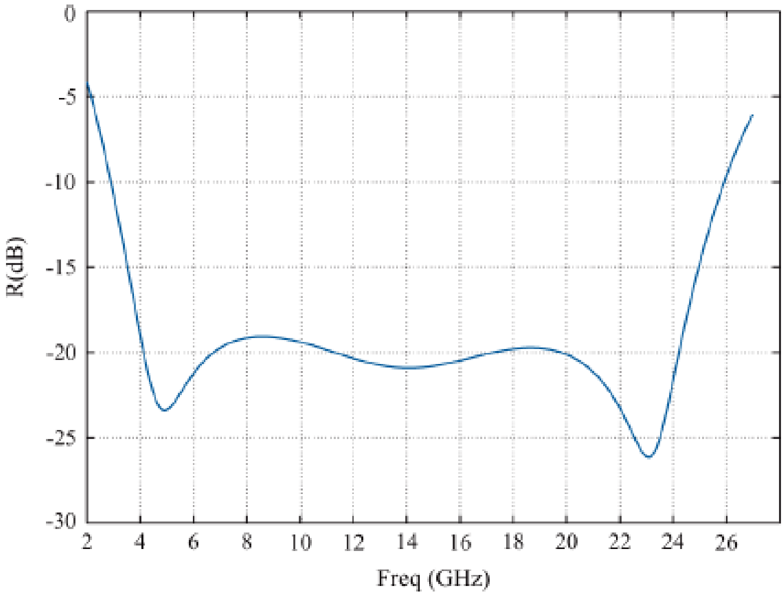

Figure 2-22 The frequency response of the ultra-wideband Capacitive Circuit absorber (From [18])

In the following chapter of the thesis, it will be shown that designs comprising of not only square patches but also other types of FSSs can have wider operation bandwidths and can be thinner. This claim will be proven by the full wave electromagnetic simulation results of a four-layered absorber with a thickness of ~ 8.8 mm and -15 dB reflectivity within the operational frequency range from 5.5 GHz to 45.5 GHz.

CHAPTER 3

A FAST AND EFFICIENT METHOD FOR THE DESIGN OF MULTI-LAYERED CIRCUIT ANALOG RAMs

In this chapter of the thesis, a novel method for the design of multi-layered absorbers is introduced, [21]. The design approach will be explained in a step by step manner over an example absorbing structure designed by the proposed method. To illustrate the efficiency of the method, an absorber with a wider operation band together with its reflection characteristics will also be presented. During the design process, at every step where full-wave electromagnetic solutions are needed, the high frequency simulation tool HFSS is used.

With the proposed methodology, it is possible to design an absorber with the following properties:

- Backed by a ground plane used to eliminate the dependence on environmental effects, as in almost all the absorber types
- Multilayered structure, without any constraint on the number of layers
- Periodic structure, a common period for all the layers
- Freedom of FSS type choice, any FSS shape can be a candidate for the conducting layers
- Degree of freedom for selection of overall thickness together with the thickness values of the separating slabs
- Degree of freedom for selection of electrical characteristics of the slabs

In addition to these characteristics, it is worth to note that the main consideration of the approach is the reflection minimization for the normal incidence case. Method can be modified for the design of absorbers with desired reflectivity characteristics under oblique incidence cases. The necessary modifications are given in Appendix A.

The proposed methodology consists of five main steps, namely:

- Design constraints determination
- Candidate FSS types characterization
- Optimization by using equivalent circuit techniques and Genetic Algorithm
- Determination of the dimensional parameters together with proper surface resistance values for each FSS layer,
- Verification of the absorber with a full wave simulation

The corresponding steps are also visualized in Figure 3-1, in a sequential order.

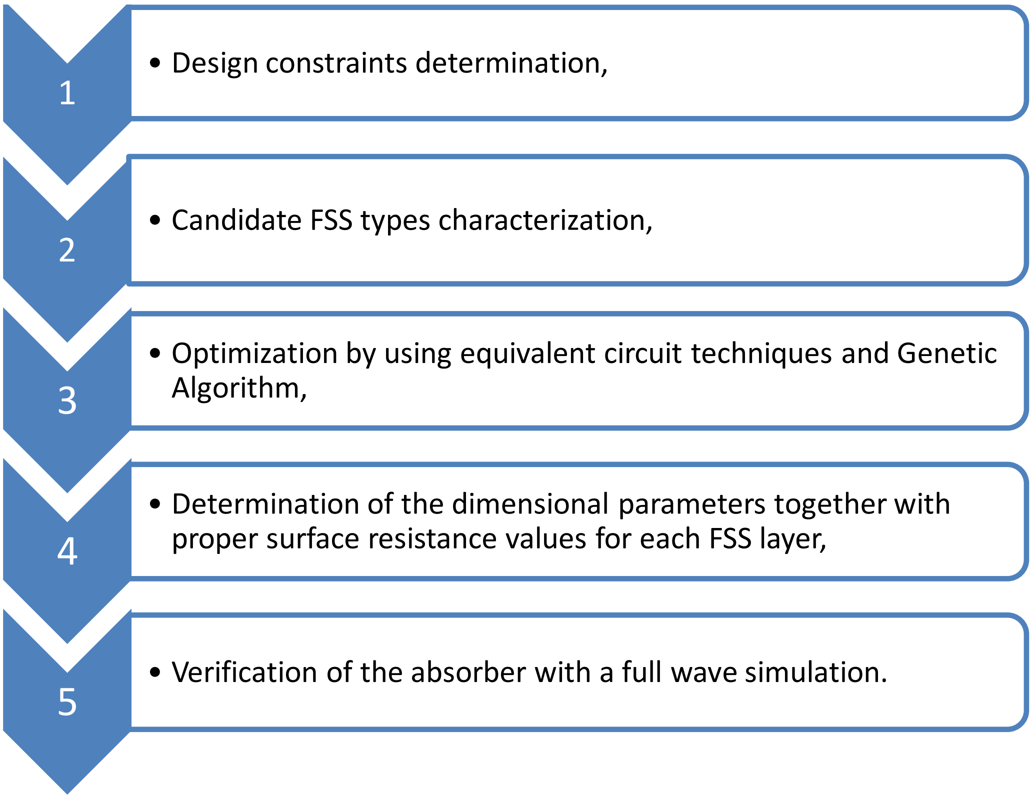

Figure 3-1 Flowchart of the proposed method

By using the proposed method, a two-layered absorber with an overall thickness of 4.6 mm and an operation band of 12 GHz to 33 GHz with a -15 dB reflectivity is designed. In the following parts of the chapter, the method is explained by covering the design steps of the mentioned absorber.

3.1 Design constraints determination

In this first step of the design process, the specifications for the absorber to be designed are determined. These specifications are:

- Frequency band of operation, and hence the common period for all the layers,
- Candidate FSS types to be used for the lossy layers,
- Maximum (or exact) thickness values for the separating slabs,
- Electrical characteristics of the separating slabs,
- Aimed reflectivity value,
- Allowable (or maximum and minimum limits) resistance values for the conducting layers.

The period determination is highly related to the aimed frequency band of operation, especially to the upper edge of the band. At this upper edge, it is more probable for the generation of undesired Floquet modes, which corresponds to waves propagating in directions different from the specular one, as explained in Chapter 2.

When the period of the absorber is large enough to make the propagation of higher order modes possible, then the decrease in the specular reflection is not solely dependent on the absorption mechanism but also the scattering of the incident energy to other directions. This phenomenon may result in an increase in the bistatic reflection coefficient; even if a further decrease for the monostatic case is observed. Hence to avoid this undesired scattering characteristics, in other words to avoid the grating lobes, the period of the structure should be smaller than the wavelength at the upper frequency edge of operation, if the normal incidence case is the only concern for angular operation region.

For the example absorber design, the target band of operation is chosen as from 10 GHz up to 35 GHz. At 35 GHz, the wavelength is 8.56 mm. Hence the period is determined to be 8 mm, which is lower than this wavelength value.

Candidate FSS types to be used are chosen as square patch, crossed dipole and square ring, shown in Figure 3-2.

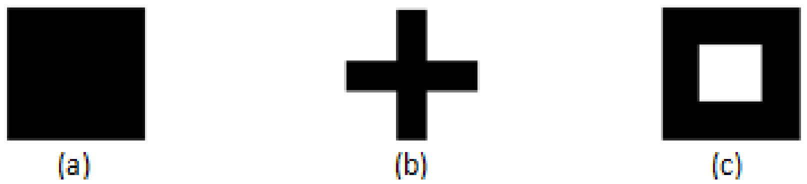

Figure 3-2 Candidate FSS types for the designed absorber: (a) square patch, (b) crossed dipole, (c) square ring

Since the design example is a conceptual one, the separating slabs are modelled as air; hence their relative permeability and permittivity values are kept as 1. Furthermore, to design a thin absorber, upper bound for the thickness values of these slabs are chosen as 2.4 mm, while lower bound is specified as 0.4 mm to avoid any unpredictable effects such as creation of a capacitance between closely positioned FSS layers. The target reduction value for the reflectivity of the absorber is defined as 15 dB, and the allowable lumped resistance limits are specified as 50 Ω and 1500 Ω, for the lower and upper bounds respectively. Note that these resistance values are different from the surface resistance values for the conducting layers. They are the bounds for the lumped resistor values to be used in circuit equivalence models. These lumped resistance values will be interrelated with the surface resistances after the proper FSS types and their corresponding dimensions are determined.

3.2 Candidate FSS types characterization

In this step, characterization of the candidate FSS types either by using full wave simulation tools or existing analytical formulations is realized. In Chapter 2, most of these existing analytical formulations are mentioned and referred to the corresponding studies in the literature. This characterization step is based on generation of a coarse look-up table relating the LC model parameters of each FSS type to the altering FSS dimensions, which will be useful in the fourth step of the design process. During this characterization, frequency selective surfaces are modelled as perfectly conducting layers. The aim is to extract upper and lower limits for the LC parameters of their lumped models. These limits will be used in the succeeding step as boundaries of the search area for layers' optimum reactance values.

For the example absorber, the LC characterizations of the chosen three FSS types are realized by using unit cell simulation in HFSS, according to the techniques explained in Chapter2. The unit cell simulation models for the three FSS types are shown in Figure 3-3.

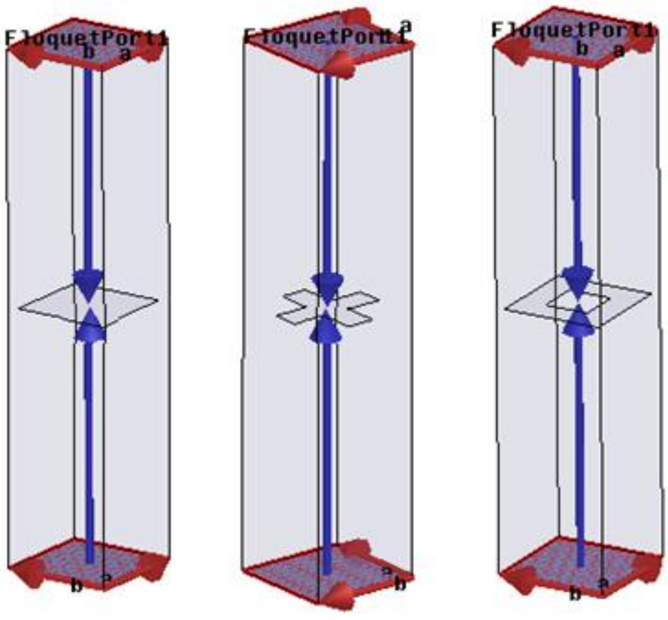

(a) (b) (c)

Figure 3-3 HFSS Simulation models for the candidate FSS types: (a) square patch, (b) crossed dipole, (c) square ring

If the separating slabs for the absorber to be designed are not air lines, there are two alternative methods for candidate FSS types' characterizations. The first one is to model the surrounding medium in the unit cell simulations with the corresponding material characteristics. The other method is to use analytical formulas existing for some specific FSS types and used to convert LC parameters obtained for free standing case in air to the case where FSS is embedded into the corresponding dielectric medium, [20].

By using the S-parameters of the simulated models, the optimum LC representation of the frequency selective surfaces is realized with the equations 2.24 to 2.28 given in Chapter 2. The extracted L and C values for altering dimensions of the surfaces are given in Table 3-1, Table 3-2 and Table 3-3 for the cases of square patch, square ring and crossed dipole, respectively.

As can be seen from Table 3-1, as the edge length of the square patch increases the surface becomes highly capacitive. The decrease in the inductance value can be related to the widening of the patch strips, since thinner conductors behave more inductive with respect to the wider ones. The increase in the capacitance is owing to the decrease in the air gap between the adjacent patches. Similarly for the case of square ring, Table 3-2, the general tendency is decrease in the inductance as the width of the ring increases. An increase in the length of the ring edges results in an incline in the capacitance. The case is similar also for the crossed dipole type FSS, Table 3-3.

Table 3-1 Lumped model characterization of the square patch FSS with a period of 8mm

patch width	L_{opt}	C_{opt}
3 mm	*2.89 nH*	*6.79 fF*
3.6 mm	*2.48 nH*	*7.07 fF*
4.2 mm	*1.68 nH*	*11.52 fF*
4.8 mm	*1.06 nH*	*18.84 fF*
5.4 mm	*0.66 nH*	*28.51 fF*
6 mm	*0.41 nH*	*39.86 fF*
6.6 mm	*0.20 nH*	*63.25 fF*
7.2 mm	*0.08 nH*	*100.22 fF*
7.8 mm	*0.01 nH*	*229.58 fF*

Table 3-2 Lumped model characterization of the square ring FSS with a period of 8mm

Ring edge width	*Ring edge length*	L_{opt}	C_{opt}
0.4 mm	*4.2 mm*	*3.91 nH*	*11.12 fF*
	4.8 mm	*3.57 nH*	*16.78 fF*
	5.4 mm	*3.56 nH*	*23.26 fF*
	6.0 mm	*4.00 nH*	*27.94 fF*
	6.6 mm	*4.67 nH*	*31.36 fF*
	7.2 mm	*7.25 nH*	*23.86 fF*
	7.8 mm	*4.31 nH*	*68.43 fF*
0.8 mm	*4.2 mm*	*2.69 nH*	*11.27 fF*
	4.8 mm	*2.36 nH*	*17.47 fF*
	5.4 mm	*2.31 nH*	*25.18 fF*
	6.0 mm	*2.58 nH*	*32.23 fF*
	6.6 mm	*3.13 nH*	*37.70 fF*
	7.2 mm	*4.11 nH*	*37.73 fF*
	7.8 mm	*5.27 nH*	*36.73 fF*
1.2 mm	*4.2 mm*	*2.06 nH*	*11.13 fF*
	4.8 mm	*1.67 nH*	*11.22 fF*
	5.4 mm	*1.51 nH*	*25.78 fF*
	6.0 mm	*1.61 nH*	*35.70 fF*
	6.6 mm	*2.06 nH*	*42.67 fF*
	7.2 mm	*2.86 nH*	*45.10 fF*
	7.8 mm	*4.59 nH*	*36.82 fF*
1.6 mm	*4.2 mm*	*1.77 nH*	*11.25 fF*
	4.8 mm	*1.29 nH*	*17.22 fF*
	5.4 mm	*1.02 nH*	*25.79 fF*
	6.0 mm	*0.95 nH*	*37.60 fF*
	6.6 mm	*1.13 nH*	*50.06 fF*
	7.2 mm	*1.66 nH*	*57.85 fF*
	7.8 mm	*3.34 nH*	*44.72 fF*
2.0 mm	*4.2 mm*	*1.72 nH*	*11.24 fF*
	4.8 mm	*1.10 nH*	*18.24 fF*
	5.4 mm	*0.79 nH*	*25.73 fF*
	6.0 mm	*0.61 nH*	*37.85 fF*
	6.6 mm	*0.59 nH*	*54.07 fF*
	7.2 mm	*0.79 nH*	*72.20 fF*
	7.8 mm	*1.46 nH*	*81.42 fF*

Table 3-3 Lumped model characterization of the crossed dipole FSS with a period of 8mm

Dipole edge width	Dipole edge length	L_{opt}	C_{opt}
0.4 mm	4.2 mm	9.13 nH	2.83 fF
	4.8 mm	7.98 nH	4.55 fF
	5.4 mm	7.37 nH	6.16 fF
	6.0 mm	6.70 nH	8.92 fF
	6.6 mm	6.35 nH	11.52 fF
	7.2 mm	6.11 nH	14.34 fF
	7.8 mm	5.84 nH	19.03 fF
0.8 mm	4.2 mm	6.39 nH	3.92 fF
	4.8 mm	5.65 nH	6.34 fF
	5.4 mm	5.40 nH	8.38 fF
	6.0 mm	5.36 nH	10.25 fF
	6.6 mm	5.12 nH	13.17 fF
	7.2 mm	5.00 nH	17.10 fF
	7.8 mm	5.03 nH	22.13 fF
1.2 mm	4.2 mm	4.70 nH	4.97 fF
	4.8 mm	4.47 nH	6.83 fF
	5.4 mm	4.20 nH	9.66 fF
	6.0 mm	4.18 nH	12.11 fF
	6.6 mm	4.21 nH	15.59 fF
	7.2 mm	4.36 nH	18.74 fF
	7.8 mm	4.49 nH	24.95 fF
1.6 mm	4.2 mm	3.58 nH	5.97 fF
	4.8 mm	3.35 nH	8.35 fF
	5.4 mm	3.27 nH	10.93 fF
	6.0 mm	4.27 nH	14.53 fF
	6.6 mm	3.46 nH	17.84 fF
	7.2 mm	3.76 nH	21.44 fF
	7.8 mm	4.18 nH	27.09 fF
2.0 mm	4.2 mm	2.83 nH	7.00 fF
	4.8 mm	2.51 nH	10.06 fF
	5.4 mm	2.44 nH	13.14 fF
	6.0 mm	2.52 nH	16.42 fF
	6.6 mm	2.76 nH	20.15 fF
	7.2 mm	3.24 nH	23.79 fF
	7.8 mm	4.11 nH	27.58 fF

The consistency of the series LC equivalents for the lumped models of these surfaces is illustrated in Figure 3-4 to Figure 3-6. In corresponding figures, the shunt model impedance values obtained via simulation and lumped models are compared for the three FSS types. As can be seen from the figures, series LC representation of the corresponding FSS types is convenient to use for the design process.

As an input to the next step of the design method, the upper and lower bounds for the LC parameters of candidate surfaces are:

Table 3-4 Lower and upper bounds for the LC parameters of candidate surfaces

	Square patch	Crossed dipole	Square ring
L_{min}	0.01 nH	2.51 nH	0.59 nH
L_{max}	2.89 nH	9.13 nH	7.25 nH
C_{min}	6.79 fF	2.83 fF	11.12 fF
C_{max}	299.58 fF	27.58 fF	81.42 fF

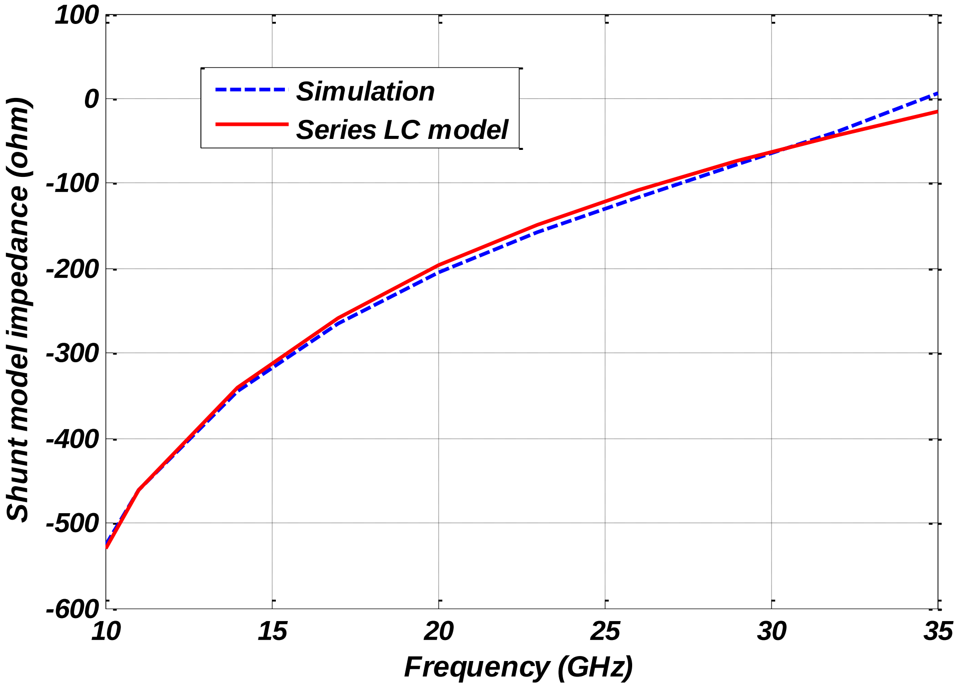

Figure 3-4 Shunt model impedance for the patch type FSS with edge length of 5.4 mm

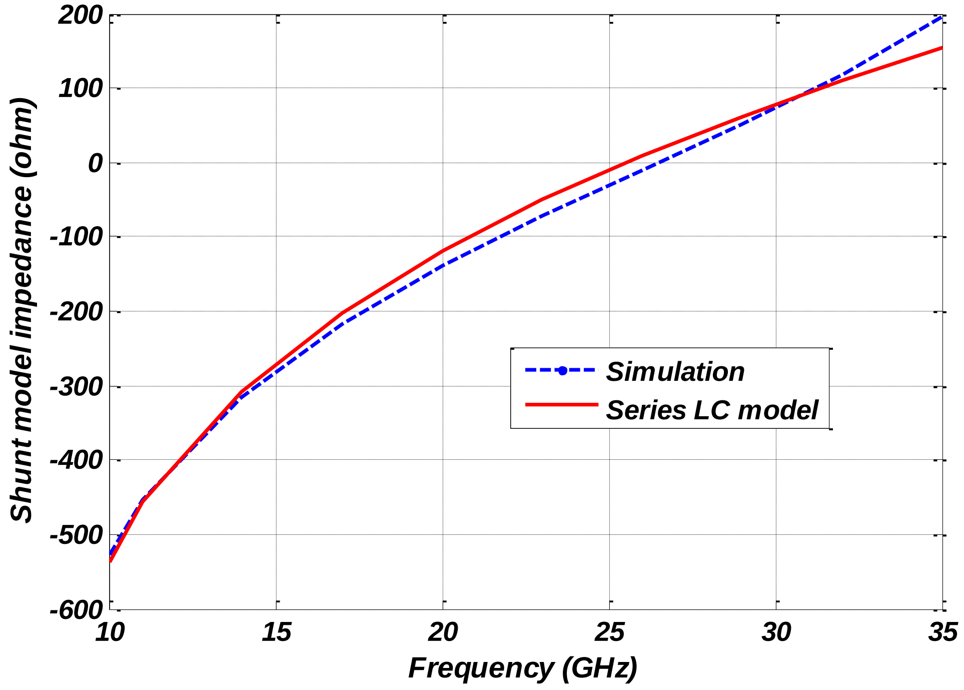

Figure 3-5 Shunt model impedance for the square ring type FSS with edge length of 5.4 mm and edge width of 1.2 mm

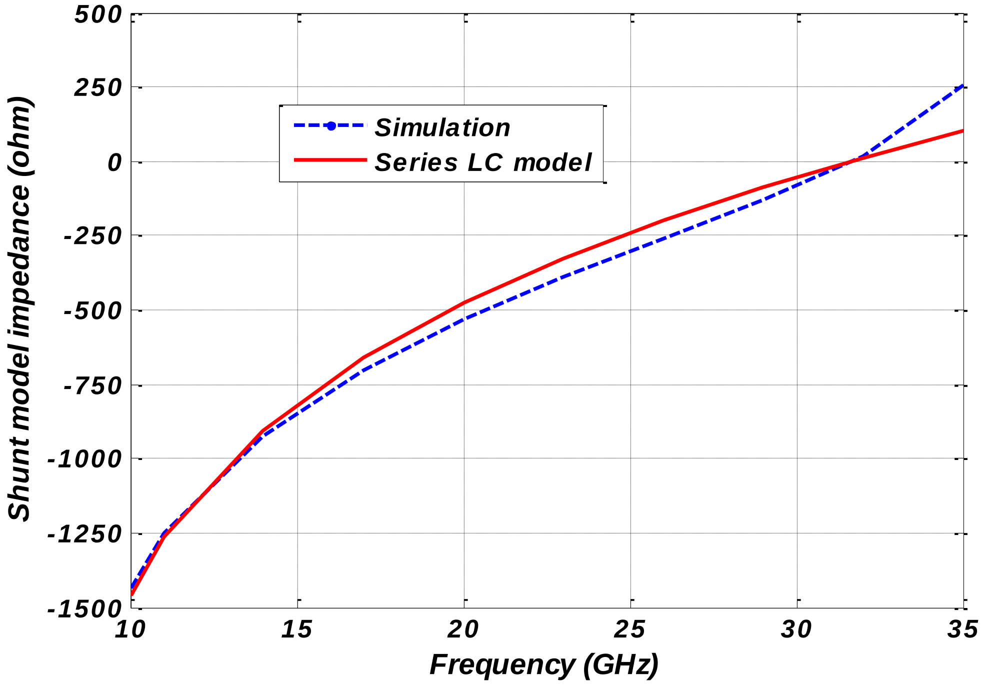

Figure 3-6 Shunt model impedance for the crossed dipole type FSS with edge length of 5.4 mm and edge width of 0.8 mm

3.3 Optimization by using equivalent circuit techniques and Genetic Algorithm

In this step of the method, by using the extracted LC limits in the second step and according to the design constraints specified in the first step, the suitable FSS types and proper lumped resistance values are determined for each layer of the absorber. The corresponding decisions are realized by using Genetic Algorithm, which is a widely known optimization technique used for various applications. By using the Genetic Algorithm optimization technique, the thickness values of the separating slabs; optimum inductance, capacitance and resistance values for each layer of the structure are searched within the specified limits. During this optimization process, every layer is modelled as lumped impedance which is connected as shunt to the transmission lines representing the layer separator slabs. By using transmission line theory, the input impedance of the structure is tried to be matched to free space intrinsic impedance, which is approximately 377 ohms.

The inputs of the optimization are the frequency range of interest, the number of layers, upper and lower bounds for the thickness values of separating slabs (which can be discrete values for practical applications), the electrical characteristics (permeability, permittivity, loss tangent) of the separating slabs, lower and upper limits for the LC parameters of each candidate FSS type and also the limits of the lumped resistance values to be used for absorption mechanism.

In Genetic Algorithm, the variables related to the structure to be designed are represented as binary numbers, consisting of bits which can be ‘1’ or ‘0’. The term *‘individual’* represents a set of all the variables to be optimized. To state more clearly, an individual is a string of binary numbers consisting of 1s and 0s, which corresponds to a case that all the variables of the design are set to specific values. The *‘fitness’* of an individual is a number regarding how close the characteristics of the structure represented by that individual are to the desired ones. The optimization is realized by using a set of individuals, which is called as *‘population’*.

To state the process shortly, optimization starts with an initialization of the population by creating a number (*'population density'*) of individuals composed of random strings. Then the fitness values of all the individuals are calculated during the corresponding iteration. The individuals are ordered from healthiest to the weakest. By using the current individuals in the population, which are now called as *'parents',* new individuals are generated. The newly generated individuals are called as *'children'*. The reproduction of the parents to give birth to children is realized by crossover between the strings of the parents as illustrated in Figure 3-7, below:

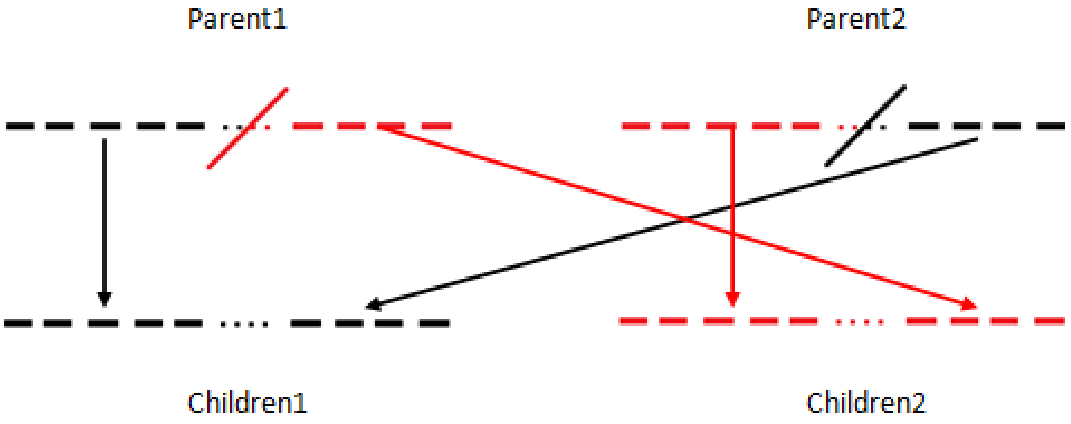

Figure 3-7 Crossovers (reproduction of parents) in Genetic Algorithm

The parents that will take part in the reproduction are chosen with respect to their fitness values. The healthier ones are more probable to be selected for children generation.

The weak parents in terms of fitness are replaced by the newly generated children. The number of healthiest parents that will stay for the next iteration in the current population is defined by a term called as *'elite selection'*. In any iteration, children with a number of $population\ density * (1 - elite\ selection)$ are generated.

To increase the variety, which is the basis of Genetic Algorithm, a process called as *'mutation'* is realized. In every iteration, with a probability of *'mutation probability',* random individuals with a number of *'mutant individual number'* are selected.

Randomly selected bits with a number of *'mutant bit number'* of the chosen individuals are complemented such that if the corresponding bit is a 1, then it is replaced with a 0 and vice versa.

These processes are repeated until the desired characteristics or the maximum iteration number is reached. Detailed information regarding the Genetic Algorithm can be obtained in [33]. The main steps of the method are summarized in Figure 3-8.

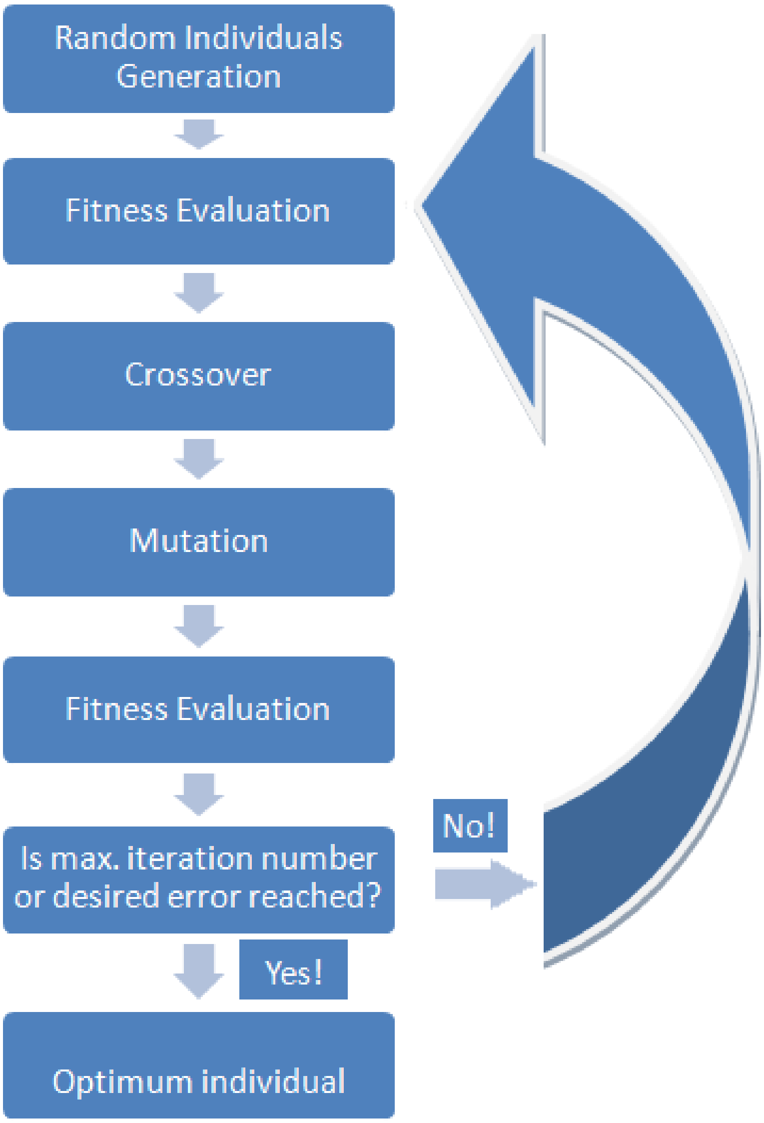

Figure 3-8 Optimization steps of the Genetic Algorithm

For the two-layered absorber designed with the proposed method, inputs for the code are:

$f_{start}: 10\ GHz$ $f_{stop}: 35\ GHz$
$desired\_absorption: 15\ dB$
$min.slab\ thickness: 0.4\ mm$
$max.slab\ thickness: 2.4\ mm$
$min.lumped\ resistance\ values: 50\ \Omega$
$max.lumped\ resistance\ values: 1500\ \Omega$

$$\left.\begin{array}{ll} C^1_{min}: 6.79\ fF & L^1_{min}: 0.01\ nH \\ C^1_{max}: 299.58\ fF & L^1_{max}: 2.89\ nH \end{array}\right\} \text{square patch}$$

$$\left.\begin{array}{ll} C^2_{min}: 11.12\ fF & L^2_{min}: 0.59\ nH \\ C^2_{max}: 81.42\ fF & L^2_{max}: 7.25\ nH \end{array}\right\} \text{square ring}$$

$$\left.\begin{array}{ll} C^3_{min}: 2.83\ fF & L^3_{min}: 2.51\ nH \\ C^3_{max}: 27.58\ fF & L^3_{max}: 9.13\ nH \end{array}\right\} \text{crossed dipole}$$

$slab\ permittivity\ (relative): 1$
$slab\ permeability\ (relative): 1$
$slab\ loss\ tangent: 0$
$max.iteration\ number: 600$
$elite\_selection: 10\%$
$p\_mutation: 15\%$
$population\ density: 800$
$R\ bit\ number: 10$ $L\ bit\ number: 8$ $C\ bit\ number: 8$
$thickness\ bit\ number: 10$
$number\ of\ layers: 2$
$number\ of\ FSS\ types: 3$

The inputs regarding the bit numbers (R bit number, L bit number, C bit number, thickness bit number), shows the bit number of the string which the corresponding variable is represented. According to the corresponding bit numbers, an individual is a binary word consisting of 62 bits.

Bit Number	*2*	*2*	*10*	*8*	*8*	*10*	*8*	*8*	*4*	*4*
Synonym	*FSS type (bottom)*	*FSS type (top)*	R^1	L^1	C^1	R^2	L^2	C^2	t^1	t^2

where, the synonyms with an upper index of 1 correspond to parameters regarding the bottom FSS layer, while ones with an index of 2 correspond to the parameters of the upper FSS layer. The synonyms represented by t, represent the thickness values of the upper and lower separating slabs.

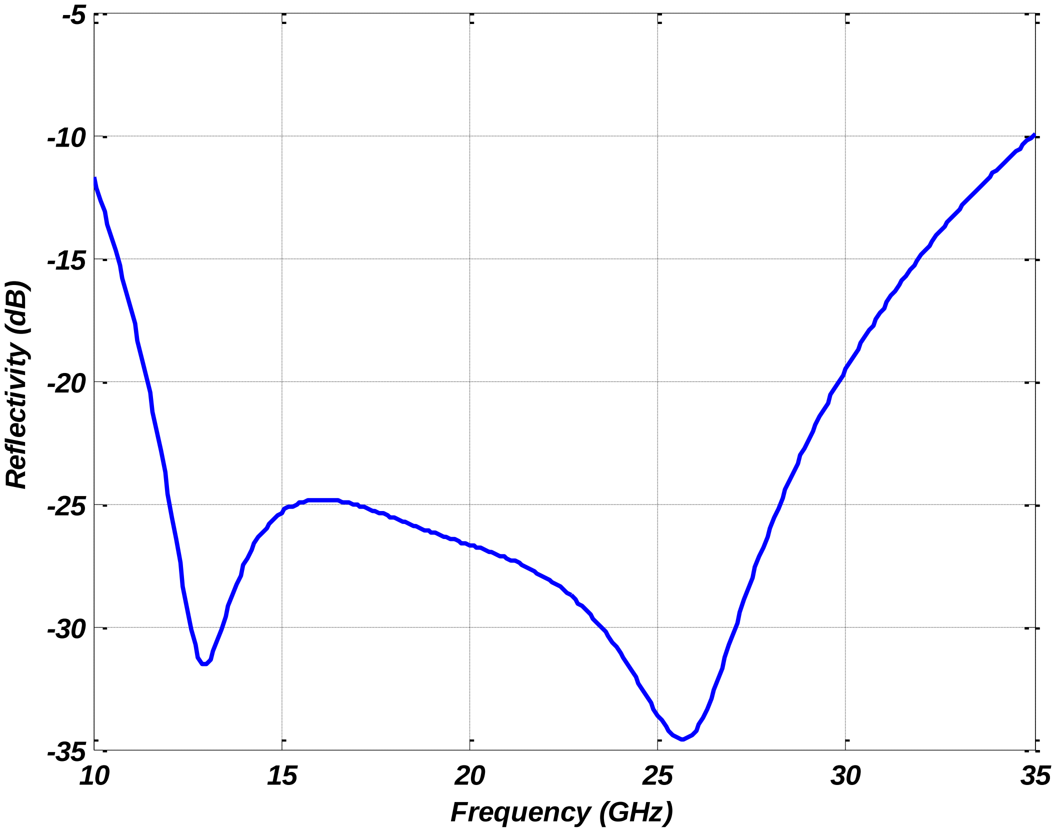

Figure 3-9 Reflectivity characteristics for the optimum design obtained by Genetic Algorithm

According to the code outputs, optimum variables resulting in a reflectivity characteristic given by Figure 3-9 are given in Table 3-5.

Table 3-5 Optimum design parameters for the 2-layered absorber example

	L_{opt}	C_{opt}	R_{opt}
Upper FSS	*3.26 nH*	*14.45 fF*	*542.2 Ω*
Upper Slab		*2.2 mm*	
Bottom FSS	*2.01 nH*	*44.3 fF*	*231.2 Ω*
Bottom Slab		*2.4 mm*	
Metal Plate			

According to optimum values of the code output regarding the inductance and capacitance values of the frequency selective surfaces, it is convenient to use square ring type FSS for the bottom layer and crossed dipole type FSS for the upper layer.

3.4 Determination of the dimensional parameters together with proper surface resistance values for each FSS layer

In this step of the proposed method, optimum reactance values of the Genetic Algorithm outputs are tried to be realized by altering the corresponding FSS dimensions and optimum surface resistance values are searched to achieve desired lumped resistance values. This optimization process is conducted by using a full wave electromagnetic solver (i.e. HFSS) in a smart iterative method. The determination of FSS dimensions together with proper surface resistance values will be explained over the 2-layered example absorber whose optimum lumped parameters are obtained in the previous step.

For the bottom FSS of the 2-layered RAM, it has been decided to use square ring type FSS. The optimum inductance and capacitance values for the corresponding layer have been determined as 2.01 nH and 44.3 fF, respectively. If we look at Table 3-2 extracted in the second step, which shows lumped capacitance and inductance values for changing ring dimensions, it seems that a square ring layer with edge length of 6.6 mm and edge width of 1.2 mm can be used. To realize the optimum lumped resistance, 231.2 ohm, a proper surface resistance value should be determined. To find this resistance value, a starting point can be the equation 2.20, given in Chapter 2, as:

$$R \approx R_s \frac{S}{A} \tag{2.20}$$

For the square ring, effective surface area is not clear, but can be taken as the total area of the 2 arms, since the excitation with a linear polarization which is directed along any 2 arms is effective on the corresponding arms, as illustrated in Figure 3-10.

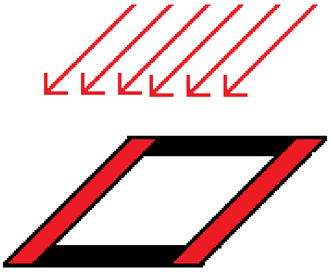

Figure 3-10 Illustration of the effective area of a square ring illuminated with a linearly polarized wave

Hence the effective area for the square ring can be taken as:

$$2 * 1.2\ \mathrm{mm} * 6.6\ \mathrm{mm} = 15.84\ \mathrm{mm}^2$$

And as a starting point, the surface resistance value of the ring can be taken as:

$$R_s^{ring} \approx 231.2\,\frac{15.84}{64} = 57.2\ \Omega/sq$$

With the corresponding dimensions and the surface resistance value, the square ring type FSS is simulated in HFSS. In HFSS, surface resistance can be assigned to sheets by using the impedance boundary condition, shown by a screenshot taken from HFSS in Figure 3-11.

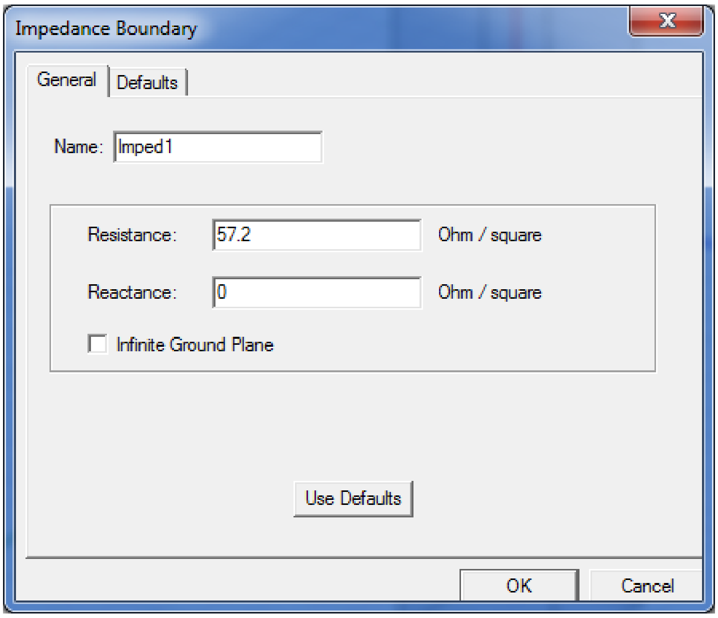

Name: Imped1

Resistance: 57.2 Ohm / square

Reactance: 0 Ohm / square

☐ Infinite Ground Plane

Figure 3-11 Impedance boundary condition dialog box of HFSS used for surface resistance assignment

The shunt model impedance values of the square ring with specified dimensions and surface resistance are given in Figure 3-12 and Figure 3-13.

The lumped model values of the simulated ring type FSS, came out to be as 1.207 nH and 51.89 fF, for the inductance and capacitance values, respectively. Corresponding values obtained in the second step by lossless FSS simulations were 2.06 nH and 42.67 fF, respectively. This result shows that the reactive part of the lossy FSS impedance is not independent from the sheet conductance. And hence, realization of the optimum impedance should be conducted by altering the FSS dimensions and surface resistance in an interactive manner.

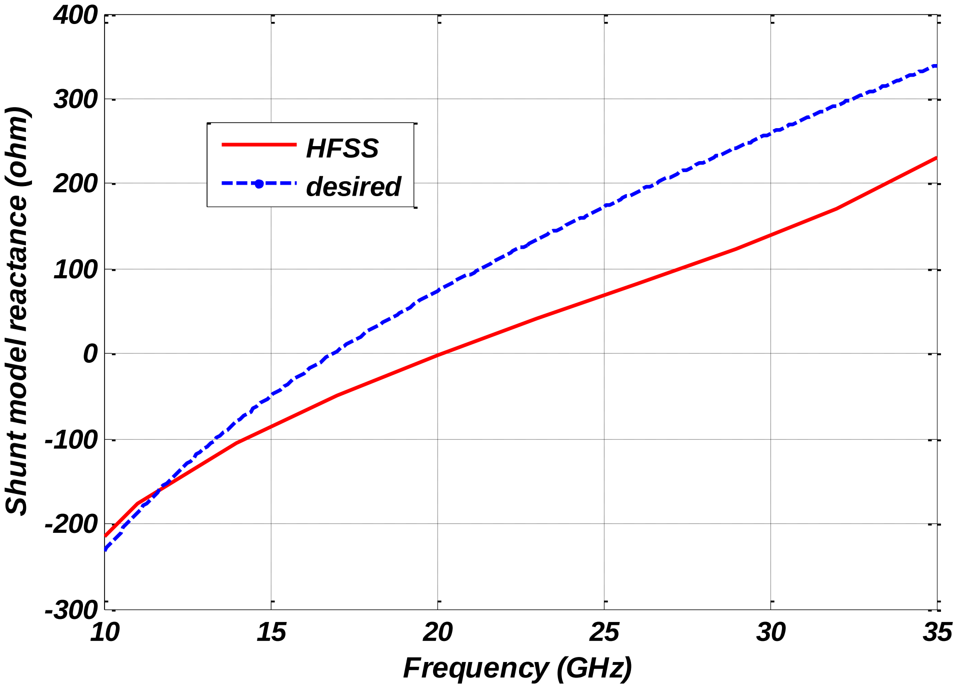

Figure 3-12 Shunt model reactance of the square ring with edge width of 1.2 mm, edge length of 6.6 mm and surface resistance of 57.2 Ω/sq

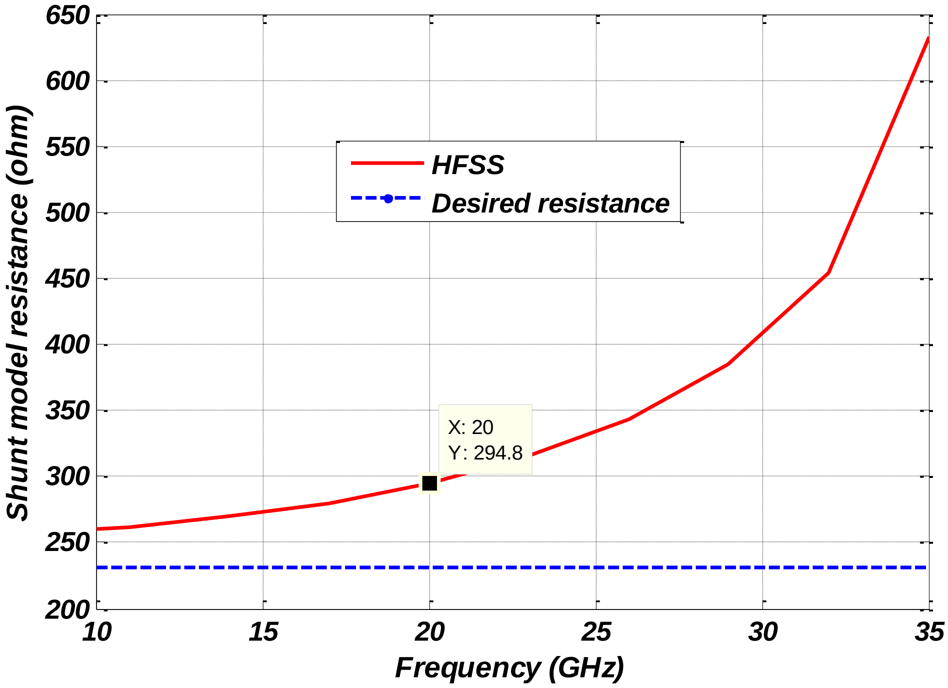

Figure 3-13 Shunt model resistance of the square ring with edge width of 1.2 mm, edge length of 6.6 mm and surface resistance of 57.2 Ω/sq

The obtained capacitance value is higher than the desired one; hence the edge length of the ring should be decreased. On the other hand, the realized inductance is smaller than the desired one; so the width of the edges should also be decreased.

For the case of real part of the shunt model impedance, as can be seen from Figure 3-12, the shunt model resistance does not poses a stationary characteristics with respect to frequency. This behaviour can be explained by the change of the effective area as the frequency is changed. The corresponding change in the effective area can be demonstrated by giving the plots of current densities on the ring surface for two distinct frequency values, Figure 3-14.

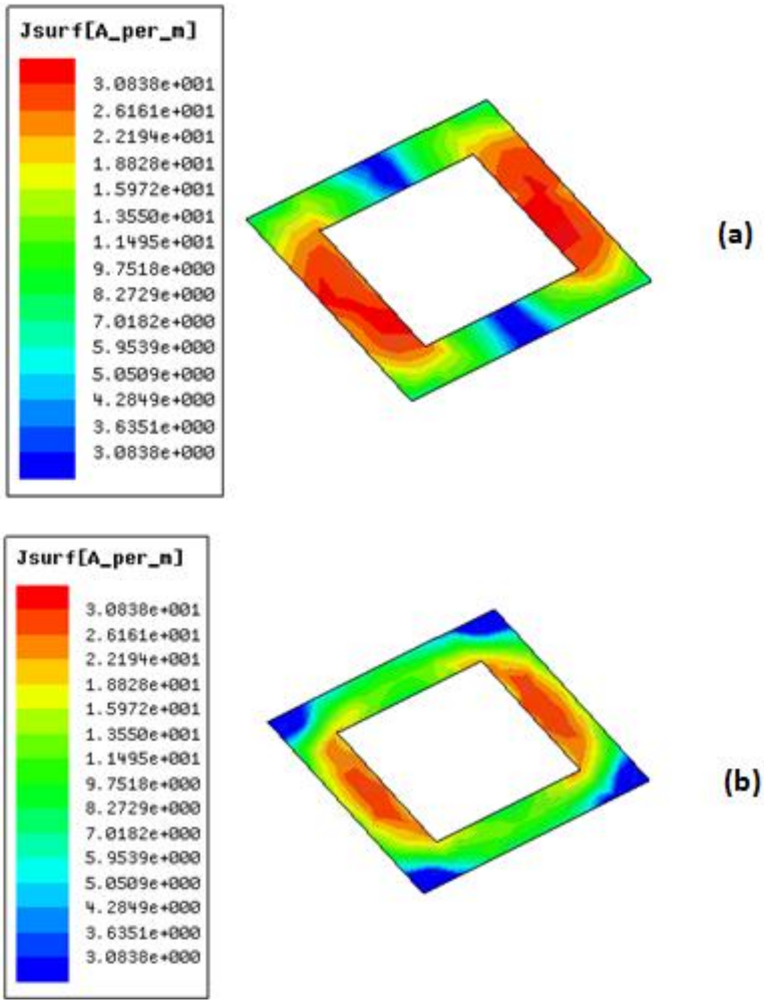

Figure 3-14 Magnitude of surface current densities on the square ring taken from HFSS: (a) 15 GHz, (b) 35 GHz (fields are plotted within a range of 20 dB)

As can be seen from Figure 3-14, as the frequency increases, the effective area on the ring surface decreases, and hence the shunt model resistance increases. So, it is not possible to obtain an unchanging resistance value for the whole operation frequency range. Therefore, the desired resistance value is tried to be achieved at 20 GHz, which is almost the center of the operation range where the expected absorption level is high.

In light of this information, a few simulations are conducted iteratively to achieve the desired layer characteristics. The final characteristics regarding the shunt model impedance of the optimized ring type FSS together with the desired characteristics are shown in Figure 3-15 and Figure 3-16. The edge with of the optimized structure is 0.88 mm, the edge length is 6.45 mm, and the optimum surface resistance is 30 ohm/sq. Also, lumped equivalent inductance, capacitance and resistance values are compared with the desired ones in Table 3-6.

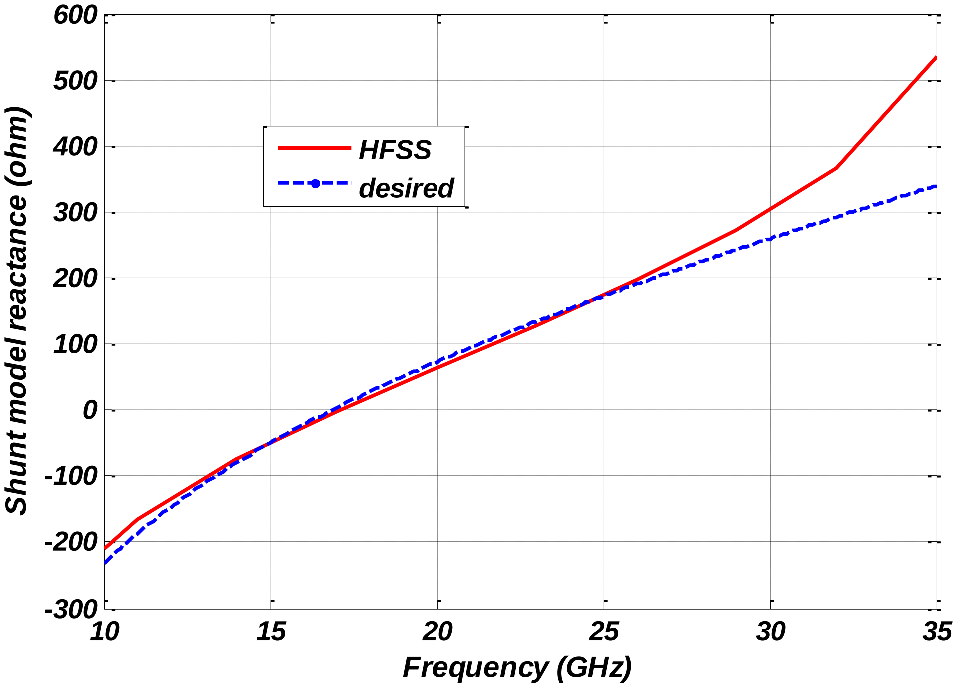

Figure 3-15 Shunt model reactance of the square ring with edge width of 0.88 mm, edge length of 6.45 mm and surface resistance of 30 Ω/sq

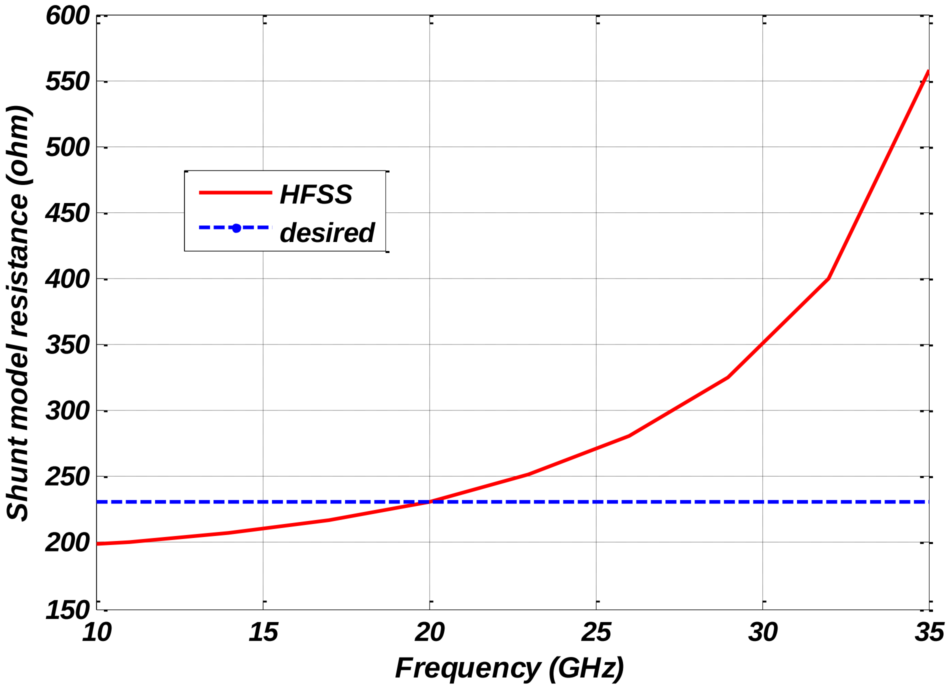

Figure 3-16 Shunt model resistance of the square ring with edge width of 0.88 mm, edge length of 6.45 mm and surface resistance of 30 Ω/sq

Table 3-6 Lumped model parameters of the realized ring type FSS

	Desired	Realized
L	***2.01 nH***	***1.97 nH***
C	***44.3 fF***	***44.25 fF***
R	***231.2 Ω***	***232.6 Ω (@ 20 GHz)***

The situation is similar for the case of crossed dipole type FSS, which will be used for the top layer in the final design. As can be seen from Table 3-3, to realize an inductance of 3.26 nH and a capacitance of 14.45 fF, it seems reasonable to start with a dipole layer with edge length of 5.7 mm and edge width of 1.6 mm. An initial value for the surface resistance to be used can be estimated by the method used for the case of ring optimization.

Effective area for crossed dipole can be taken as the area of one of two arms owing to linearly polarized illumination. Hence, the surface resistance value can be calculated as:

$$R_s^{crossed\ dipole} \approx 542.2\ \frac{1.6 * 5.7}{64} = 77.26\ \Omega/sq$$

With the corresponding dimensions and the surface resistance value, the crossed dipole type FSS is simulated in HFSS. The shunt model impedance values of the crossed dipole with specified dimensions and surface resistance are given in Figure 3-17 and Figure 3-18.

The lumped model values of the simulated crossed dipole type FSS, came out to be as 2.89nH and 12.42 fF, for the inductance and capacitance values, respectively. Corresponding desired values obtained in the second step by lossless FSS simulations were 3.26 nH and 14.45 fF, respectively. Hence, both inductance and capacitance values for the lumped model of the simulated case should be increased. This can be achieved by simultaneously increasing the edge length and decreasing the edge with of the dipole arms.

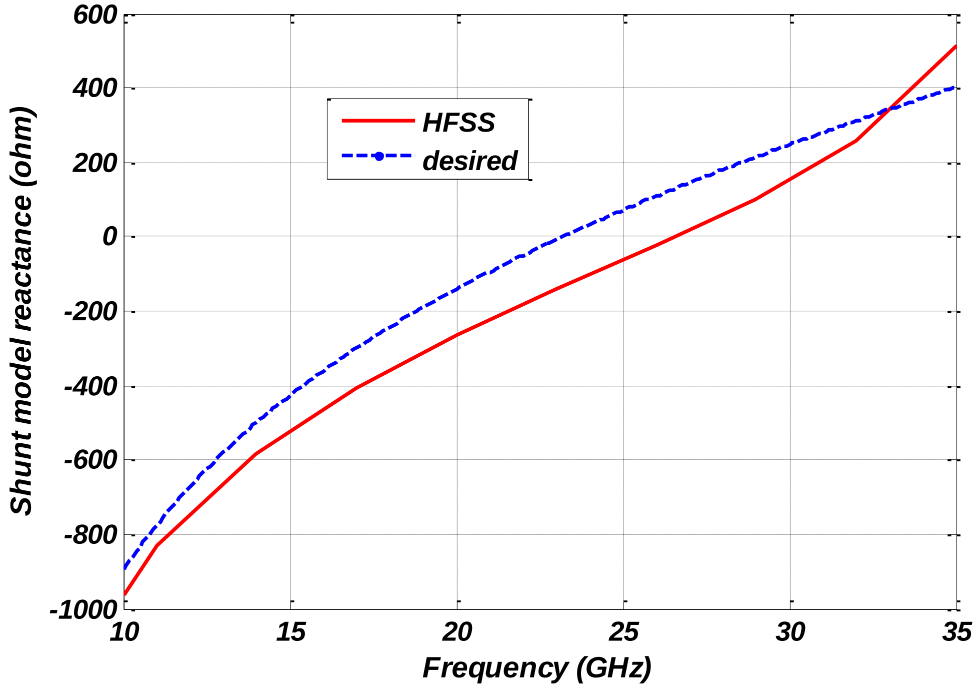

Figure 3-17 Shunt model reactance of the crossed dipole with edge width of 1.6 mm, edge length of 5.7 mm and surface resistance of 77.26 Ω/sq

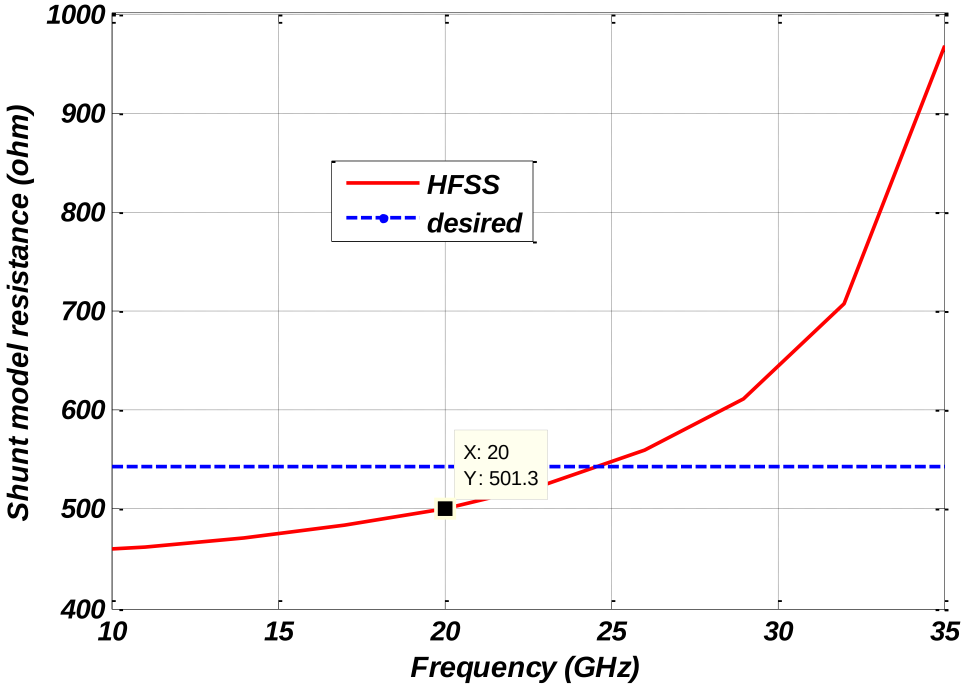

Figure 3-18 Shunt model resistance of the crossed dipole with edge width of 1.6 mm, edge length of 5.7 mm and surface resistance of 77.26 Ω/sq

After a few successive iterations carried out in HFSS, optimum characteristics are obtained with a dipole layer whose edge width is 1.25 mm, edge length is 6.5 mm and surface resistance is 67 ohm/sq. The shunt model impedance of this optimized layer is shown in Figure 3-19 and Figure 3-20.

The desired and the realized values regarding lumped model equivalent parameters of the crossed dipole are compared in Table 3-7. As can be seen from the table, the optimized structure almost satisfies the desired characteristics.

Table 3-7 Lumped equivalent model parameters of the realized crossed dipole type FSS

	Desired	**Realized**
L	***3.26 nH***	***3.31 nH***
C	***14.45 fF***	***14.35 fF***
R	***542.2 Ω***	***543.6 Ω (@ 20 GHz)***

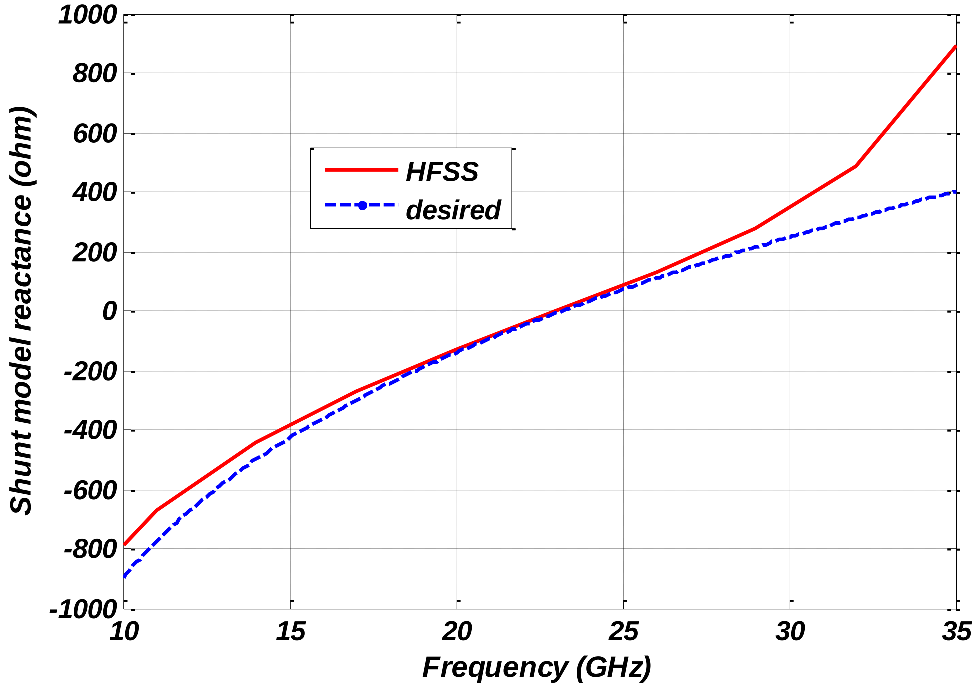

Figure 3-19 Shunt model reactance of the crossed dipole with edge width of 1.25 mm, edge length of 6.5 mm and surface resistance of 67 Ω/sq

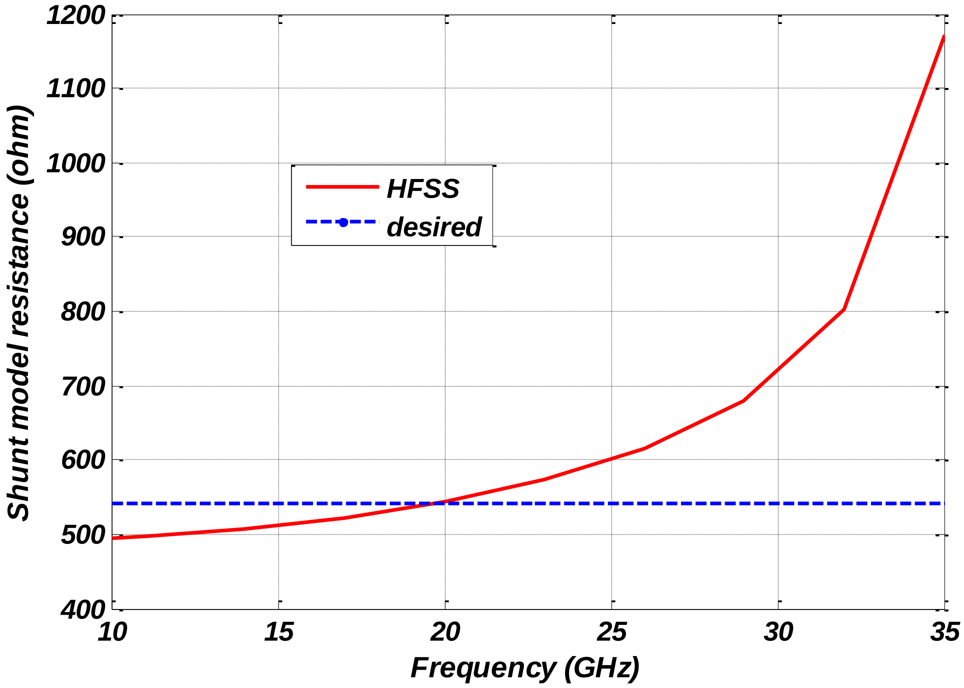

Figure 3-20 Shunt model resistance of the crossed dipole with edge width of 1.25 mm, edge length of 6.5 mm and surface resistance of 67 Ω/sq

The monotonic increase characteristic of the shunt model resistance is observed for the crossed dipole type FSS, as in the case of square ring. At 15 GHz and 35 GHz, the surface currents induced on the crossed dipole FSS are shown in Figure 3-21 within a current magnitude range of 40 dB. As can be seen, the effective area is very small for upper frequency point, which causes an increase in the shunt model resistance according to equation 2.20.

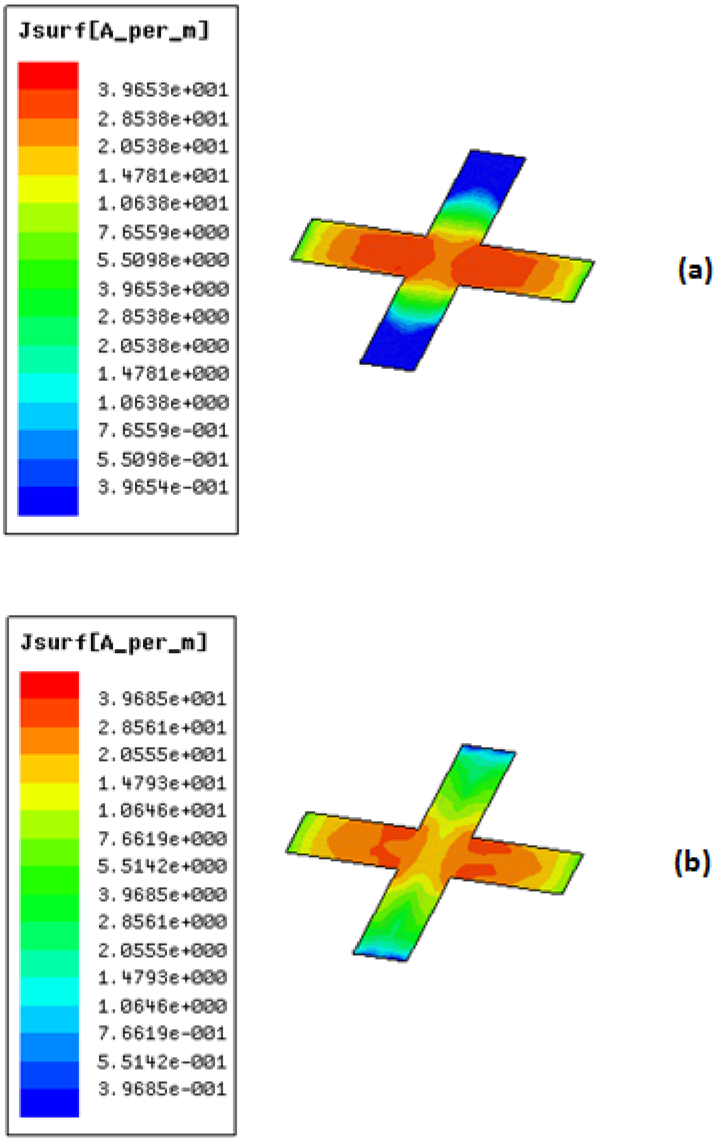

Figure 3-21 Magnitude of surface current densities on the crossed dipole taken from HFSS: (a) 15 GHz, (b) 35 GHz (fields are plotted within a range of 40 dB)

3.5 Verification of the absorber with a full wave simulation

In this final step of the proposed method, by using the lossy FSS layers optimized in the previous step, the absorbing structure is simulated via a full wave simulation tool. The overall performance of the absorber is verified and if needed a further optimization over the whole structure is performed. This time, optimization is carried out to compensate the unexpected characteristics owing to the coupling between the layers. The corresponding coupling phenomenon cannot be embedded into the genetic algorithm optimization step since analytical formulations regarding the mutual impedance between the consecutive layers do not exist in the literature. Hence, the design pursues assuming that the corresponding coupling mechanism will not affect the final performance of the absorber significantly, in other words the FSS layers will almost pose their free standing characteristics also when combined together.

For the case of two-layered example absorber, the optimized layers are combined to model the whole structure in HFSS as shown in Figure 3-22.

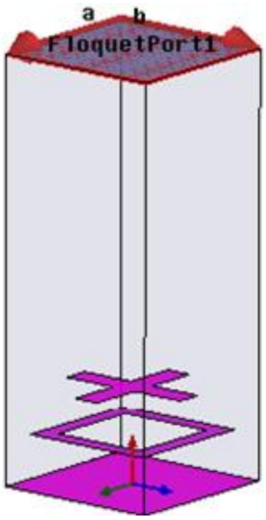

Figure 3-22 The HFSS model of the final absorbing structure

The input impedance and the reflectivity characteristics of the absorbing structure are shown in Figure 3-23 and Figure 3-24, respectively.

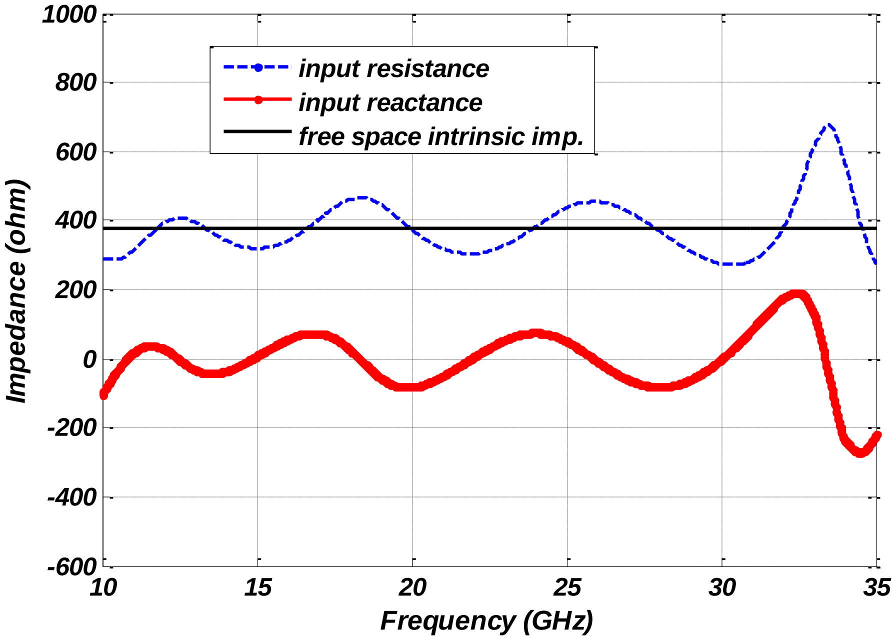

Figure 3-23 Input impedance of the designed two-layered circuit analog RAM

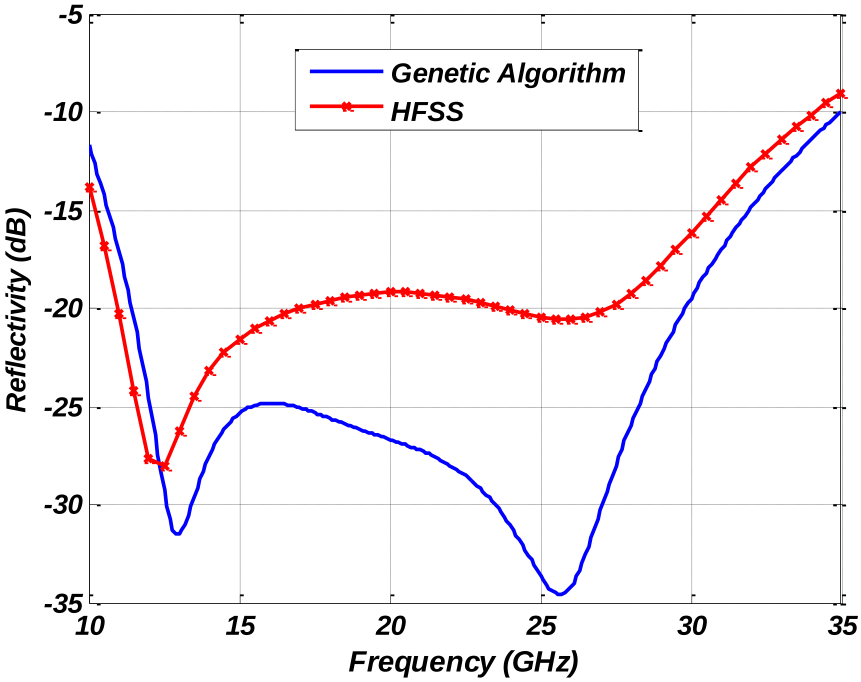

Figure 3-24 Reflectivity characteristics of the designed two-layered RAM

As can be seen from Figure 3-24, there are some discrepancies between expected and the realized characteristics. The corresponding incompatibility can be dedicated to two main reasons. The first one is that the shunt model impedance characteristics of the ring and dipole FSS layers are different from the optimum layer characteristics obtained in GA optimization, especially in terms of layer resistance for upper edge of the band, Figure 3-16 and Figure 3-20. The other reason is the unconsidered mutual coupling between the layers which is mentioned at the beginning of the final step explanation. To clarify which reason outweighs the other, a synthetic reflectivity characteristic is constructed in MATLAB by using the realized layers' impedance values, shown in Figure 3-15, Figure 3-16, Figure 3-19 and Figure 3-20, and transmission line theory. By this way, the FSS layers optimized in the fourth step are modelled exactly to see the effects of discrepancy due to deviation from the desired layer characteristics, since the mutual coupling is still not taken into consideration. The synthesized reflectivity is compared with the realized and desired ones in Figure 3-25.

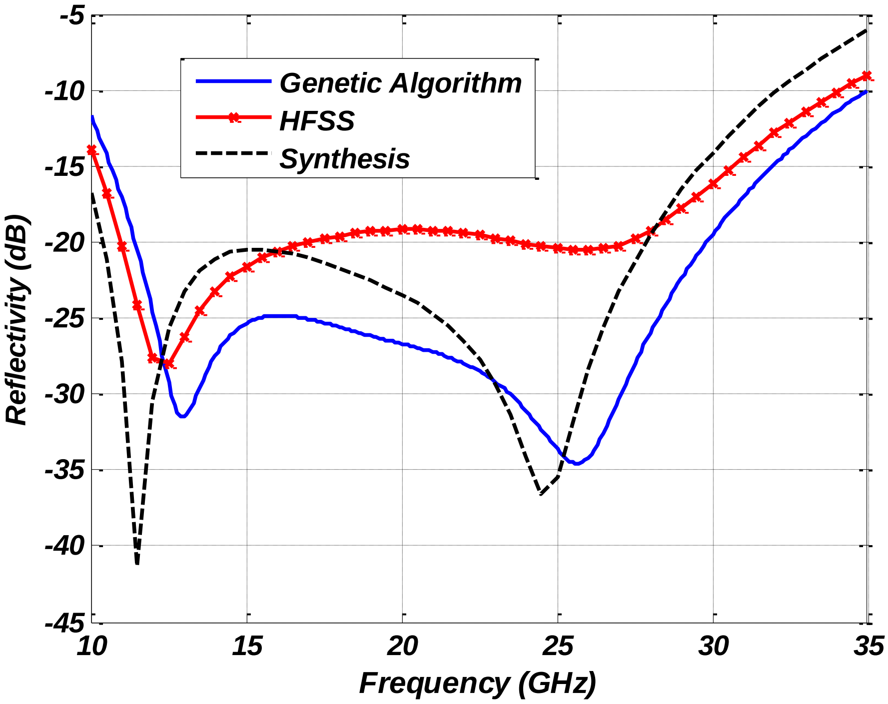

Figure 3-25 Synthesized, ideal and realized reflectivity characteristics for the two-layered RAM

As can be seen from the Figure 3-25, it is not clear which factor outweighs for the deviation from the desired characteristics, but it can be said that the mutual coupling between the layers is effective for the whole band by comparing the synthesized and realized reflectivity values.

Although out of concern for the scope of the design method, to see the behaviour of the absorber under oblique incidence cases, the unit cell model is simulated for angles of incidence up to 40 degrees with 10 degree steps in one of the principal planes. The reflectivity characteristics of the RAM are shown in Figure 3-26 and Figure 3-27 for perpendicular and parallel polarization cases, respectively.

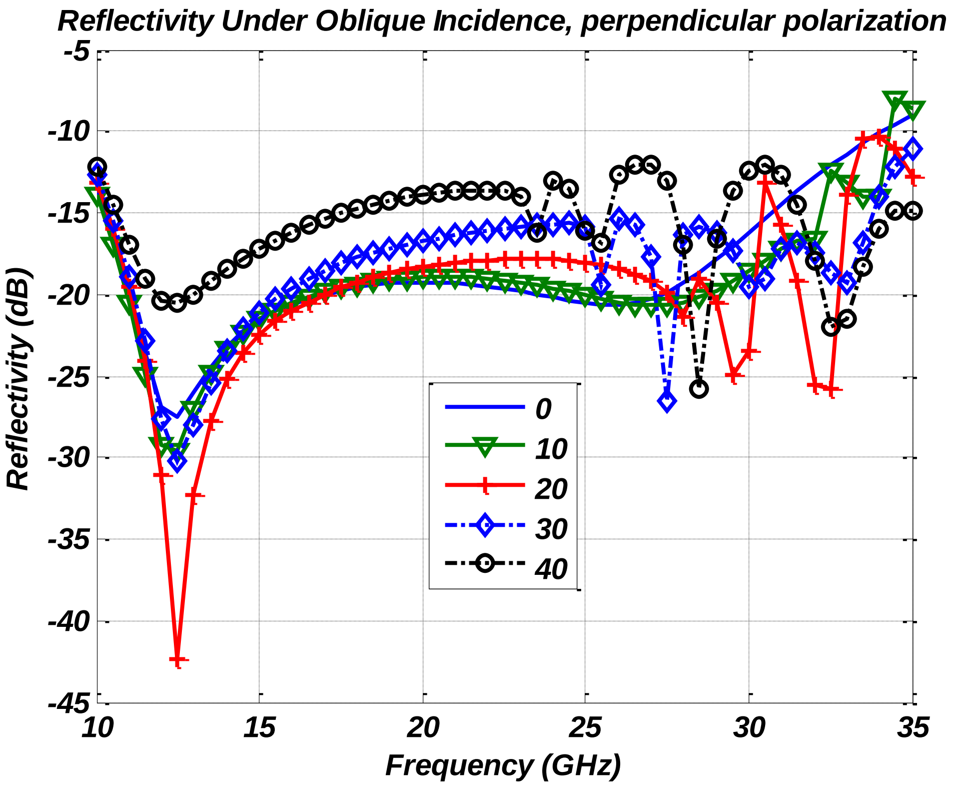

Figure 3-26 Reflectivity characteristics of the designed RAM in Figure 3-22 under oblique incidence case, perpendicular polarization

As can be seen from Figure 3-26 and Figure 3-27, there occurs ripples on the reflectivity characteristics for the upper edge of the frequency band as the angle of incidence increases. This is not a surprising result, since the the period of the structure is not small enough to suppress higher order modes for angles of incidence values up to 40 degrees (2.23). Due to these higher modes, together with absorption, scattering mechanism also plays role in the reflectivity minimization. Scattering characteristics change rapidly with respect to changing frequency, resulting in ripples on the reflectivity. These figures are shown just to illustrate the performance of the RAM under oblique incidence although it is not a design constraint.

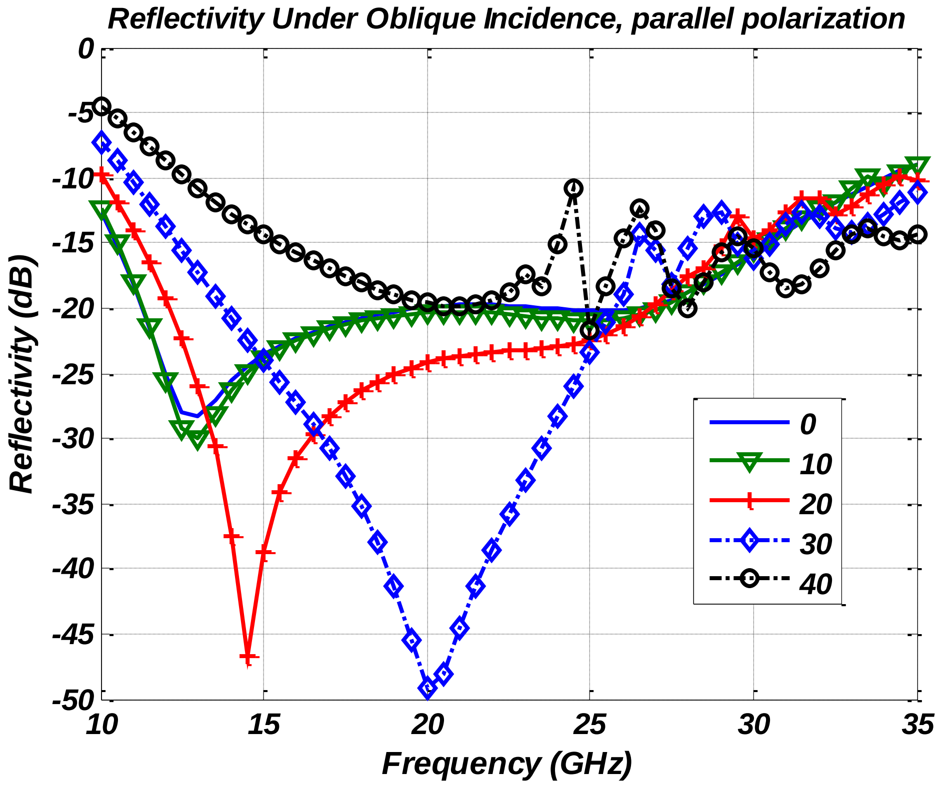

Figure 3-27 Reflectivity characteristics of the designed RAM in Figure 3-22 under oblique incidence, parallel polarization

By using the proposed approach, a second circuit analog RAM is designed. The corresponding structure is a four-layered one consisting of square rings only, a decision obtained by genetic algorithm optimization step. The characteristics of the layers in terms of dimensions and surface resistance values together with the air slab thicknesses are shown in Table 3-8.

Table 3-8 Structural parameters of the four-layered circuit analog RAM designed by the proposed method

	ring length	***ring width***	***surface impedance***
ring4	***3.205 mm***	***0.99 mm***	***151.3 ohm/sq.***
thickness	***2.2 mm (air)***		
ring3	***5.26 mm***	***0.68 mm***	***89.8 ohm/sq.***
thickness	***2.43 mm (air)***		
ring2	***5.56 mm***	***0.25 mm***	***21.02 ohm/sq.***
thickness	***1.78 mm (air)***		
ring1	***5.41 mm***	***0.52 mm***	***62.1 ohm/sq.***
thickness	***2.36 mm (air)***		
Metal Plate			

The HFSS model of the designed structure is shown in Figure 3-28. In Figure 3-29, the reflectivity characteristics of the structure are plotted. The input impedance of the absorber is shown in Figure 3-30.

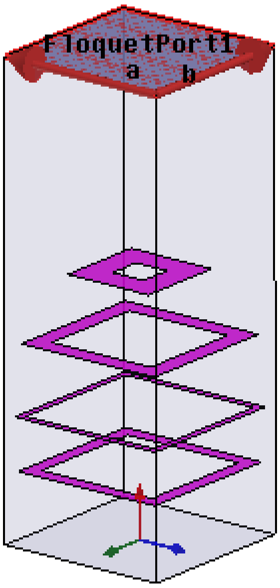

Figure 3-28 HFSS model of the designed four-layered RAM

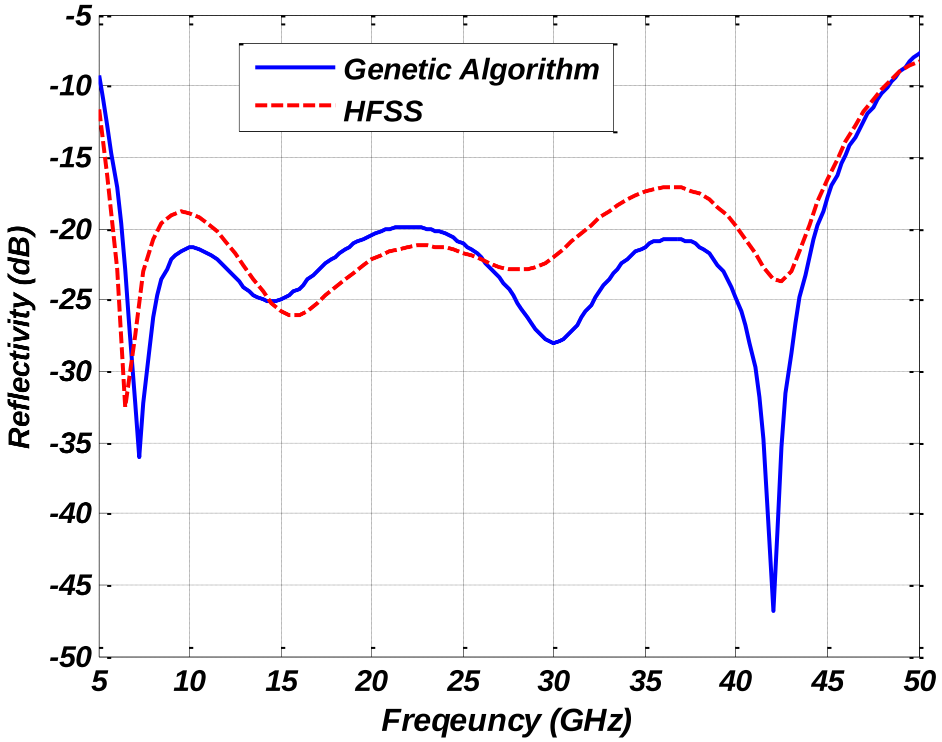

Figure 3-29 Reflectivity characteristics of the designed four-layered RAM

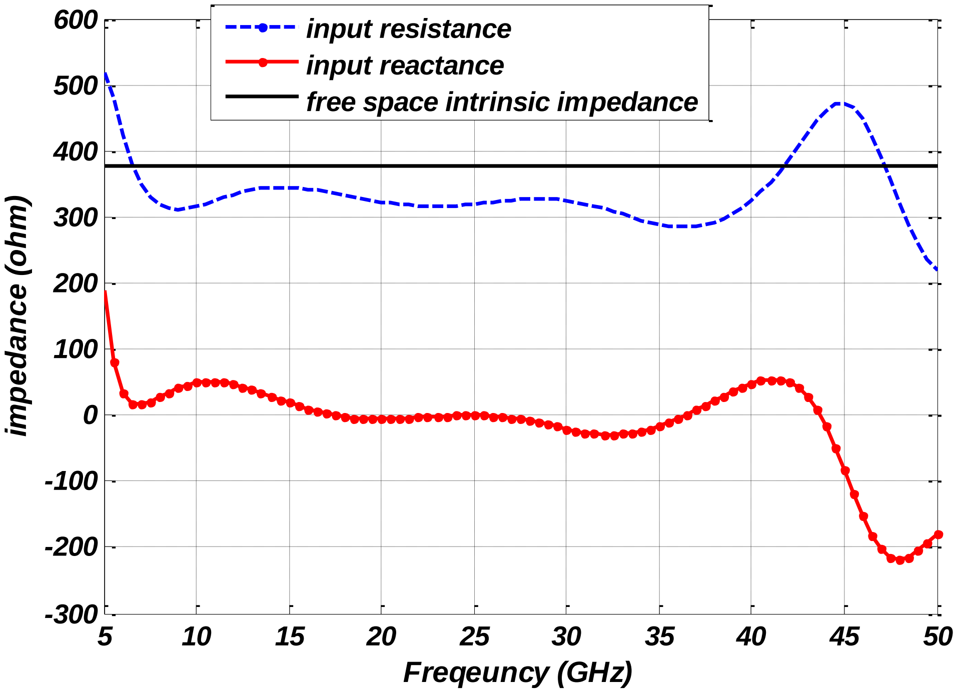

Figure 3-30 Input impedance of the designed four-layered RAM

As can be seen from Figure 3-29, the designed four-layered absorber has a total thickness of $\sim$ 8.77 mm and an operational frequency range of 5.5 GHz up to 45.5 GHz with a reflectivity value less than -15 dB. This result refutes the assertion given in [18], which Alirezah and Anders claim that the optimum FSS type for the design of circuit analog absorbers is the square patch. Their ultra-wideband absorber design consists of three patch type FSS layers with an overall thickness of 15.1 mm, and has a 15 dB absorption band of 3.5 GHz to 25 GHz.

CHAPTER 4

AN EFFICIENT METHOD FOR THE DESIGN OF MULTI-LAYERED CIRCUIT ANALOG RAM BY USING FINITE DIFFERENCE TIME DOMAIN (FDTD)

In Chapter 3, a fast and efficient method for the design of multi-layered circuit analog absorbers is introduced and two example absorbers designed by the proposed approach are presented. As shown in the corresponding chapter, due to interactions between the lossy layers, the resultant reflectivity attributes deviate from the aimed characteristics. Hence, to achieve the desired characteristics, either coupling between the layers should be taken into account during the design process or a further optimization over the whole structure should be carried out. Since, analytical formulations regarding these coupling effects do not exist in the literature; the second method is chosen to carry the current method to one step further. Moreover, with the design method introduced in Chapter 3, MATLAB and a full wave electromagnetic solution tool, HFSS, are needed for the design process. Hence, both to create a compact design tool and to compensate the effects of coupling between the layers of a multi-layered absorber, a numerical code is developed in MATLAB, which uses the finite difference time domain method. The developed code includes the following main capabilities:

- Characterization of single layer lossy and lossless FSS layers via FDTD,
- By using Genetic Algorithm, design of multi-layered absorbers via circuit equivalent models of the characterized FSS layers and transmission line theory,

- To compensate the effects of interactions between the lossy layers, optimization of the designed absorber within limited bounds regarding design parameters by using Genetic Algorithm and FDTD.

4.1 FDTD Fundamentals

The finite difference time domain (FDTD) method has desirable and unique features among the other numerical methods for the analysis of electromagnetic structures. It simply discretizes the Maxwell's equations in time and space domains, and the electromagnetic solution is gathered through a time evolving process. The method is applicable to a wide range of electromagnetic problems including antenna pattern and input impedance characterizations, scattering and RCS calculations and microwave circuit design. The most spectacular property of the scheme is the capability of achieving a broadband solution for the problem with a single simulation. This property makes the method favorable especially for solutions of wideband structures, as in the case of radar absorbing materials.

The FDTD method deals with the differential form of the Maxwell equations:

$$\nabla \times \boldsymbol{E} = -\frac{\partial \boldsymbol{B}}{\partial t} \qquad (4.1a)$$

$$\nabla \times \boldsymbol{H} = \frac{\partial \boldsymbol{D}}{\partial t} + \boldsymbol{J} \qquad (4.1b)$$

$$\nabla \cdot \boldsymbol{D} = \rho \qquad (4.1c)$$

$$\nabla \cdot \boldsymbol{B} = 0 \qquad (4.1d)$$

where

$\boldsymbol{E}$: $electric\ field\ intensity\ vector\ (volts/meter)$
$\boldsymbol{H}$: $magnetic\ field\ intensity\ vector\ (amperes/meter)$
$\boldsymbol{D}$: $electric\ flux\ density\ vector\ (coulomb/meter^2)$
$\boldsymbol{B}$: $magnetic\ flux\ density\ vector\ (weber/meter^2)$

$\boldsymbol{J}$: $electric\ current\ density\ vector\ (amperes/meter^2)$
ρ : $electric\ charge\ density\ (coulomb/meter^3)$

Together with Maxwell equations, constitutive relations describing the material properties are also necessary for the solution of the electromagnetic problem. In linear, isotropic and non-dispersive mediums, these relations can be simply written as:

$$\boldsymbol{D} = \epsilon \boldsymbol{E}, \qquad \boldsymbol{B} = \mu \boldsymbol{H}, \qquad \boldsymbol{J} = \sigma \boldsymbol{E} \tag{4.2}$$

where

ϵ : $permittivity\ of\ the\ medium\ (farad/meter)$
μ : $permeability\ of\ the\ medium\ (henry/meter)$
σ : $conductivity\ of\ the\ medium\ (siemens/meter)$

For anisotropic materials, the permittivity and permeability parameters are tensors with complex values.

For the numeric solutions of Maxwell's equations by using finite difference scheme, in [34], Yee has introduced a cubic lattice to discretize the computational domain, which is called as *"Yee's unit cell".* The cell dimensions are denoted as $\Delta x, \Delta y\ and\ \Delta z$. The whole computation domain is filled with Yee's cells, and a grid point *(i, j, k)* is defined as:

$$(i, j, k) = (i\Delta x, j\Delta y, k\Delta z) \tag{4.3}$$

The Yee cell together with the nodes on which the fields are calculated is shown in Figure 4-1. As can be seen from the figure, electric fields are calculated in the middle of the cubic edges, while magnetic fields are calculated in center of the cubic surfaces, [36]. Each E-field component is surrounded by four circulating H-field components, and each H-field component is surrounded by four circulating E-field components.

Electric and magnetic field values are calculated sequentially in time. Let the time step be Δt, then the electric field components are calculated in time $n\Delta t$, while H-field components are calculated in time points $(n + 1/2)\Delta t$. Together with the grid notations, the field components subject to numeric solution can be symbolized as in eqn. 4.4.

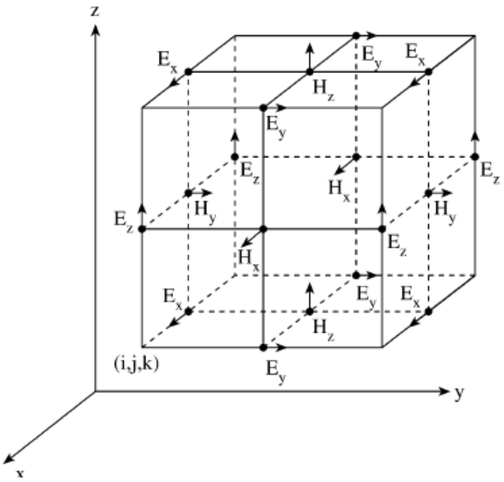

Figure 4-1 Electric and magnetic field vectors in a Yee's cubic cell (From [35])

$$E^{n}_{x,i-\frac{1}{2},j,k} \quad , \qquad E^{n}_{y,i,j-\frac{1}{2},k} \quad , \qquad E^{n}_{z,i,j,k-\frac{1}{2}} \tag{4.4a}$$

$$H^{n+\frac{1}{2}}_{x,i,j-\frac{1}{2},k-\frac{1}{2}} \quad , \qquad H^{n+\frac{1}{2}}_{y,i-\frac{1}{2},j,k-\frac{1}{2}} \quad , \qquad H^{n+\frac{1}{2}}_{z,i-\frac{1}{2},j-\frac{1}{2},k} \tag{4.4b}$$

With the above field component notations, by using the central difference scheme which has second-order accuracy, the curl equations given in equations 4.1a and 4.1b can be discretized by using the central difference scheme. The difference equations regarding the corresponding discretization are given in Appendix B.

In order to employ the time evolving process, the field components are initialized to zero for all the nodes of the computational domain. Then a time domain excitation signal is introduced to the domain. For the case of FSS and absorber characterizations, this excitation signal is chosen as an incident plane wave. At time $0.5\Delta t$, the magnetic field components are updated according to the equations 4.5a-c. Following the updates of H-components, at time Δt, the electric field components are calculated by using the equations 4.6a-c. This recursive calculation scheme is repeated until the field value at the observation points decays to a predefined level with respect to incident energy.

As can be seen, the major advantage of the FDTD is the lack of matrix inversion when compared to other numerical methods. On the other hand, the field storage for every time step is the main disadvantage of the method. However, if one is not interested in the field values of every grid at the end of the simulation, then the corresponding data storage is carried out for only observation points, such as ports of a waveguide structure, input terminals of an antenna, the grids on the observation plane for scattering analysis of periodic structures.

An important point in FDTD solutions is the stability condition to avoid numerical instability. As an explicit finite difference scheme, it is required that the time step, Δt, should be smaller than a certain value determined by the lattice dimensions. For three dimensional problems, according to Courant-Friedrich-Lewy (CFL) stability condition, [36], the upper limit for the time step is defined as:

$$\Delta t \leq \frac{1}{c\sqrt{\frac{1}{\Delta x^2}+\frac{1}{\Delta y^2}+\frac{1}{\Delta z^2}}} \tag{4.5}$$

4.2 Electromagnetic solutions of FSS layers and multi-layered absorbers by using FDTD

In the sub-section 4.1, the fundamental points of the FDTD method are explained. Detailed information concerning the FDTD scheme can be found in [35], [36], and [37]. In this section, the adaptation of the method for the scattering analysis of periodic structures (lossy FSS layers and circuit analog absorbers) is explained in detail.

In Figure 4-2, the computational domains for the characterization of FSS layers and multi-layered circuit analog absorbers are shown. The domains are similar to the unit cells used for the analysis of periodic structures in HFSS. The side walls of the cell are the boundaries on which the periodicity is imposed. PECs (perfect electric conductors) are used to truncate the domain in the direction of wave propagation. Adjacent to these PEC sheets, perfectly matched layers (PMLs) are deposited to simulate the open space condition for propagating waves. These are matched layers; they do not reflect the energy incident upon them. On the other hand, these mediums are lossy and they introduce attenuation to the propagating waves inside them. By this way, in other words without reflecting the incident energy and attenuating the penetrated energy to very low levels, PMLs are used to simulate the open boundary conditions. To introduce the excitation signal to the domain, excitation planes are used. At the positions of these planes, plane waves propagating in the direction where FSS layers exist, are introduced. Observation planes are used to sample the reflected and the transmitted energy. For FSS characterization, two observation planes exist to extract the S11 and S21 parameters, while for the case of absorbers, only one plane is present, since the only consideration is the reflectivity.

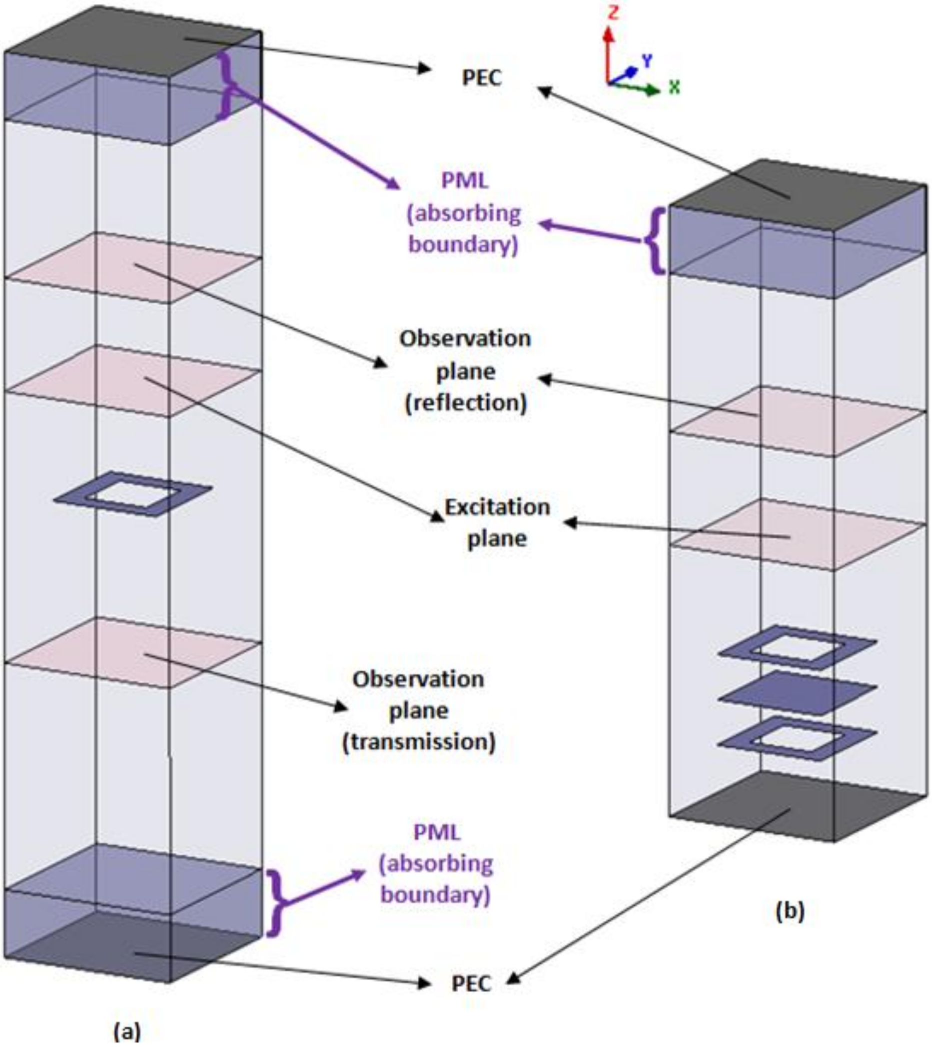

Figure 4-2 Computational domains used for: (a) characterization of lossy FSS layers, (b) reflectivity calculation of multi-layered circuit analog absorbers

The construction of the computational domain, employment of excitation and boundary conditions, and time evolving computation process will be explained over following sub-sections:

- Discretization of the computational domain,
- Discretization and modeling of FSS layers with predefined surface impedance values,
- Realization of periodic boundary conditions,
- Employment of PML regions,

- Excitation of plane wave source in the domain,
- Gathering of transmission and reflection parameters.

4.2.1 Discretization of the computational domain

To discretize the computational domain, as mentioned in FDTD fundamentals part, Yee's cubic lattices are used. These lattices are nothing but hexagonal meshes used to define the grids on which the electric and magnetic fields are calculated. In Figure 4-3, an illustrative computation domain discretized by hexagonal lattices is shown.

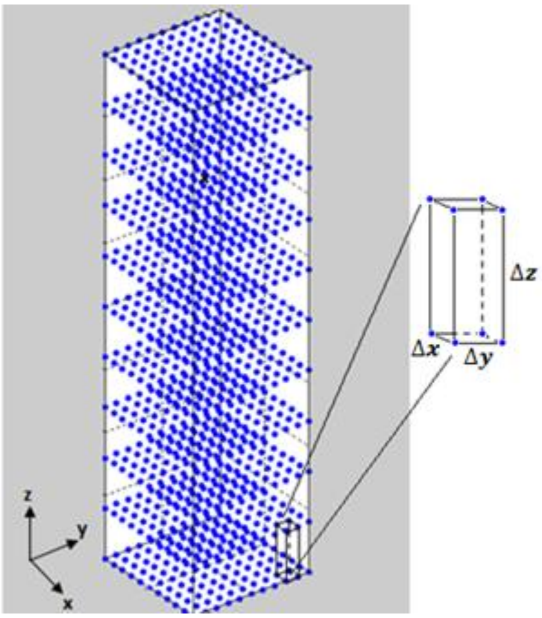

Figure 4-3 Discretization of the computational domain with hexagonal meshes

For the developed codes, the spatial increments Δx and Δy are kept equal for all simulations regardless of the simulated structure. On the other hand, the choice of Δz is kept as free from the transversal mesh dimension. Moreover, the spatial increments for all the meshes in the domain are same, in other words an adaptive discretization method is not used.

4.2.2 Discretization and modeling of FSS layers with predefined surface impedance values

Frequency selective surfaces are ideally patterned sheets with zero thickness. In order to introduce loss, these sheets are modeled by using real valued surface impedance values rather than perfectly conducting surfaces. To model these resistive layers in the time domain analysis, there are two alternative methods. The first method is to model the FSS layer with a sheet of zero thickness and assign proper impedance boundary condition on its surface. But, due to frequency nature of the surface impedance concept, in time domain, the relation between the tangential electric and magnetic fields on the surface of the sheet is represented by a convolution integral:

$$frequency\ domain: \qquad \boldsymbol{E}_{tan} = Z_s(\boldsymbol{n} \times \boldsymbol{H}_{tan}) \qquad (4.6a)$$

$$time\ domain: \qquad \boldsymbol{E}_{tan}(t) = Z_s(t) * \left(\boldsymbol{n} \times \boldsymbol{H}_{\tan}(t)\right) \qquad (4.6b)$$

In [38], Tesche has formulated a time domain integral equation based on this convolution integral. But, direct evaluation of the convolution integral is impractical due to the large computation time and field storage requirements. To overcome the computational difficulties, lots of studies have been conducted and they have been mainly focused on usage of some approximating functions to represent the time domain nature of the surface impedance. By using the corresponding approximation functions (exponential functions, rational functions, etc.), the convolution integral can be converted to closed form expressions which can be evaluated recursively. Example studies regarding this issue can be found in [39]-[43]. The other alternative method to model the conducting layers with predefined surface resistance values is to use sheets with finite thickness and finite conductivity, whose conductance is determined from the desired surface resistance value. For the validity of this method, the thickness of the modeled sheet should be very small when compared to skin depth of the conducting medium. However, when the FSS layer is modeled with a very thin sheet, the spatial increment of the lattice in which the FSS is positioned, results a very small time step value for the time evolving calculation of the fields according to the equation 4.7. This small time step value increases the simulation time. This problem can be illustrated as follow.

Assume that an FSS layer with a surface resistance value of 20 ohm/sq. is modeled at 4 GHz with a conducting sheet whose thickness is 1 mm. According to equation (2.14), the conductivity of the sheet should be

$$\sigma = \frac{1}{R_s t} = 50\ siemens/m$$

At 4 GHz, the skin depth of the medium with a conductivity value of 50 siemens/m is (form equation 2.13):

$$\delta = \sqrt{\frac{2}{(2\pi * 4 * 10^{9})(4\pi * 10^{-7})50}} = 0.8\ mm$$

Since the thickness of the modeled sheet is larger than the skin depth of the material, the finite thickness modeling will fail for the FSS characterization. To ensure the validity of the model, the thickness of the conductor should be decreased to very low values which results in very small time step values according to equation 4.7.

To overcome this problem, in [44], Maloney and Smith have proposed a subcell model for including thin sheets in the finite difference time domain simulations. By the introduced method, the restriction of the domain discretization which sets the spatial grid increment to be at least as small as the smallest physical feature (the thickness of the lossy FSS layers) in the solution space can be removed. With the gained advantage, storage requirements and the number of time steps needed are greatly reduced.

The main idea of the method proposed by Maloney and Smith is to define an interior electric field component normal to the sheet surface in the cells through which the sheet passes. With this newly defined field component, and by using average conductivity and permittivity values in these special cells, the unknowns of the finite difference equations given in 4.5 and 4.6 are modified only for the grids on the corresponding cells. By this way, the global lattice dimensions are not disturbed even if the sheet thickness is very small. To explain the approximation they have used, consider the thin material sheet ($\sigma_s, \epsilon_s, \mu_s = \mu_0$) located in free space (ϵ_0, μ_0), Figure 4-4.

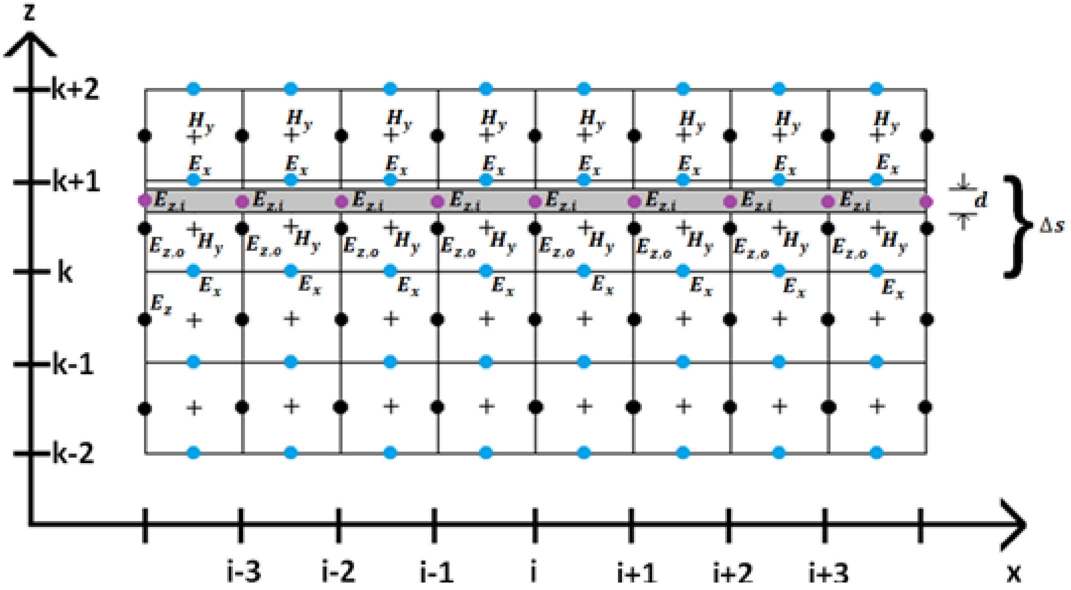

Figure 4-4 A slice of the three-dimensional rectangular FDTD grid showing the locations of the field components

As can be seen from Figure 4-4, usual interleaved grid is used for all the cells except the special cells through which the sheet passes. In this special cells, extra grid points are defined on which the z-directed electric fields interior to the conducting sheets will be calculated. In other words, the electric field oriented in the direction normal to the sheet surface is split into two parts in the special cells; $E_{z,i}$ and $E_{z,o}$, interior and exterior components respectively. The tangential components are not split since they are continuous across the boundary. Also the normal component of the magnetic field is not split since the conducting sheets are modeled as non-magnetic materials, $\mu_s = \mu_0$. The difference equations for the normal component of electric field are given by:

$$\begin{aligned}E_{z,o,(i,j,k+0.5)}^{n+1} &= E_{z,o,(i,j,k+0.5)}^{n} + \frac{\Delta t}{\epsilon_0 \Delta x}\left[H_{y,(i+0.5,j,k+0.5)}^{n+0.5} - H_{y,(i-0.5,j,k+0.5)}^{n+0.5}\right] \\ &\quad + \frac{\Delta t}{\epsilon_0 \Delta y}\left[H_{x,(i,j-0.5,k+0.5)}^{n+0.5} - H_{x,(i,j+0.5,k+0.5)}^{n+0.5}\right] \qquad (4.7a)\end{aligned}$$

$$\begin{aligned}E_{z,i,(i,j,k+0.5)}^{n+1} &= \left[\frac{1-\Delta t\dfrac{\sigma_s}{2\epsilon_s}}{1+\Delta t\dfrac{\sigma_s}{2\epsilon_s}}\right] E_{z,i,(i,j,k+0.5)}^{n} \\ &\quad + \left[\frac{\dfrac{\Delta t}{\epsilon_s \Delta x}}{1+\Delta t\dfrac{\sigma_s}{2\epsilon_s}}\right]\left[H_{y,(i+0.5,j,k+0.5)}^{n+0.5} - H_{y,(i-0.5,j,k+0.5)}^{n+0.5}\right] \\ &\quad + \left[\frac{\dfrac{\Delta t}{\epsilon_s \Delta y}}{1+\Delta t\dfrac{\sigma_s}{2\epsilon_s}}\right]\left[H_{x,(i,j-0.5,k+0.5)}^{n+0.5} - H_{x,(i,j+0.5,k+0.5)}^{n+0.5}\right] \qquad (4.7b)\end{aligned}$$

For the tangential components of the electric field, average conductivity and permittivity values are used:

$$\varepsilon^{avg} = \left(1 - \frac{d}{\Delta z}\right)\varepsilon_0 + \frac{d}{\Delta z}\varepsilon_s \qquad (4.8a)$$

$$\sigma^{avg} = \frac{d}{\Delta z}\sigma_s \qquad (4.8b)$$

$$\begin{aligned}E_{x,(i+0.5,j,k+1)}^{n+1} &= \left[\frac{1-\left(\Delta t\dfrac{\sigma^{avg}}{2\varepsilon^{avg}}\right)}{1+\left(\Delta t\dfrac{\sigma^{avg}}{2\varepsilon^{avg}}\right)}\right] E_{x,(i+0.5,j,k+1)}^{n} \\ &\quad + \left[\frac{\dfrac{\Delta t}{\varepsilon^{avg}\Delta z}}{1+\Delta t\dfrac{\sigma^{avg}}{2\epsilon^{avg}}}\right]\left[H_{y,(i+0.5,j,k+0.5)}^{n+0.5} - H_{y,(i+0.5,j,k+1.5)}^{n+0.5}\right] \\ &\quad + \left[\frac{\dfrac{\Delta t}{\varepsilon^{avg}\Delta y}}{1+\Delta t\dfrac{\sigma^{avg}}{2\epsilon^{avg}}}\right]\left[H_{z,(i+0.5,j+0.5,k+1)}^{n+0.5} - H_{z,(i+0.5,j-0.5,k+1)}^{n+0.5}\right] \qquad (4.8c)\end{aligned}$$

$$
\begin{aligned}
E^{n+1}_{y,(i,j+0.5,k+1)} = {} & \left[\frac{1-\left(\Delta t\,\dfrac{\sigma^{avg}}{2\varepsilon^{avg}}\right)}{1+\left(\Delta t\,\dfrac{\sigma^{avg}}{2\varepsilon^{avg}}\right)}\right] E^{n}_{y,(i,j+0.5,k+1)} \\
& + \left[\frac{\dfrac{\Delta t}{\varepsilon^{avg}\Delta z}}{1+\Delta t\,\dfrac{\sigma^{avg}}{2\epsilon^{avg}}}\right]\left[H^{n+0.5}_{x,(i,j+0.5,k+1.5)} - H^{n+0.5}_{x,(i,j+0.5,k-0.5)}\right] \\
& + \left[\frac{\dfrac{\Delta t}{\varepsilon^{avg}\Delta x}}{1+\Delta t\,\dfrac{\sigma^{avg}}{2\epsilon^{avg}}}\right]\left[H^{n+0.5}_{z,(i-0.5,j+0.5,k+1)} - H^{n+0.5}_{z,(i+0.5,j+0.5,k+1)}\right] \qquad (4.8d)
\end{aligned}
$$

The equation for the magnetic field normal to the sheet is the same as that for a non-special cell. For the tangential components, the update equations are:

$$
\begin{aligned}
H^{n+0.5}_{x,(i,j+0.5,k+0.5)} = {} & H^{n-0.5}_{x,(i,j+0.5,k+0.5)} \\
& + \frac{\Delta t}{\mu_0 \Delta y}\left[\left(1-\frac{d}{\Delta z}\right)\left[E^{n}_{z,o,(i,j,k+0.5)} - E^{n}_{z,o,(i,j+1,k+0.5)}\right]\right. \\
& \left. + \left(\frac{d}{\Delta z}\right)\left[E^{n}_{z,i,(i,j,k+0.5)} - E^{n}_{z,i,(i,j+1,k+0.5)}\right]\right] \\
& + \frac{\Delta t}{\mu_0 \Delta z}\left[E^{n}_{y,(i,j+0.5,k+1)} - E^{n}_{y,(i,j+0.5,k)}\right] \qquad (4.9a)
\end{aligned}
$$

$$
\begin{aligned}
H^{n+0.5}_{y,(i+0.5,j,k+0.5)} = {} & H^{n-0.5}_{y,(i+0.5,j,k+0.5)} \\
& + \frac{\Delta t}{\mu_0 \Delta x}\left[\left(1-\frac{d}{\Delta z}\right)\left[E^{n}_{z,o,(i+1,j,k+0.5)} - E^{n}_{z,o,(i,j,k+0.5)}\right]\right. \\
& \left. + \left(\frac{d}{\Delta z}\right)\left[E^{n}_{z,i,(i+1,j,k+0.5)} - E^{n}_{z,i,(i,j,k+0.5)}\right]\right] \\
& + \frac{\Delta t}{\mu_0 \Delta z}\left[E^{n}_{x,(i+0.5,j,k)} - E^{n}_{x,(i+0.5,j,k+1)}\right] \qquad (4.9b)
\end{aligned}
$$

In the developed FDTD codes, for the design of circuit analog absorbers, this second alternative is preferred for embedding of FSS layers into the solution domain. The surfaces are modelled with sheets whose thickness values are specified to be smaller than quarter of the smallest spatial increment of the global mesh.

As stated in 'dicretization of the computation domain' part, a global mesh is used for discretization of the whole domain and hence the spatial increments, $\Delta x, \Delta y, \Delta z$, do not change from cell to cell. Moreover, these increment values do not depend on the dimensions of the FSS layers, i.e. edge width/length of a crossed dipole type FSS. In such a case, it is highly probable that the FSS sheet is not properly discretized. As a result, offsets of the sheets from the grid nodes exist, as illustrated in Figure 4-5.

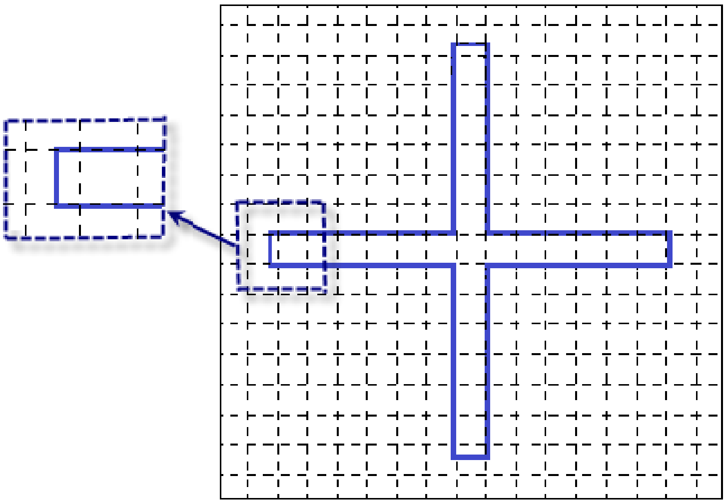

Figure 4-5 Illustration of the sheet offsets from the grid nodes due to usage of unique mesh sizes for discretization of the whole domain

When the edges of the FSS sheets do not coincide with the grid points, as illustrated in Figure 4-5, in the corresponding cells, the finite difference equations should be modified. Without perturbing the equations significantly, by using average conductivity and/or permittivity values, the corresponding cases can be handled. Some studies concerning this issue have been conducted and formulated in the literature, [45]-[47]. In the corresponding studies, different ways to define the average permittivity values by preserving the second order accuracy of the central difference scheme are introduced. But, none of the studies have covered the determination of the average conductivity for the case when one of the interfaces is a lossy medium. In these studies, both interfaces are taken as perfect dielectric mediums. For the case of absorber and lossy FSS simulations, the interface at the edge of the FSS sheet has a finite conductivity medium in one side. In a similar way used in the average permittivity calculation presented in [47], average conductivity has been derived for the case of lossy FSS interfaces. The corresponding derivations are given in Appendix C.

The case is illustrated in Figure 4-6 with normal and tangential electric field nodes at the sheet interface.

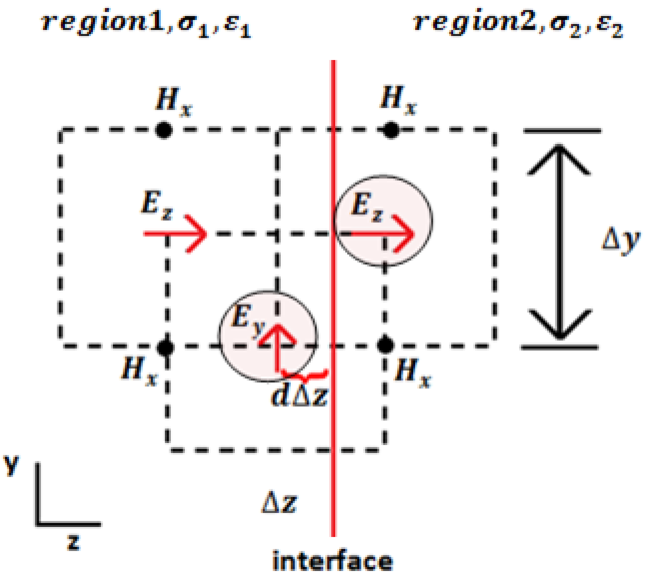

Figure 4-6 Placement of electric and magnetic field nodes near a dielectric interface for the case of 2-D $\mathbf{TE_x}$ polarization

In the special cells adjacent to the dielectric interface shown in Figure 4-6, the usual finite difference equations given in 4.5a-c are used for the magnetic fields since permeability values of both mediums are same. On the other hand, for the electric field components, the definitions of the conductivity and permittivity values used in 4.6a-c alter. For the case illustrated in Figure 4-6, the finite difference equation for the tangential component of the electric field is

$$E_{y,j,k}^{n+1} = \left[\frac{1-\left(\Delta t\frac{\sigma^*}{2\varepsilon^*}\right)}{1+\left(\Delta t\frac{\sigma^*}{2\varepsilon^*}\right)}\right]E_{y,j,k}^{n} + \left[\frac{\frac{\Delta t}{\varepsilon^*\Delta z}}{1+\Delta t\frac{\sigma^*}{2\epsilon^*}}\right]\left[H^{n+\frac{1}{2}}_{x,j,k+\frac{1}{2}} - H^{n+\frac{1}{2}}_{x,j,k-\frac{1}{2}}\right] \tag{4.10}$$

where

$$\sigma^* = \sigma_1\left(\frac{1}{2}+d\right)+\sigma_2\left(\frac{1}{2}-d\right) \tag{4.10a}$$

$$\varepsilon^* = \epsilon_1\left(\frac{1}{2}+d\right)+\epsilon_2\left(\frac{1}{2}-d\right) \tag{4.10b}$$

For the normal component of the electric field, as shown in Appendix-C, an average conductivity value could not be generated by preserving the second order accuracy of finite difference scheme. After some trials regarding the corresponding cells, it is discovered that usage of conductivity and permittivity values of the surrounding medium for the difference equations regarding normal component of the electric field in these cells yields most accurate solutions when referenced to HFSS outputs. Hence, the finite difference equation for the normal component of the electric field for the cells located at the medium-FSS interface:

$$\begin{aligned} E^{n+1}_{z,j+\frac{1}{2},k+\frac{1}{2}} = {} & \left[\frac{1-\left(\Delta t\frac{\sigma^*}{2\varepsilon^*}\right)}{1+\left(\Delta t\frac{\sigma^*}{2\varepsilon^*}\right)}\right]E^{n}_{z,j+\frac{1}{2},k+\frac{1}{2}} \\ & + \left[\frac{\frac{\Delta t}{\varepsilon^*\Delta z}}{1+\Delta t\frac{\sigma^*}{2\epsilon^*}}\right]\left[H^{n+\frac{1}{2}}_{x,j,k+\frac{1}{2}} - H^{n+\frac{1}{2}}_{x,j+1,k+\frac{1}{2}}\right] \end{aligned} \tag{4.11}$$

where

$$\sigma^* = \sigma_{surrounding\_medium} \tag{4.11a}$$

$$\varepsilon^* = \epsilon_{surrounding\_medium} \tag{4.11b}$$

With these average conductivity and permittivity values defined at the sheet interfaces, a great simplification for the domain discretization is achieved.

4.2.3 Realization of periodic boundary conditions

Frequency selective surfaces and circuit analog absorbers are periodic in their nature. Simulations regarding these structures are carried out by modeling a single period of the pattern. In FDTD simulations, as in the case of HFSS (FEM) simulations, unit cell concept is used for the analysis of a single period.

For a unit cell with periodicity *D* along the x-direction, electromagnetic fields at the two boundaries at $x = 0,$ and $x = D$ satisfy the following equations in frequency domain, which are also given in 2.22a-b:

$$\boldsymbol{E}(x = 0, y, z) = \boldsymbol{E}(x = D, y, z)e^{jk_x D} \qquad (4.12a)$$

$$\boldsymbol{H}(x = 0, y, z) = \boldsymbol{H}(x = D, y, z)e^{jk_x D} \qquad (4.12b)$$

For the case of scattering analysis of FSS and absorbers, the propagation constant along the x direction is:

$$k_x = k_0 \sin(\theta) \cos{(\varphi)} \qquad (4.13)$$

If we convert (4.14) to the time domain by using the Fourier transformation, we obtain:

$$\boldsymbol{E}(x = 0, y, z, t) = \boldsymbol{E}\left(x = D, y, z, t + \frac{D \sin(\theta) \cos{(\varphi)}}{c}\right) \qquad (4.14a)$$

$$\boldsymbol{H}(x = 0, y, z, t) = \boldsymbol{H}\left(x = D, y, z, t + \frac{D \sin(\theta) \cos{(\varphi)}}{c}\right) \qquad (4.14b)$$

For the case of oblique incidence simulations, which θ is not zero, for the update of electric and magnetic fields in current time (t), the field data in the future time $(t + \frac{D\sin(\theta)\cos{(\varphi)}}{c})$ are needed, opposing the casual relation in the time domain simulation. But, as stated in Chapter 3, the main consideration of the studies regarding the thesis is focused on specular reflection for the normal incidence case. In normal incidence case, $\theta = 0$, hence (4.16a) and (4.16b) yields

$$\boldsymbol{E}(x = 0, y, z, t) = \boldsymbol{E}(x = D, y, z, t) \tag{4.15a}$$

$$\boldsymbol{H}(x = 0, y, z, t) = \boldsymbol{H}(x = D, y, z, t) \tag{4.15b}$$

The periods of the absorbers designed in the studies are defined to be square to obtain a reflectivity characteristic independent from the polarization of the incoming wave. Hence, the boundary conditions along the y direction can be written similarly as

$$\boldsymbol{E}(x, y = 0, z, t) = \boldsymbol{E}(x, y = D, z, t) \tag{4.16a}$$

$$\boldsymbol{H}(x, y = 0, z, t) = \boldsymbol{H}(x, y = D, z, t) \tag{4.16b}$$

For the oblique incidence case in FDTD simulations, sine-cosine technique [48] or constant k_x method [49]-[50] can be used.

4.2.4 Employment of PML regions

In scattering problems, the radiated and scattered fields propagate to infinity. Hence, for perfect representation of the electromagnetic scenario, the computational domain should extend to infinity, ideally. Since this is impractical to implement, one should truncate the domain by using proper boundary conditions. These boundary conditions should be realized such that the reflected field should be eliminated when the radiated or scattered fields arrive on these boundaries. There are two alternative groups for the candidate boundary conditions. The first one is a radiation boundary condition based on travelling wave equations [51]-[52]. The other type of absorbing boundary condition is perfectly matched layers (PML) [36], [53]-[54]. This technique is based on the use of artificial layers appropriately designed to absorb the electromagnetic waves without significant reflection. For the analysis of periodic structures by using FDTD method, the second method is preferred owing to its simplicity.

For the case of FSS and circuit analog absorbers, the main consideration during the thesis studies is the normal incidence case as mentioned before. Hence, the wave propagation is realized in only one direction, along the z-axis. Owing to this concept, one-dimensional (1-D) perfectly matched layers are used for the FDTD simulations.

To illustrate the case, the interface between the PML region and the free space is shown in Figure 4-7.

The constitutive parameters of the PML region are:

$$\epsilon^*_{PML} = \epsilon_{PML} + \frac{\sigma^e_{PML}}{j\omega} \tag{4.17a}$$

$$\mu^*_{PML} = \mu_{PML} + \frac{\sigma^m_{PML}}{j\omega} \tag{4.17b}$$

where σ^e_{PML} is the electric conductivity, and σ^e_{PML} is the magnetic conductivity of the PML region.

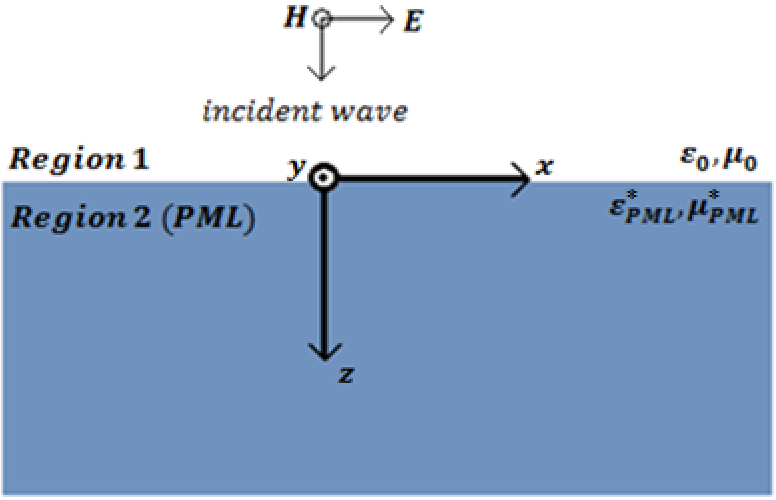

Figure 4-7 A plane wave normally incident on an interface between the PML and air

The incident fields can be written as:

$$\boldsymbol{E}^i = \boldsymbol{a_x} E_0 e^{-jk_0 z} \tag{4.18a}$$

$$\boldsymbol{H}^i = \boldsymbol{a_y} \frac{E_0}{\eta_0} e^{-jk_0 z} \tag{4.18b}$$

$$\eta_0 = \sqrt{\frac{\mu_0}{\epsilon_0}}\,, \qquad k_0 = \omega\sqrt{\mu_0\epsilon_0} \tag{4.18c}$$

When the incident field impinges on the interface, part of the energy is reflected back to the medium 1, while part of it is transmitted into region 2. The reflected and transmitted waves can be written as:

$$\boldsymbol{E}^r = \boldsymbol{a_x}\Gamma E_0 e^{jk_0 z}\,,\ \ \boldsymbol{H}^r = -\boldsymbol{a_y}\Gamma\frac{E_0}{\eta_0}e^{jk_0 z} \tag{4.19a}$$

$$\boldsymbol{E}^t = \boldsymbol{a_x}\tau E_0 e^{-jk_{PML}z}\,,\ \ \boldsymbol{H}^t = \boldsymbol{a_y}\tau\frac{E_0}{\eta_{PML}}e^{-jk_{PML}z} \tag{4.19b}$$

$$\eta_{PML} = \sqrt{\frac{\mu_{PML}^*}{\epsilon_{PML}^*}}\,, \qquad k_{PML} = \omega\sqrt{\mu_{PML}^*\epsilon_{PML}^*} \tag{4.19c}$$

where τ, Γ are transmission and reflection coefficients defined at the interface, respectively, [36]. The reflection coefficient at the interface is:

$$\Gamma = \frac{\eta_0 - \eta_{PML}}{\eta_0 + \eta_{PML}} = \frac{\sqrt{\frac{\mu_0}{\epsilon_0}} - \sqrt{\left(\frac{\mu_{PML}}{\epsilon_{PML}}\right)\frac{1+\frac{\sigma_{PML}^m}{j\omega\mu}}{1+\frac{\sigma_{PML}^e}{j\omega\epsilon}}}}{\sqrt{\frac{\mu_0}{\epsilon_0}} + \sqrt{\left(\frac{\mu_{PML}}{\epsilon_{PML}}\right)\frac{1+\frac{\sigma_{PML}^m}{j\omega\mu}}{1+\frac{\sigma_{PML}^e}{j\omega\epsilon}}}} \tag{4.20}$$

If the following conditions are satisfied

$$\epsilon_{PML} = \epsilon_0\,,\ \ \mu_{PML} = \mu_0 \tag{4.21a}$$

$$\frac{\sigma_{PML}^m}{\mu} = \frac{\sigma_{PML}^e}{\epsilon} \tag{4.21b}$$

Then, the reflection coefficient Γ equals to zero, resulting in reflectionless interface between the PML region and air.

With the constitutive parameters set above, the transmitted fields in the PML region can be written as:

$$\eta_{PML} = \eta_0\,, \qquad k_{PML} = k_0 - j\sigma_{PML}^{e}\eta_0 \tag{4.22a}$$

$$\boldsymbol{E}^{t} = \boldsymbol{a_x} E_0 e^{-jk_0 z} e^{-\sigma_{PML}^{e}\eta_0 z} \tag{4.22b}$$

$$\boldsymbol{H}^{t} = \boldsymbol{y}\frac{E_0}{\eta_0} e^{-jk_0 z} e^{-\sigma_{PML}^{e}\eta_0 z} \tag{4.22c}$$

The transmitted fields decay exponentially, with an attenuation constant of $\sigma_{PML}^{e}\eta_0$. After a certain distance, the field strength in the PML region approaches zero. Furthermore, if the PML region is truncated with a perfectly conducting sheet at the domain truncation side, the reflected fields from this PEC sheet will further be exposed to the attenuation introduced by the PML region. Hence the effective thickness of the absorbing medium is twice as its physical thickness. In summary, zero reflection at the interface and attenuation in the lossy medium constitute the key points of the perfectly matched layers.

While implementing these PML regions in FDTD, usage of the average conductivity concept at the PML interface cause noticeable error in the simulations. To compensate this phenomenon, a PML conductivity declaration with an increasing value from the interface to deep zones of the region should be used. With a polynomial distribution to set up the conductivity as:

$$\sigma_{PML}^{e}(x) = (x/l)^{m}\sigma_{max}^{e} \tag{4.23}$$

the numerical errors can be significantly reduced, where l is the thickness of the PML region [36].

4.2.5 Excitation of plane wave source in the domain

For scattering analysis in FDTD (also in other types of numeric analysis), a plane wave source is needed to illuminate the structure under observation. Plane wave source is a distributed source, where the excitation signal is incorporated on a virtual surface in the computation domain. The corresponding surface is shown in Figure 4-2, and labeled as 'excitation planes'. With the corresponding surface, the computation domain is split into two regions, total field region and scattered field region, namely. In total-field region, YEE algorithm operates on total field vector components, including the propagating fields of the incident wave as well as those of the scattered fields. The interacting structure is embedded in this region. On the other hand, in scattered field region, Yee algorithm operates only on the scattered fields. Hence, there is no incident field component in this region. This region is the place where the scattered fields are sampled to characterize the illuminated structure. The excitation of plane wave in the computation domain will be explained over a one dimensional example for simplicity, as illustrated in Figure 4-8.

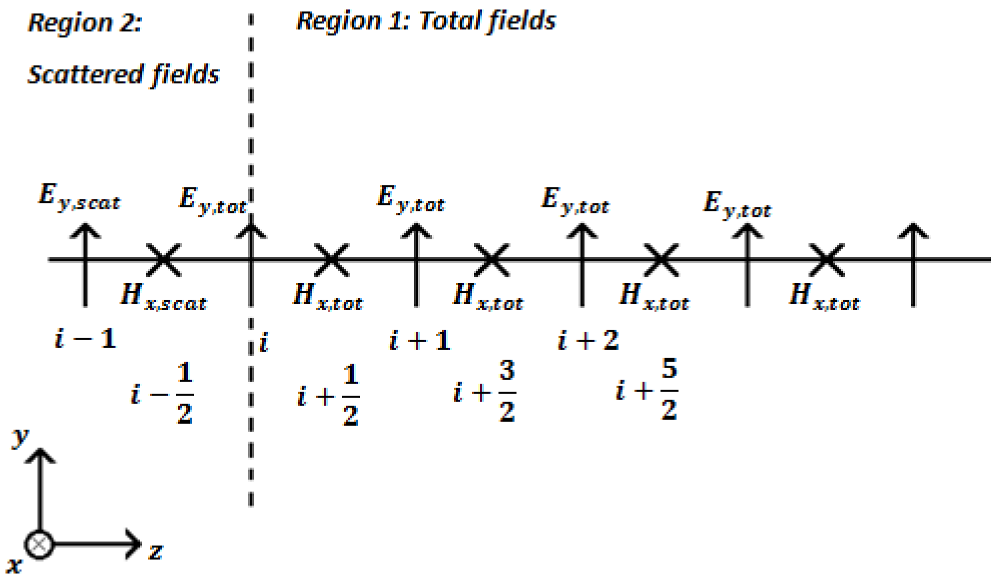

Figure 4-8 Field component locations adjacent to virtual excitation plane

If we blindly write the finite difference equation for the magnetic field component at node $i-\frac{1}{2}$, shown in Figure 4-8

$$H_{x,scat}\Big|_{i-\frac{1}{2}}^{n+\frac{1}{2}} = H_{x,scat}\Big|_{i-\frac{1}{2}}^{n-\frac{1}{2}} + \frac{\Delta t}{\mu_0 \Delta z}\left[E_{y,tot}\big|_i^n - E_{y,scat}\big|_{i-1}^n\right] \tag{4.24}$$

As (4.26) stands, it is an incorrect operation, since unlike electric fields in the brackets are subtracted. To correct the formulation, known incident electric field component at node i should be added to the relation to yield

$$H_{x,scat}\Big|_{i-\frac{1}{2}}^{n+\frac{1}{2}} = \underbrace{H_{x,scat}\Big|_{i-\frac{1}{2}}^{n-\frac{1}{2}}}_{\substack{stored\ in \\ computer \\ memory}} + \frac{\Delta t}{\mu_0 \Delta z} \underbrace{\left[E_{y,tot}\big|_i^n - E_{y,scat}\big|_{i-1}^n\right]}_{\substack{stored\ in \\ computer \\ memory}} - \frac{\Delta t}{\mu_0 \Delta z} \underbrace{E_{y,inc}\big|_i^n}_{\substack{known \\ quantity}} \tag{4.25}$$

In a similar manner, the difference equation for the electric field component at node i, can be given as:

$$E_{y,tot}\big|_i^{n+1} = \underbrace{E_{y,tot}\big|_i^n}_{\substack{stored\ in \\ computer \\ memory}} + \frac{\Delta t}{\epsilon_0 \Delta z} \underbrace{\left[H_{x,tot}\Big|_{i+\frac{1}{2}}^{n+\frac{1}{2}} - H_{x,scat}\Big|_{i-\frac{1}{2}}^{n+\frac{1}{2}}\right]}_{\substack{stored\ in \\ computer \\ memory}} - \frac{\Delta t}{\epsilon_0 \Delta z} \underbrace{H_{x,inc}\Big|_{i-\frac{1}{2}}^{n+\frac{1}{2}}}_{\substack{known \\ quantity}} \tag{4.26}$$

The overall effect of (4.27) and (4.28) is to generate a plane wave at the scattered-field/total-field interface point i, and propagate it through the total field zone [37].

The time domain signal should be generated to cover the frequency band of interest. A popular waveform for the excitation signal is a sine wave modulated with a Gaussian waveform [36]:

$$f(t) = \mathrm{e}^{\left[-\frac{(\mathrm{t}-\mathrm{t}_0)^2}{2\sigma_\mathrm{t}^2}\right]} \cos(2\pi \mathrm{f}_0 \mathrm{t}) \tag{4.27}$$

where

σ_t : *pulse width*

t_0 : *time delay used for a smart start in time domain excitation (between* $3\sigma_t$ *and* $5\sigma_t$*)*

f_0 : *center frequency*

The signal magnitude of the frequency spectrum of the excitation signal at $f_0 + \frac{BW}{2}$ is 40 dB lower than the signal magnitude at center frequency with the following bandwidth definition:

$$BW * 2\pi = 2 * \frac{3}{\sigma_t} \tag{4.28}$$

4.2.6 Gathering of transmission and reflection parameters

The final step of the scattering analysis is the extraction of characteristic parameters, including reflection and transmission coefficients. For FSS simulations, as shown in Figure 4-2, in the computation domain there are two observation planes to store the reflected and transmitted energy, respectively. For the case of absorber simulations, there exist only one observation plane to sample the reflected fields. Stored time domain signals are integrated on these observation planes:

$$E_{co-polarized}^{transmitted}(t) = \frac{1}{N_x N_y} \sum_{i=1}^{N_x} \sum_{j=1}^{N_y} E_{co-polarized}^{transmitted}\left(i, j, k_{transmission-plane}, t\right) \tag{4.29a}$$

$$E_{co-polarized}^{reflected}(t) = \frac{1}{N_x N_y} \sum_{i=1}^{N_x} \sum_{j=1}^{N_y} E_{co-polarized}^{reflected}\left(i, j, k_{reflection-plane}, t\right) \tag{4.29b}$$

For frequency domain characterization of the simulated structure, N-point discrete Fourier transforms (DFT) of the sampled time domain signals are taken:

$$E_{co-polarized}^{transmitted}(k) = \sum_{i=1}^{N} E_{co-polarized}^{transmitted}(t)\, e^{\left(\frac{2\pi j}{N}\right)(k-1)(i-1)} \tag{4.30a}$$

$$E_{co-polarized}^{reflected}(k) = \sum_{i=1}^{N} E_{co-polarized}^{reflected}(t)\, e^{\left(\frac{2\pi j}{N}\right)(k-1)(i-1)} \tag{4.30b}$$

$$E_{co-polarized}^{incident}(k) = \sum_{i=1}^{N} E_{co-polarized}^{incident}(t)\, e^{\left(\frac{2\pi j}{N}\right)(k-1)(i-1)} \tag{4.30c}$$

with the following frequency domain parameters

$$f_{max} = \frac{1}{\Delta t} : upper\ edge\ of\ the\ frequency\ band \tag{4.30d}$$

$$\Delta f = \frac{f_{max}}{N} : frequency\ increment \tag{4.30e}$$

The reflection and transmission coefficients can be extracted as:

$$\Gamma = \frac{E_{co-polarized}^{reflected}(f)}{E_{co-polarized}^{incident}(f)} e^{j2\pi f \Delta d_{inc-ref}} \tag{4.31a}$$

$\Delta d_{inc-ref}$: *sum of the distances between the excitation plane and front face of the simulated structure and the one between observation plane regarding the reflected fields and the front face of the simulated structure*

$$T = \frac{E_{co-polarized}^{transmitted}(f)}{E_{co-polarized}^{incident}(f)} e^{j2\pi f \Delta d_{inc-trans}} \tag{4.31b}$$

$\Delta d_{inc-trans}$: *distance between the excitation plane and observation plane regarding the transmitted fields*

4.2.7 Verification of the developed FDTD codes

To verify the FDTD codes developed for the design of circuit analog absorber, three types of FSSs and the two absorbers designed in Chapter 3 are simulated with both HFSS and the corresponding code.

The first FSS to be verified is a crossed dipole with a period of 9.6 mm and whose dimensions together with the surface resistance value are shown below, in Figure 4-9.

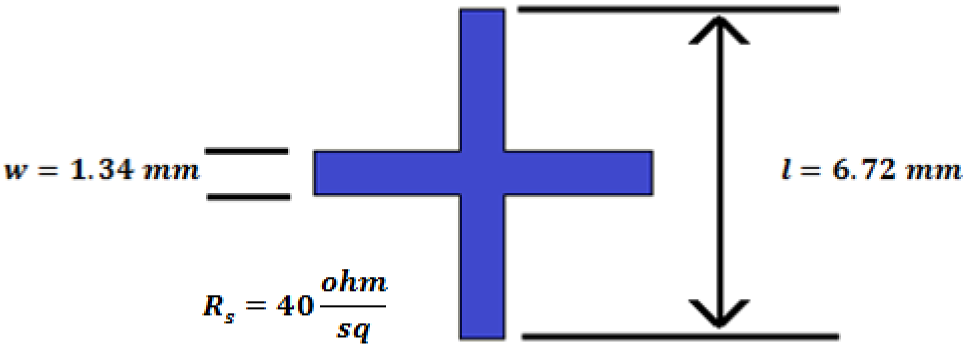

Figure 4-9 The crossed dipole type lossy FSS to be simulated

Table 4-1 FDTD parameters used in the electromagnetic solutions of the FSS given in Figure 4-9

$frequency\ band$	5-25 GHz
$\Delta x = \Delta y$	0.2 mm
Δz	0.4 mm
Δt	$\frac{0.85}{c\sqrt{\frac{1}{\Delta x^2}+\frac{1}{\Delta y^2}+\frac{1}{\Delta z^2}}}$
$thickness\ of\ the\ PML\ regions$	10 mm
$distanceof\ the\ PML\ region\ to\ nearest\ observation\ plane$	8 mm
$thickness\ of\ the\ FSS\ sheets$	0.05 mm
σ_{max}^{PML}	$5\frac{siemens}{m}$
ϵ_{FSS}	ϵ_0
σ_{FSS}	$\frac{1}{(0.05\cdot 10^{-3})40} = 500\frac{siemens}{m}$
$distance\ of\ the\ excitation\ plane\ to\ the\ FSS$	8 mm
$distance\ of\ the\ observation\ planes\ to\ excitation\ plane\ or\ FSSs$	8 mm

The results regarding S-parameters of the simulated structure are compared in Figure 4-10, Figure 4-11 and Figure 4-12.

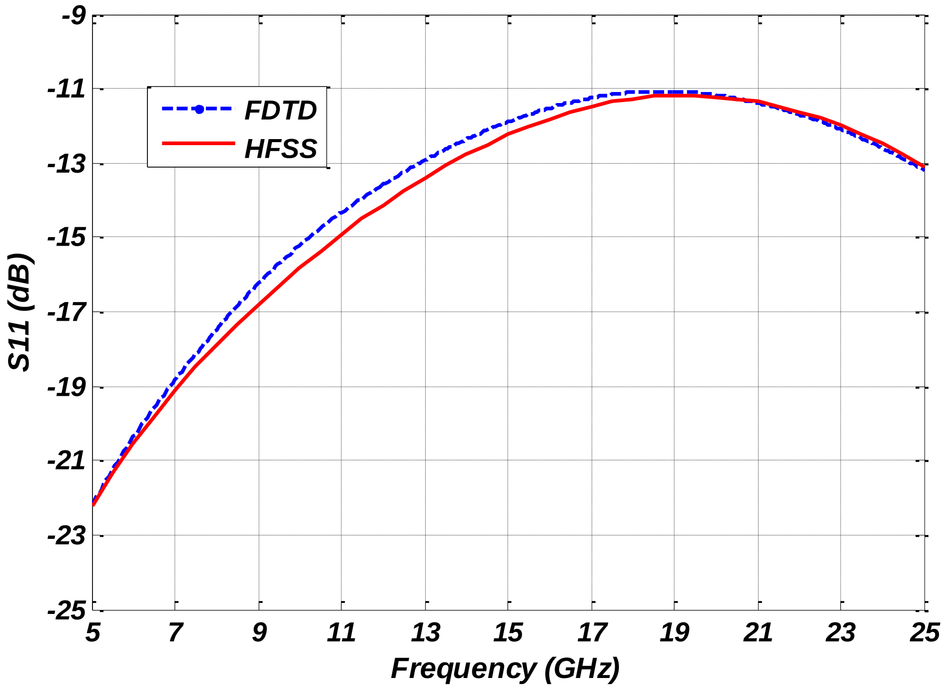

Figure 4-10 Comparison of FDTD code and HFSS in terms of return loss of crossed dipole type FSS

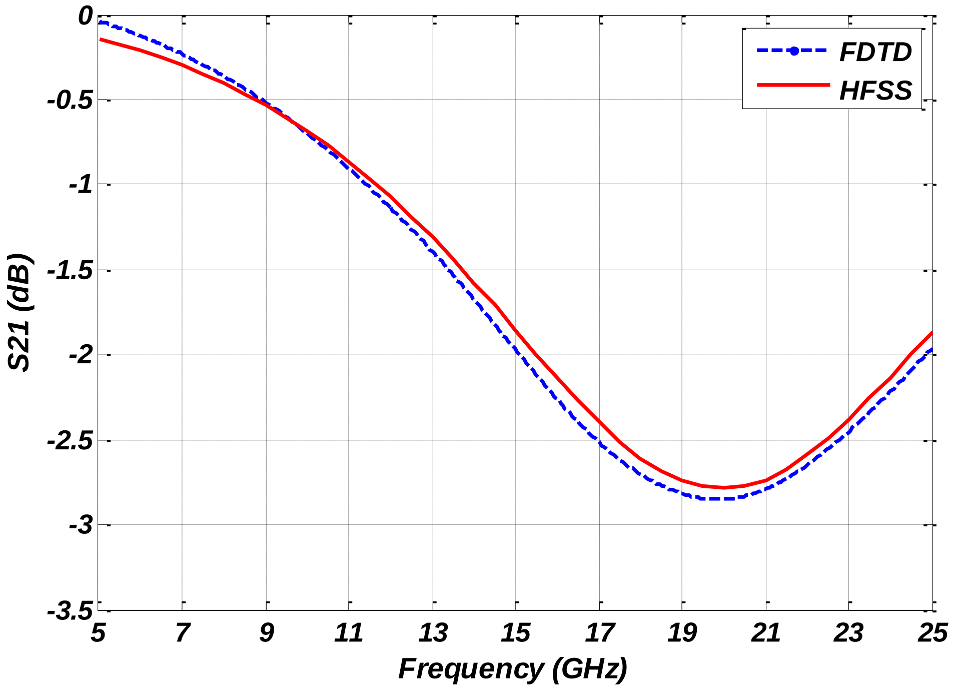

Figure 4-11 Comparison of FDTD code and HFSS in terms of insertion loss of crossed dipole type FSS

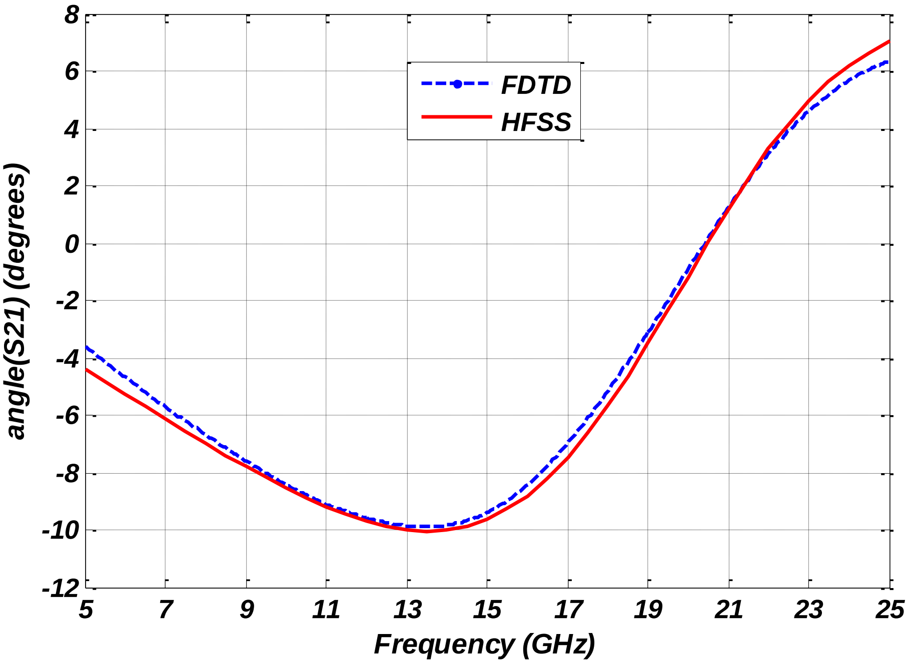

Figure 4-12 Comparison of FDTD code and HFSS in terms of insertion phase of crossed dipole type FSS

The second type FSS to be used for the verification of the FDTD code is square patch. The patch dimensions together with the surface resistance value of the FSS are given in Figure 4-13. The period of the FSS is 8 mm. The parameters regarding FDTD scheme are same as the ones used for the analysis of crossed dipole type FSS except

$$\sigma_{FSS} = \frac{1}{(0.05 \cdot 10^{-3})100} = 200\frac{siemens}{m}$$

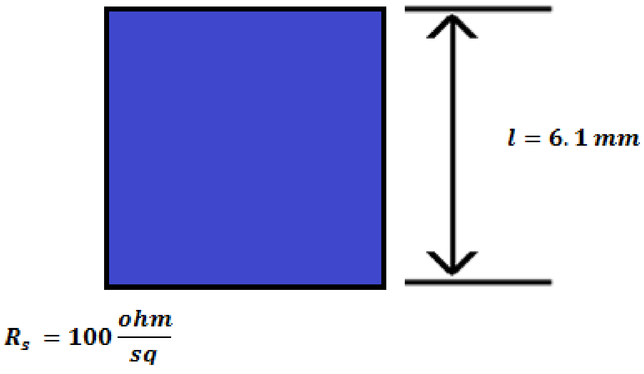

Figure 4-13 The square patch type lossy FSS to be simulated

The results regarding S-parameters of the simulated patch type FSS are compared in Figure 4-14, Figure 4-15 and Figure 4-16.

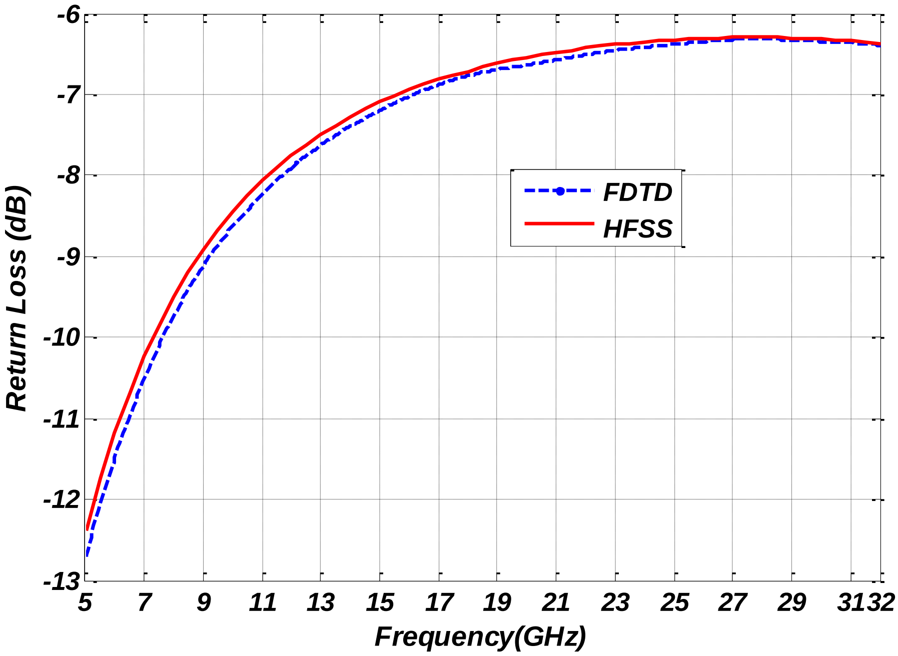

Figure 4-14 Comparison of FDTD code and HFSS in terms of return loss of patch type FSS

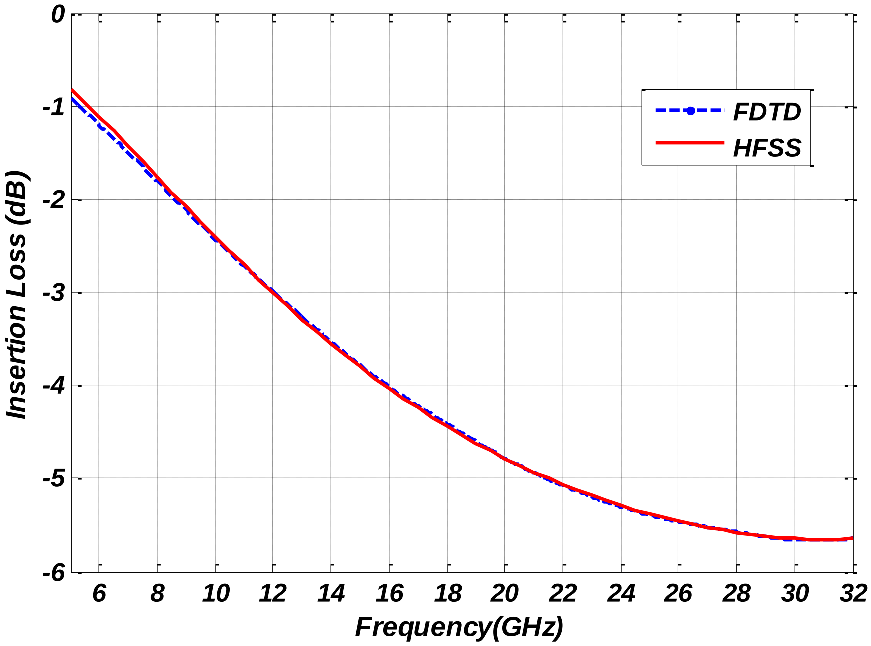

Figure 4-15 Comparison of FDTD code and HFSS in terms of insertion loss of patch type FSS

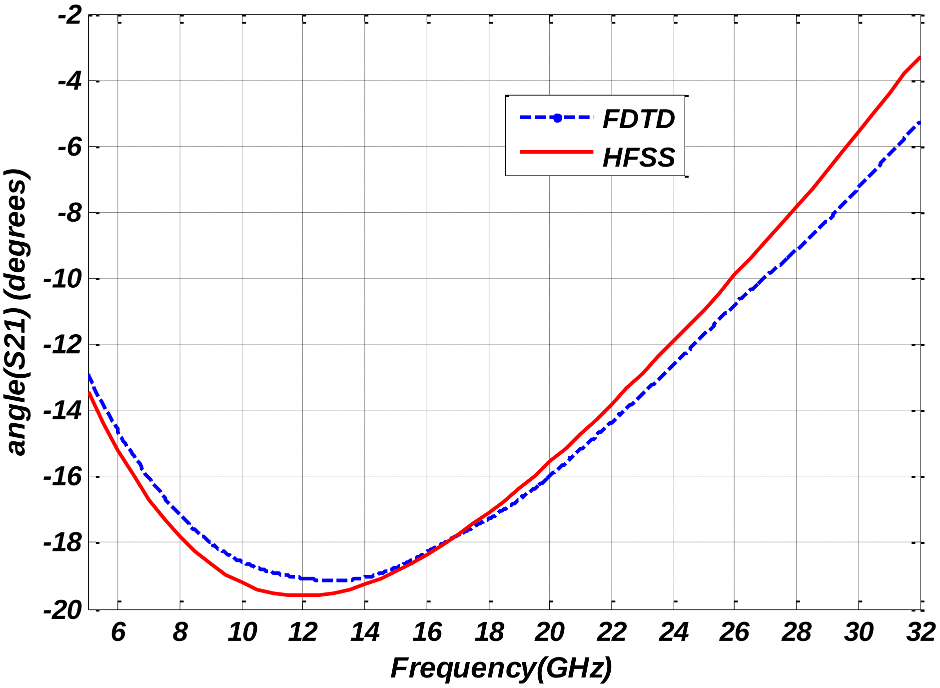

Figure 4-16 Comparison of FDTD code and HFSS in terms of insertion phase of patch type FSS

The final FSS type to be simulated for the verification purposes of the FDTD code is the square ring with characteristics shown in Figure 4-17. The corresponding simulation is realized over a perfectly conducting structure, to ensure that the FDTD code is valid for the analysis of lossless FSSs which is used in FSS characterization step of the developed method. The period is determined as 28 mm. Also, the FDTD parameters set during the analysis are shown below.

$$\Delta x = \Delta y = 0.5\,mm \;\;;\;\; \Delta z = 1\,m \;\;;\;\; \Delta t = \frac{0.85}{c\sqrt{\frac{1}{\Delta x^2}+\frac{1}{\Delta y^2}+\frac{1}{\Delta z^2}}}$$

$thickness\ of\ the\ PML\ region : 10\,mm$

$distanceof\ the\ PML\ region\ to\ nearest\ observation\ planes: 8\,mm$

$thickness\ of\ the\ FSS\ sheet: 0.05\,mm$

$$\sigma_{max}^{PML} = 5\frac{siemens}{m} \;\;;\;\; \epsilon_{FSS} = \epsilon_0 \;\;;\;\; \sigma_{FSS} = 10^8$$

$distance\ of\ the\ excitation\ plane\ to\ the\ FSS :\ 8\,mm$

$distance\ of\ the\ observation\ planes\ to\ excitation\ plane\ or\ FSS\colon 8\ mm$

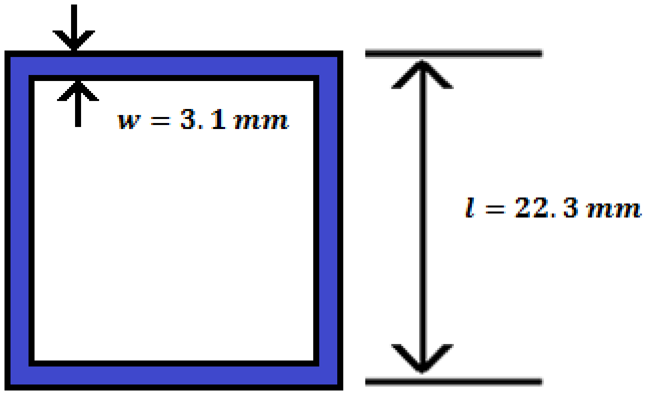

$$R_s = 0\frac{ohm}{sq}\ (PEC)$$

Figure 4-17 The square ring type perfectly conducting FSS to be simulated

The results regarding S-parameters of the simulated square ring type FSS are compared in Figure 4-18, Figure 4-19 and Figure 4-20.

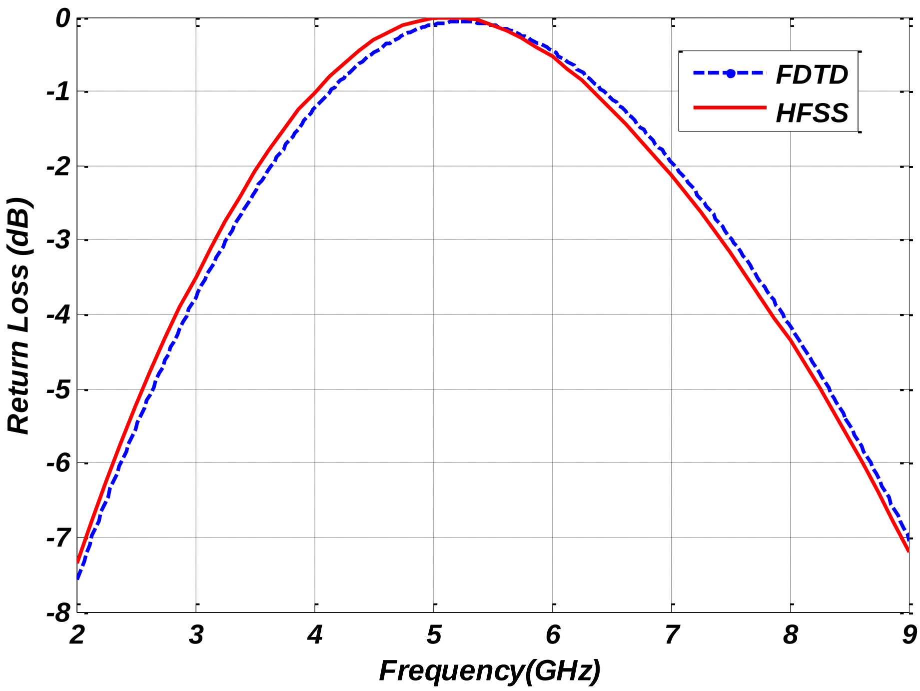

Figure 4-18 Comparison of FDTD code and HFSS in terms of return loss of square ring type FSS

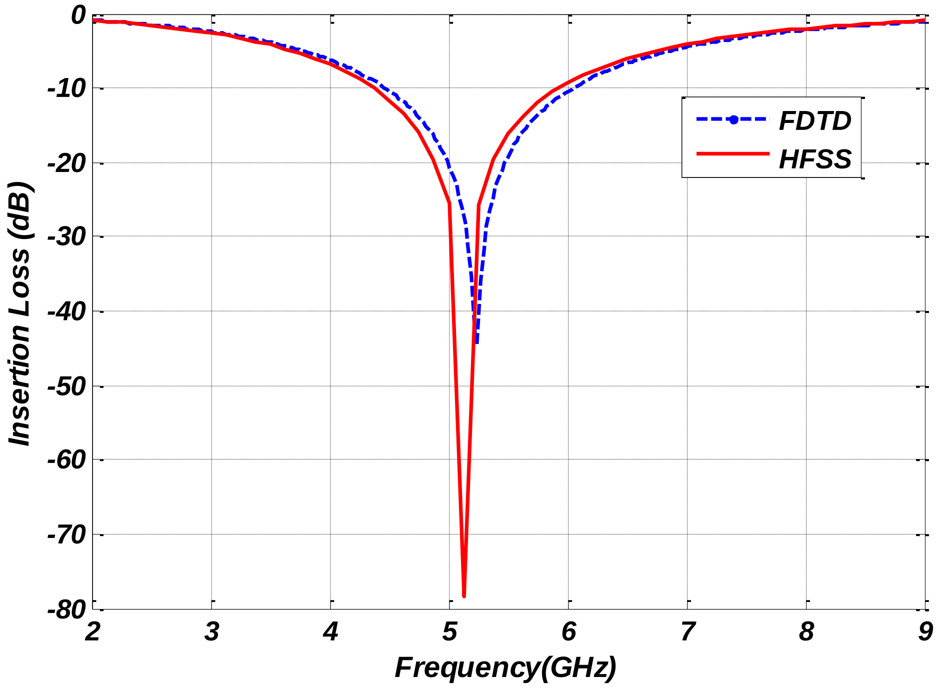

Figure 4-19 Comparison of FDTD code and HFSS in terms of insertion loss of square ring type FSS

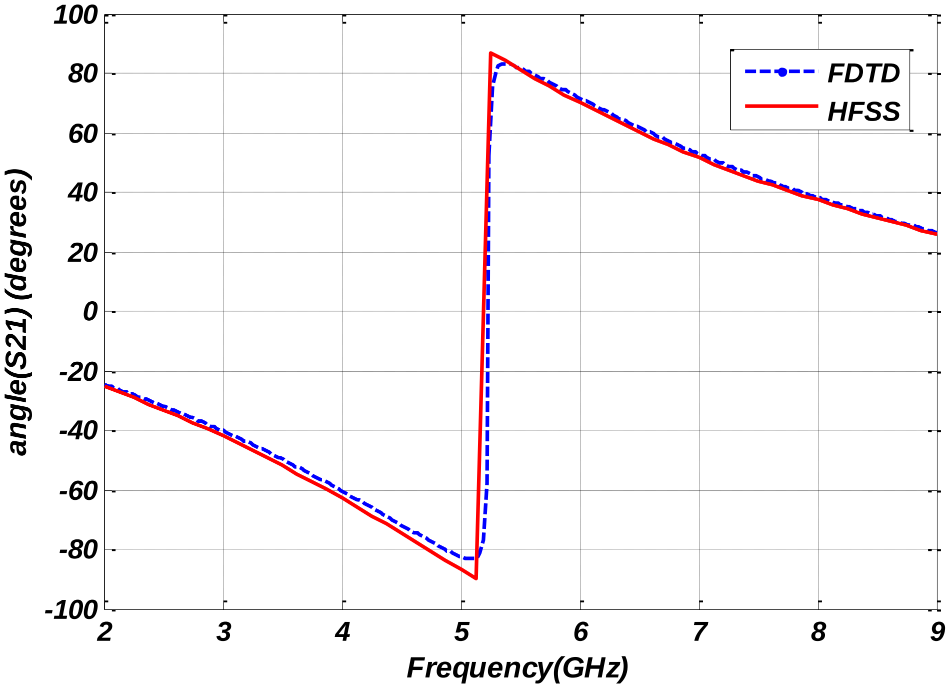

Figure 4-20 Comparison of FDTD code and HFSS in terms of insertion phase of square ring type FSS

As can be seen from the figures representing the S-parameters of the three FSS types, the results of the developed FDTD codes for the simulation and characterization of both PEC and lossy FSS structures are quite consistent with the results obtained by HFSS, which uses FEM. In order to show the consistency regarding multilayered absorbers, two circuit analog absorbers designed by the method proposed in Chapter 3 are also compared in terms of reflectivity characteristics. The HFSS models of the absorbers are shown in Figure 4-21. The FDTD parameters used in the solutions of the corresponding absorbers are given in Table 4-2.

The reflectivity characteristics of the corresponding absorbers obtained by HFSS and the developed codes are compared in Figure 4-22 and Figure 4-23.

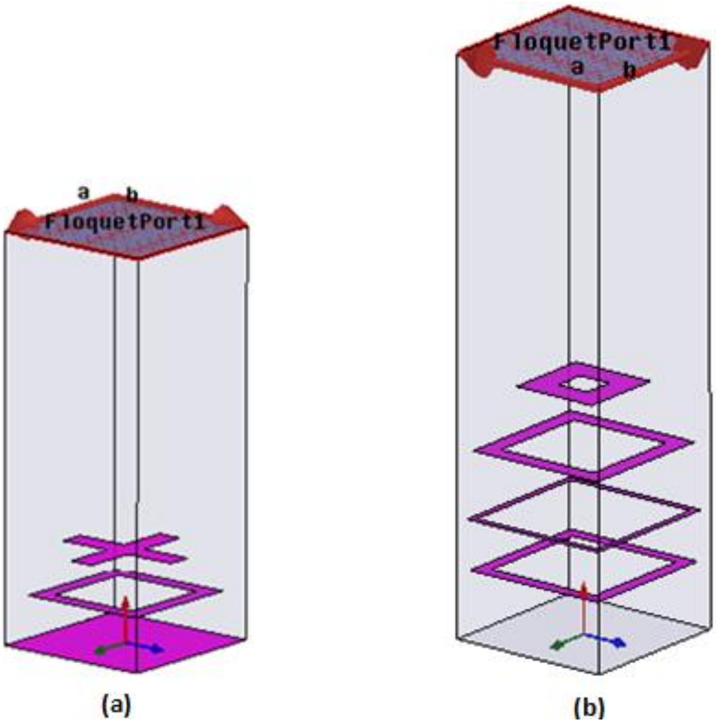

Figure 4-21 HFSS models of the designed circuit analog absorbers: (a) design-1, (b) design-2

Table 4-2 FDTD parameters used in the electromagnetic solutions of absorbers given in Figure 4-21

frequency band	10-32 GHz	4-50 GHz
$\Delta x = \Delta y$	0.2 mm	0.1 mm
Δz	0.4 mm	0.2 mm
Δt	$\frac{0.85}{c\sqrt{\frac{1}{\Delta x^2}+\frac{1}{\Delta y^2}+\frac{1}{\Delta z^2}}}$	$\frac{0.85}{c\sqrt{\frac{1}{\Delta x^2}+\frac{1}{\Delta y^2}+\frac{1}{\Delta z^2}}}$
thickness of the PML regions	8 mm	10 mm
distanceof the PML region to nearest observation plane	8 mm	8 mm
thickness of the FSS sheets	0.05 mm	0.05 mm
σ_{max}^{PML}	$5\frac{siemens}{m}$	$5\frac{siemens}{m}$
ϵ_{FSS}	ϵ_0	ϵ_0
distance of the excitation plane to the FSS	8 mm	8 mm
distance of the observation planes to excitation plane or FSSs	8 mm	8 mm

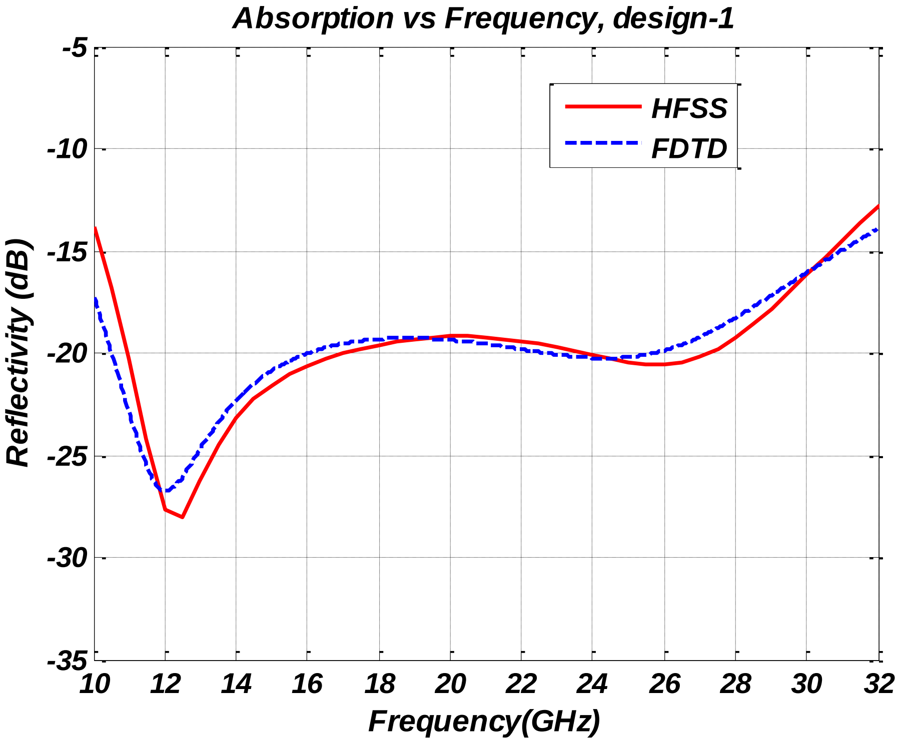

Figure 4-22 Reflectivity characteristics of the absorber labeled as *design-1*

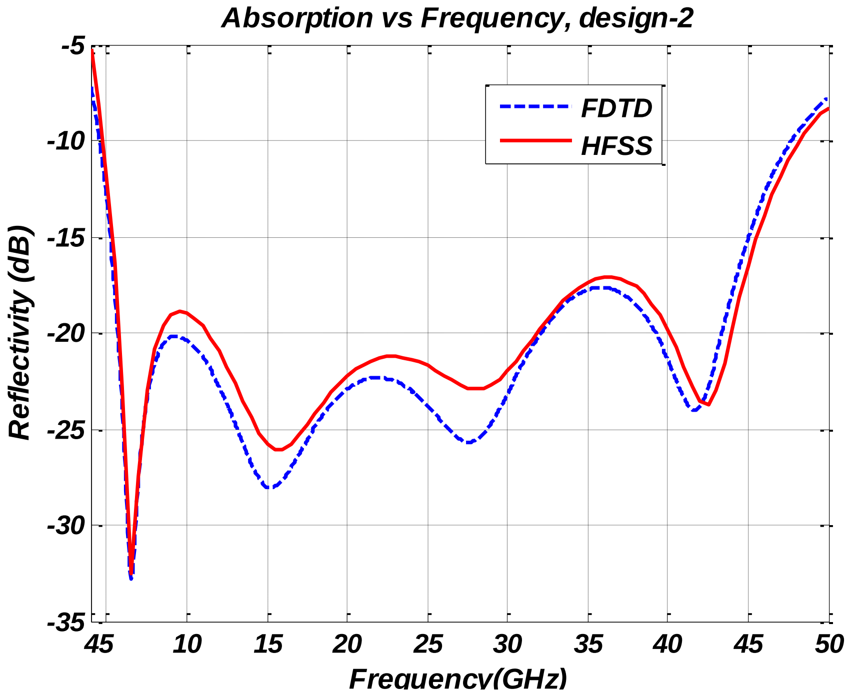

Figure 4-23 Reflectivity characteristics of the absorber labeled as *design-2*

As can be seen from the graphs, the results of the developed codes are very consistent with the solutions gathered from HFSS. Moreover, FDTD simulations are very efficient in terms of simulation time especially for wide-band structures. To illustrate the point, the simulation time of the absorber labeled as design-2 with HFSS is nearly ten minutes, while the corresponding duration for the case of FDTD analysis is less than two minutes.

4.3 Improvement of the absorber design method introduced in Chapter 3 with employment of FDTD codes to the approach

To carry the circuit analog absorber design method introduced in Chapter 3 to one step further, the developed FDTD codes are installed to the method. The main modification is that the developed codes are used instead of HFSS in the steps where full wave electromagnetic solutions are needed. Besides, a further optimization over the final design is carried out to compensate the mutual coupling effects between the lossy FSS layers which are the main reason for the deviation from the desired reflectivity characteristics as illustrated in Chapter 3. The rest of the approach is almost unchanged. The main steps of the new method are given in Figure 4-24.

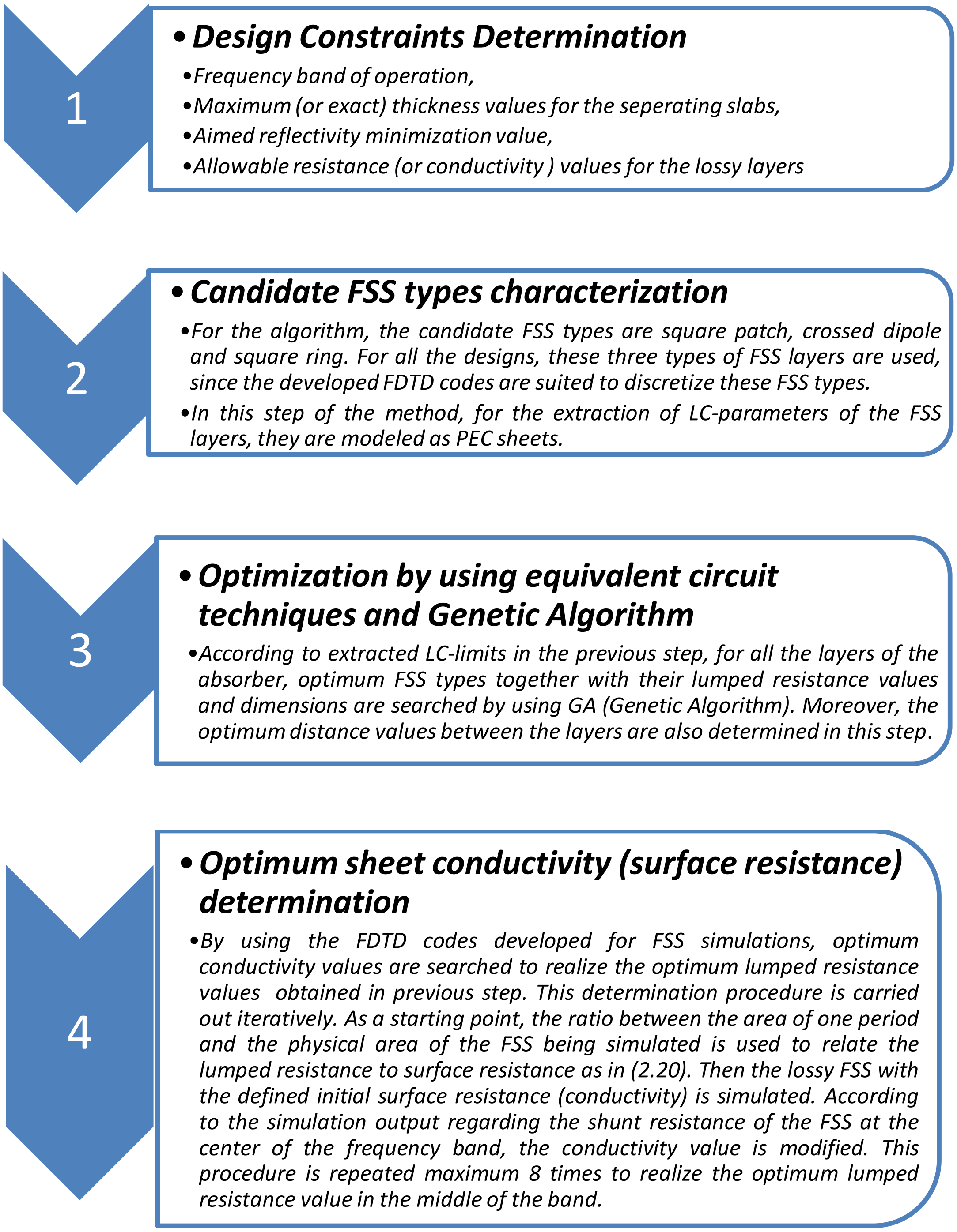

1

- ***Design Constraints Determination***
  - *Frequency band of operation,*
  - *Maximum (or exact) thickness values for the seperating slabs,*
  - *Aimed reflectivity minimization value,*
  - *Allowable resistance (or conductivity) values for the lossy layers*

2

- ***Candidate FSS types characterization***
  - *For the algorithm, the candidate FSS types are square patch, crossed dipole and square ring. For all the designs, these three types of FSS layers are used, since the developed FDTD codes are suited to discretize these FSS types.*
  - *In this step of the method, for the extraction of LC-parameters of the FSS layers, they are modeled as PEC sheets.*

3

- ***Optimization by using equivalent circuit techniques and Genetic Algorithm***
  - *According to extracted LC-limits in the previous step, for all the layers of the absorber, optimum FSS types together with their lumped resistance values and dimensions are searched by using GA (Genetic Algorithm). Moreover, the optimum distance values between the layers are also determined in this step.*

4

- ***Optimum sheet conductivity (surface resistance) determination***
  - *By using the FDTD codes developed for FSS simulations, optimum conductivity values are searched to realize the optimum lumped resistance values obtained in previous step. This determination procedure is carried out iteratively. As a starting point, the ratio between the area of one period and the physical area of the FSS being simulated is used to relate the lumped resistance to surface resistance as in (2.20). Then the lossy FSS with the defined initial surface resistance (conductivity) is simulated. According to the simulation output regarding the shunt resistance of the FSS at the center of the frequency band, the conductivity value is modified. This procedure is repeated maximum 8 times to realize the optimum lumped resistance value in the middle of the band.*

Figure 4-24 Flowchart of the improved method

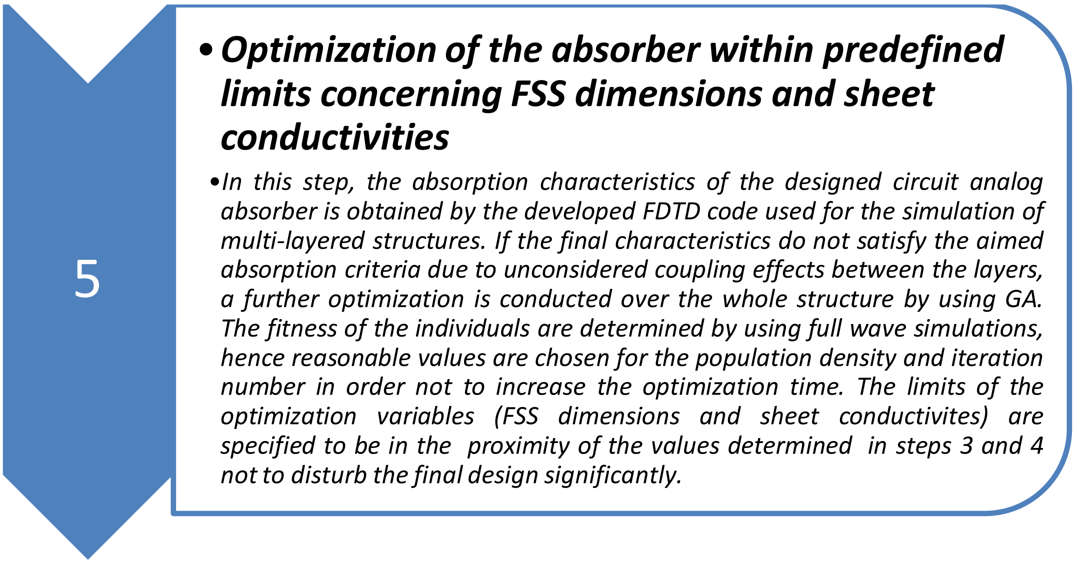

- ***Optimization of the absorber within predefined limits concerning FSS dimensions and sheet conductivities***
  - *In this step, the absorption characteristics of the designed circuit analog absorber is obtained by the developed FDTD code used for the simulation of multi-layered structures. If the final characteristics do not satisfy the aimed absorption criteria due to unconsidered coupling effects between the layers, a further optimization is conducted over the whole structure by using GA. The fitness of the individuals are determined by using full wave simulations, hence reasonable values are chosen for the population density and iteration number in order not to increase the optimization time. The limits of the optimization variables (FSS dimensions and sheet conductivites) are specified to be in the proximity of the values determined in steps 3 and 4 not to disturb the final design significantly.*

Figure 4-24 Flowchart of the improved method (continued)

To illustrate the validity and efficiency of the method, two circuit analog absorbers with different frequency bands of operation and comprising of candidate FSS types, namely square patch, crossed dipole and square ring are designed by using the improved method.

The first design example is a four-layered circuit analog absorber aimed to operate in the band 4-18 GHz. The aimed reflection minimization value is 20 dB through the whole frequency band. The HFSS model of the absorber is shown in Figure 4-25. The details of the structural parameters together with surface resistance values are shown in Table 4-2.

The reflectivity characteristics of the CA RAM in Figure 4-25 are given in Figure 4-26. The blue curve labeled as *'target',* denotes the desired reflectivity characteristics input to the design process. The red one represents the case of a synthetic absorber formed by bringing the four layers of the absorber mathematically. In other words, by using the shunt model impedance values of the designed layers and transmission line theory by taking the optimum distances between layers into account, a synthetic absorber is formed in MATLAB. Hence, in this model, the coupling effects are not taken into account. For the case of curve labeled as *'before final opt.'*, the coupling effects inherently exist, since it represents the full wave solution of the designed absorber. As can be seen, owing to coupling, the reflectivity characteristics deviate from the desired one in a negative manner. To compensate these effects, as stated in the explanation of the improved method, a further optimization over this structure is performed and the characteristic represented by light green curve is achieved.

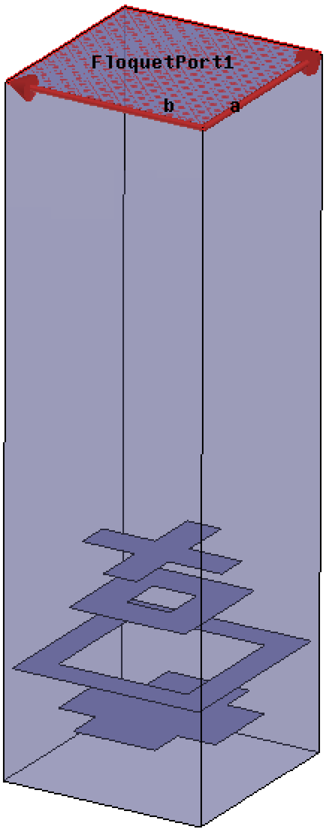

Table 4-3 Design parameters of the four-layered CA RAM designed by the improved method

FSS type	***edge width***	***edge length***	***surface impedance***
crossed dipole	*2.59 mm*	*10.71 mm*	*151.3 ohm/sq.*
thickness		*3.4 mm (air)*	
square ring	*2.79 mm*	*8.92 mm*	*89.8 ohm/sq.*
thickness		*4 mm (air)*	
square ring	*2.24 mm*	*14.4 mm*	*21.02 ohm/sq.*
thickness		*4 mm (air)*	
crossed dipole	*6.29 mm*	*12.09 mm*	*62.1 ohm/sq.*
thickness		*4 mm (air)*	
		Metal Plate	

(a) **(b)**

Figure 4-25 The first design example of the improved method: (a) HFSS model, (b) design parameters

This result shows the success of the final optimization step. To validate the accuracy of final characteristics, the structure is simulated also by HFSS and the results are added to the graph with the curve labeled as ‘HFSS’. It is worth to note that the results are well agreed with the solution obtained by the FEM method of HFSS.

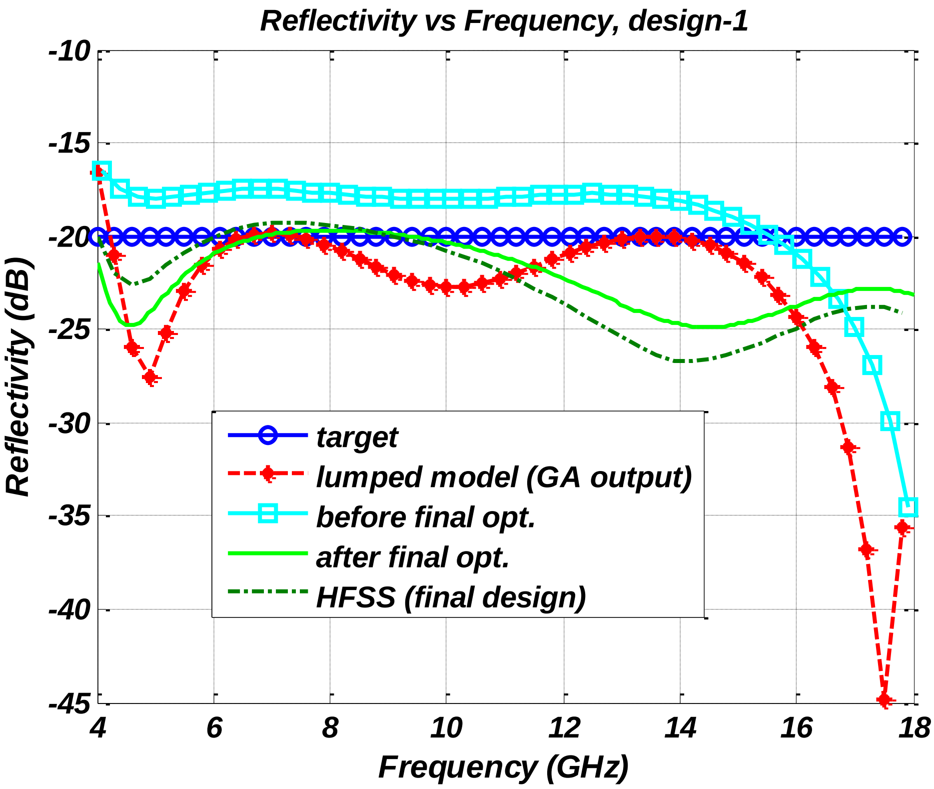

Figure 4-26 Reflectivity characteristics of the four-layered CA RAM example design by the improved method

To illustrate the efficiency of the developed codes and the method together with the validity of the results, a second circuit analog RAM with a wider operation band is designed. The second design example is a six-layered RAM aimed to operate in the band 2-26.5 GHz covering S, C, X, Ku and K bands. The aimed reflection minimization value is defined as 20 dB. The HFSS model of the absorber is shown in Figure 4-27. The details of the structural parameters together with surface resistance values are shown in Table 4-3.

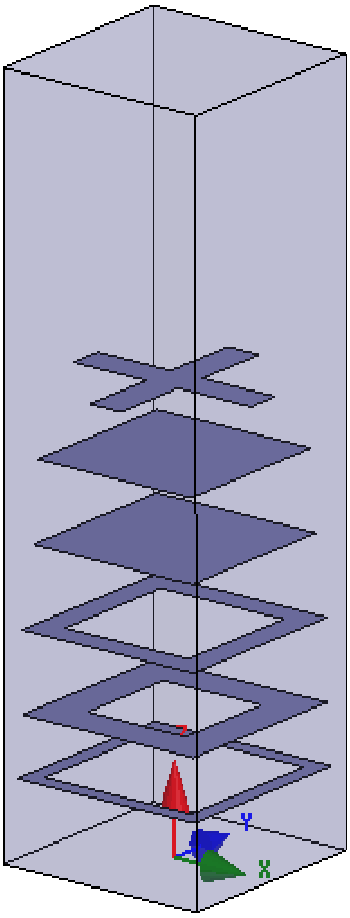

Table 4-4 Design parameters of the six-layered CA RAM designed by the improved method

FSS type	*edge width*	*edge length*	*surface impedance*
crossed dipole	*1.63 mm*	*9.2 mm*	*750.13 ohm/sq.*
thickness		*2.8 mm (air)*	
patch	*7.98 mm*	*7.98 mm*	*779.8 ohm/sq.*
thickness		*3.2 mm (air)*	
patch	*8.26 mm*	*8.26 mm*	*765.29 ohm/sq.*
thickness		*3.2 mm (air)*	
square ring	*1.26 mm*	*8.92 mm*	*177.92 ohm/sq.*
thickness		*3.2 mm (air)*	
square ring	*1.90 mm*	*8.89 mm*	*130.97 ohm/sq.*
thickness		*2.4 mm (air)*	
square ring	*0.81 mm*	*9.2 mm*	*43.6 ohm/sq.*
thickness		*3.2 mm (air)*	
		Metal Plate	

Figure 4-27 The second design example of the improved method: HFSS model, and design parameters

Mutual coupling between the layers of the second RAM example is not effective as much as in the case of first design, if the black and light green curves in Figure 4-28 are observed. The minor undesired effects due to unpredicted coupling for frequencies above 24 GHz are almost eliminated with the final optimization stage. Beside this point, the absorption characteristics are well agreed with the solution obtained by the FEM method of HFSS, which is shown by dark green curve.

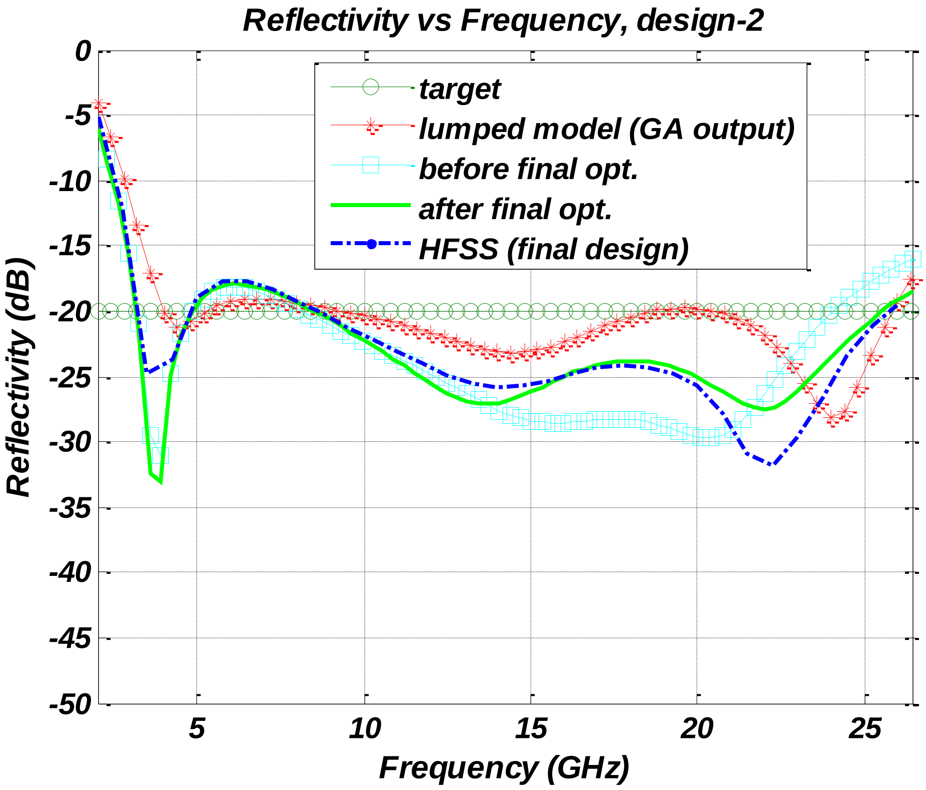

Figure 4-28 Reflectivity characteristics of the six-layered CA RAM example design by the improved method

CHAPTER 5

PRODUCTION OF CIRCUIT ANALOG RAM AND MEASUREMENTS

Up to now, developed topologies regarding CA RAM design process together with design examples with altering number of layers and different frequency bands are presented. To see the production capabilities and the consistency between the measurements and design outputs, a circuit analog RAM designed with the proposed method is manufactured. In this chapter, the production steps of the corresponding structure together with the measurement results are presented.

To realize lossy sheets with desired surface impedance values, it is decided to use tracing papers on which lossy layers are superimposed, as shown in Figure 5-1.

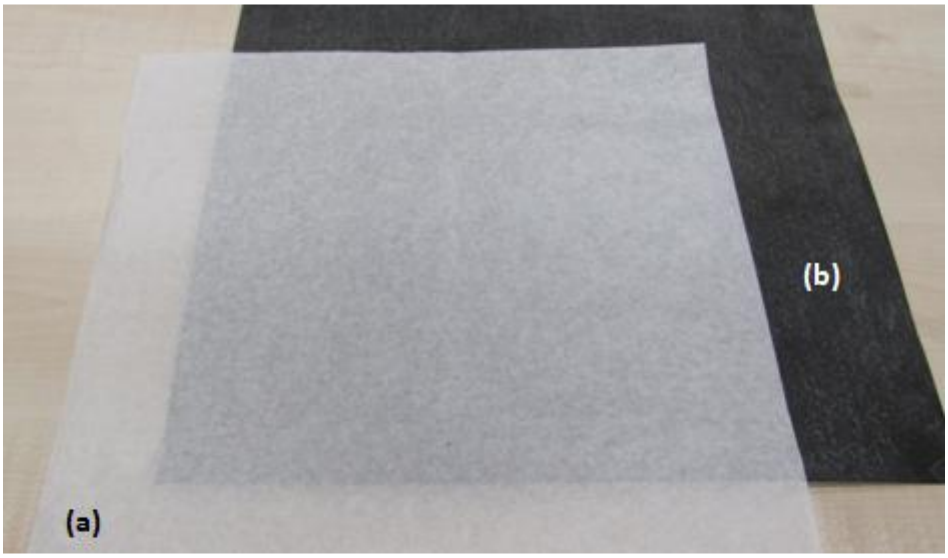

Figure 5-1 Tracing papers: (a) without absorbing layer, (b) with one pass absorbing layer superimposed on

Application of absorbing layer on tracing papers is realized by using the facilities of ASELSAN Inc. Since dielectric filler material is conductive, as the filler density on the absorbing layer increases, the conductivity of the sheet increases resulting in a decreasing surface resistance value. To obtain lower surface resistance, filler content deposited in the absorbing layer mixture is increased in discrete values. This process results in discrete surface resistance values for the lossy sheets. Hence, a continuous surface resistance spectrum cannot be achieved by this method. Therefore, the obtained discrete resistance values should be input to the design of the circuit analog RAM to be manufactured.

Before the design of the structure, to collect these discrete surface resistance values, seven tracing papers are impregnated with absorbing layers that has different filler content. The reason why this process is conducted with seven papers is to see the repeatability of the lossy layer impregnation process. Each step is applied to all seven sheets, and consistency between the sheet resistances is investigated. To extract the resistance values corresponding to these discrete number of layer impregnations, the lossy sheets are characterized in the Free Space Microwave Measurement System setup of Antenna Technologies Department of ASELSAN Inc. The setup for lossy sheet characterization is shown in Figure 5-2.

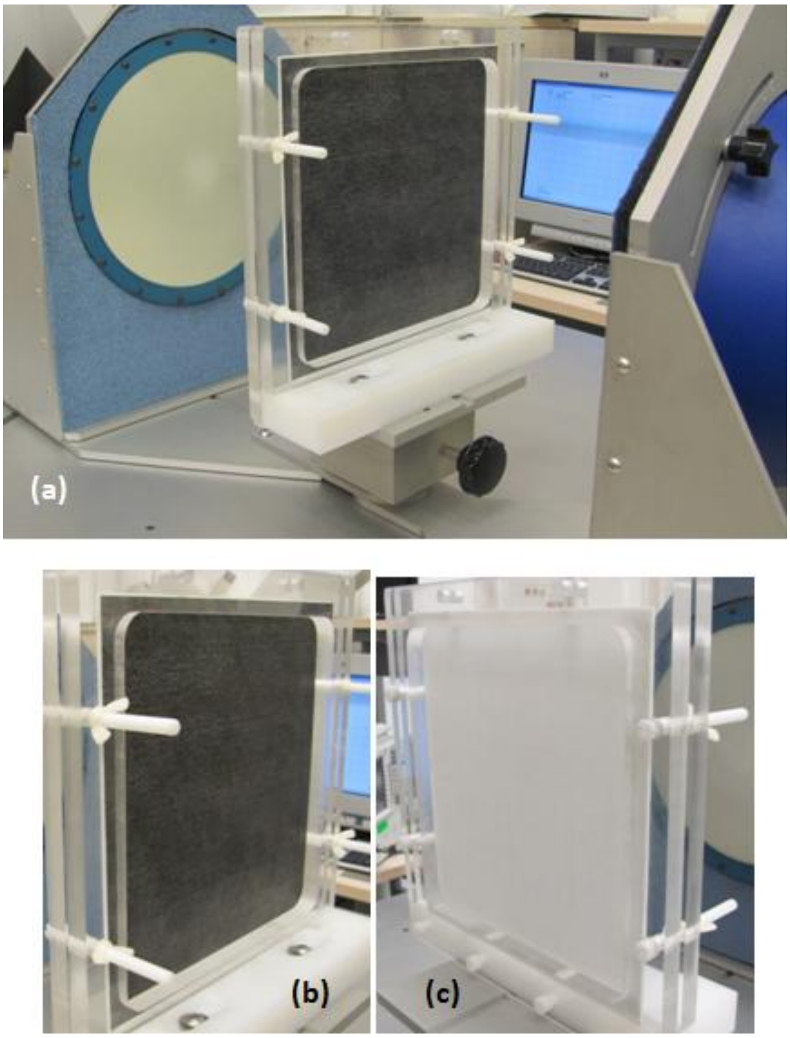

Figure 5-2 Characterization of the lossy tracing papers: (a) HVS Free Space Microwave Measurement System, (b) front view of lossy sheet, (c) back view of lossy sheet

The measured surface resistance values of the seven tracing papers are shown in Figure 5-3 to Figure 5-7 in an increasing content of filler material in the lossy sheet.

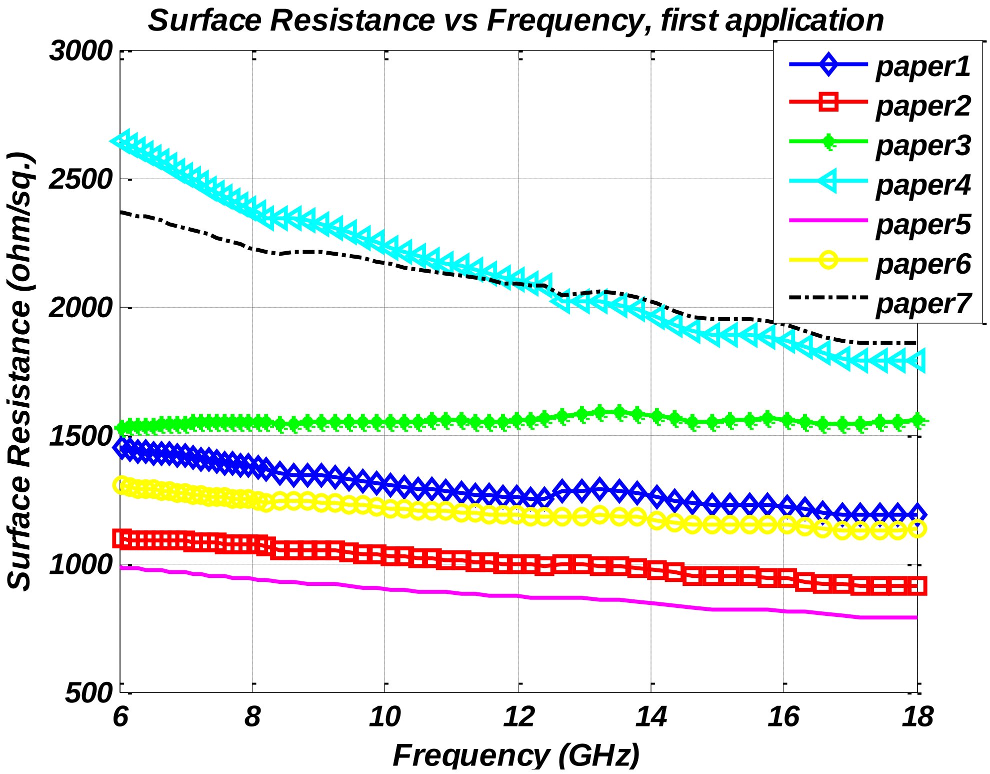

Figure 5-3 Surface resistance values of the sheets after first application

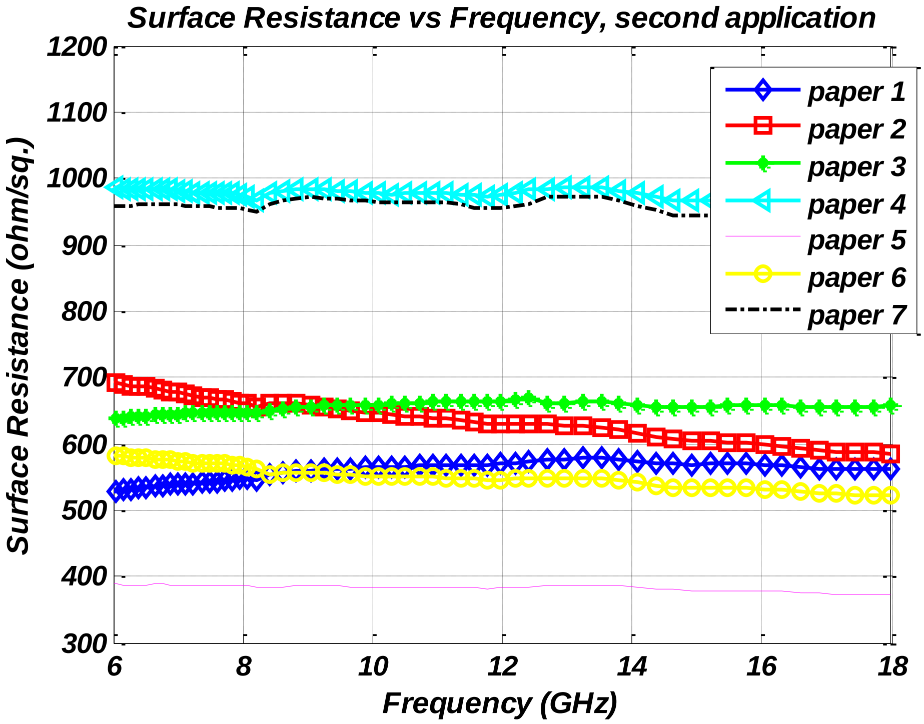

Figure 5-4 Surface resistance values of the sheets after second application

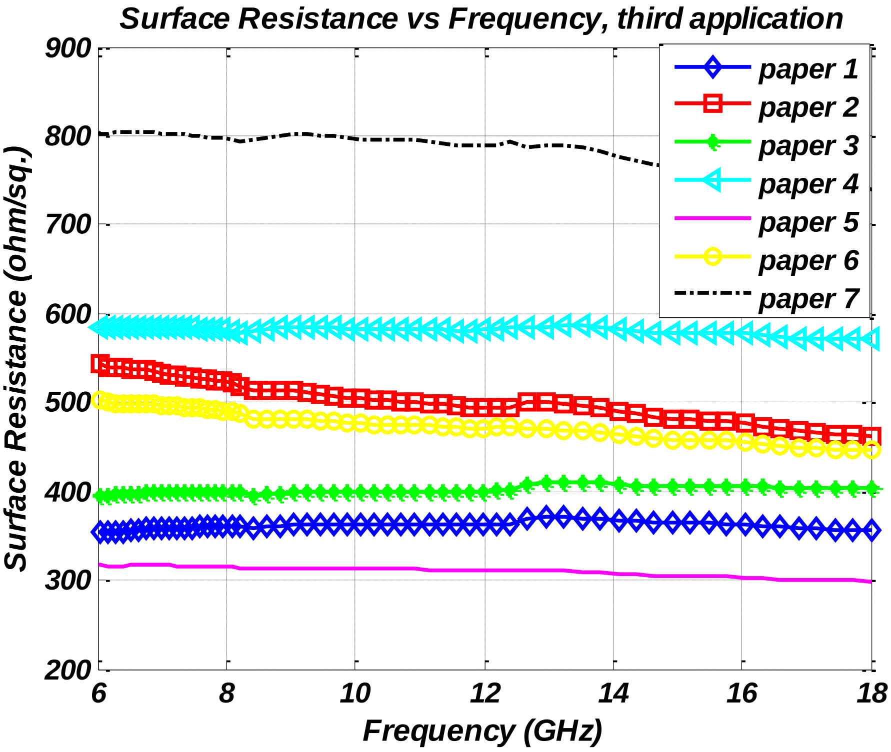

Figure 5-5 Surface resistance values of the sheets after third application

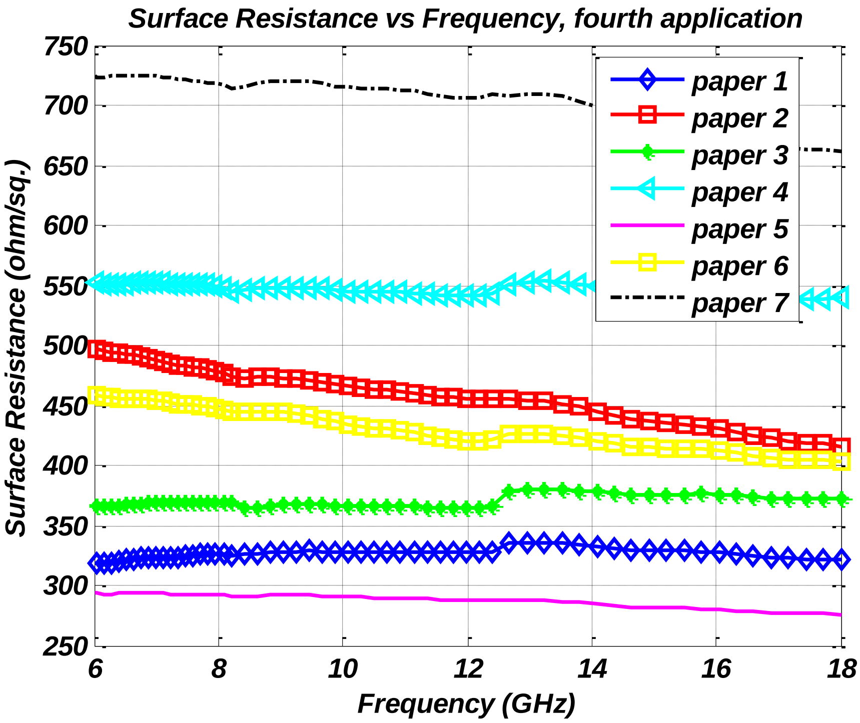

Figure 5-6 Surface resistance values of the sheets after fourth application

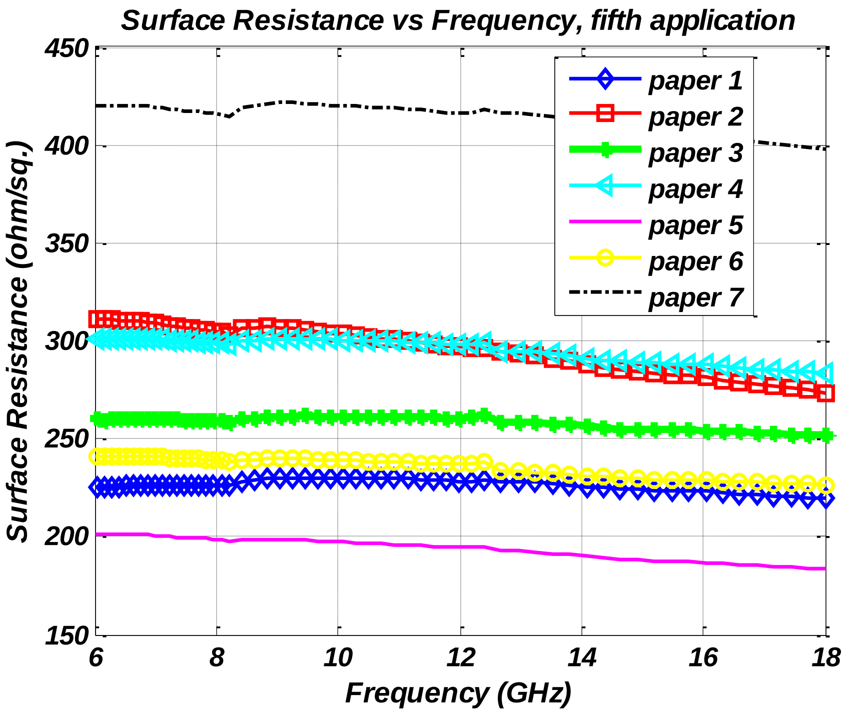

Figure 5-7 Surface resistance values of the sheets after fifth application

As can be seen from the Figures, the resistance values of the sheets on which the same amount of filler content is applied are not sufficiently consistent. The main reason of this inconsistency is owing to man-made nature of the lossy layer impregnation process. By taking into these deviations, reasonable discrete surface resistance values obtained by averaging the measured ones are defined to be used in the design process and they are shown in Table 5-1.

Table 5-1 Attainable surface resistance values with specified application configurations

Lossy layer impregnation configuration	***Surface Resistance (ohm/sq.)***
First application	*1500 ohm/sq.*
Second application	*660 ohm/sq.*
Third application	*400 ohm/sq.*
Fourth application	*340 ohm/sq.*
Fifth application	*260 ohm/sq.*

The developed circuit analog RAM design code explained in Chapter 4 is modified in a way that candidate layer conductivity (surface resistance) values are limited to the ones given in Table 5-1 rather than a continuous spectrum specified by lower and upper limits. Moreover, the separating slab characteristics of the optimization process are limited to a set consisting of air line with a thickness of 0.2 mm and Rohacell 71 HF ([55]) with a thickness of 3.5 mm. The corresponding air line with a thickness of 0.2 mm will be realized with a fabric posing electrical characteristics of free space. With these modifications, a five layered circuit analog RAM aimed to operate in the band 4-14 GHz with an aimed reflectivity of -20 dB is designed and validated with HFSS. The HFSS model of the absorber together with structural parameters is given in Figure 5-8 and Table 5-2, respectively.

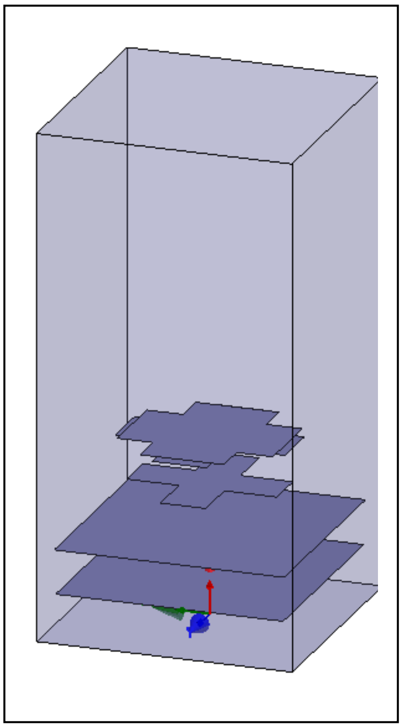

Table 5-2 Design parameters of the five-layered CA RAM to be manufactured

FSS type	***edge width***	***edge length***	***surface impedance***
crossed dipole	*6.54 mm*	*12.2 mm*	*660 ohm/sq.*
thickness		*0.2 mm (air)*	
crossed dipole	*4.3 mm*	*13.3 mm*	*260 ohm/sq.*
thickness		*3.5 mm (air)*	
crossed dipole	*3.55 mm*	*11.77 mm*	*400 ohm/sq.*
thickness		*3.5 mm (air)*	
patch	*18 mm*	*18 mm*	*260 ohm/sq.*
thickness		*3.5 mm (air)*	
patch	*17.82 mm*	*17.82 mm*	*260 ohm/sq.*
thickness		*3.5 mm (air)*	
		Metal Plate	

Figure 5-8 Five layered CA RAM to be manufactured: HFSS model, and design parameters

The reflectivity characteristics of the designed absorber are shown below, in Figure 5-9.

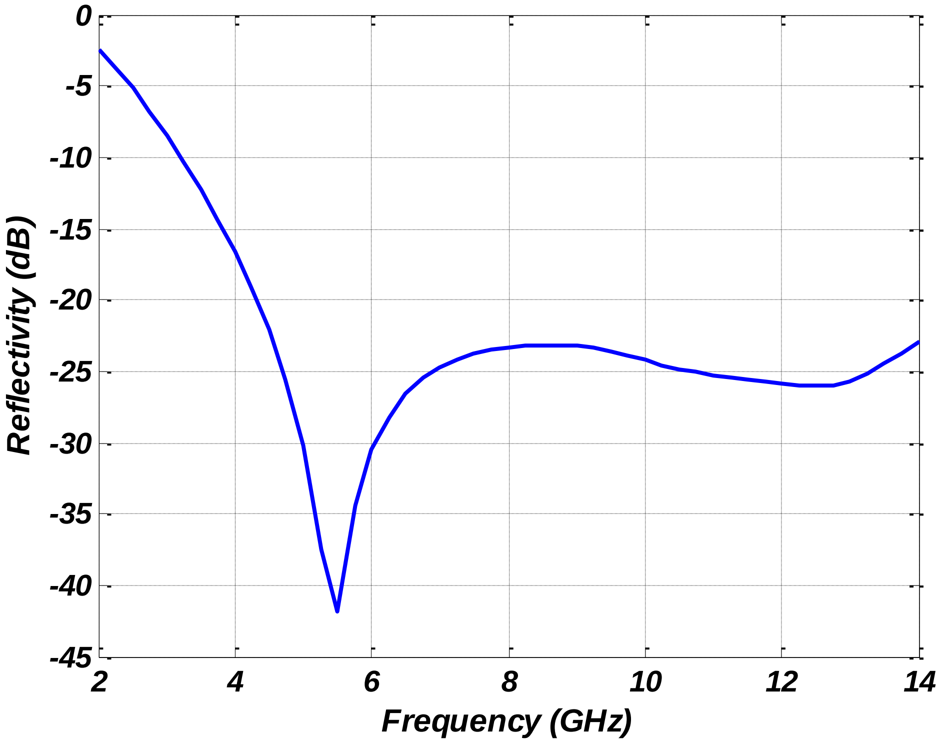

Figure 5-9 Reflectivity characteristics of the five-layered RAM

The next step is the production of the lossy sheets on which desired patterns of defined FSS shapes are superimposed. To realize this step, masks regarding FSS shapes to be realized are manufactured. For illustration purposes, manufactured mask for the fifth layer is shown in Figure 5-10.

According to optimum surface resistance values and Table 5-1 which shows the relationship between the attainable surface resistance values according to altering filler content of lossy layers, the application configuration that should be applied to corresponding sheets are determined and given in Table 5-3.

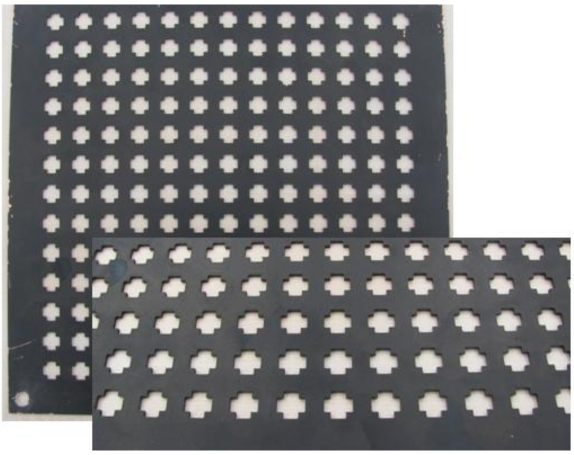

Figure 5-10 Mask of layer 5

Table 5-3 Necessary lossy layer impregnation configurations for all five sheets

Sheet ID number	***Number of applications***
1	*Five applications*
2	*Five applications*
3	*Three applications*
4	*Five applications*
5	*Two applications*

According to application configuration given in Table 5-3, the tracing papers are impregnated with lossy layers by using the manufactured masks for the initial iteration. Optimum impregnation process for each sheet has changed with characterization results of the patterned lossy sheets, since desired sheet characteristics could no t be realized with the configurations given in Table 5-3.

After application of lossy layers with sufficient iterations, the resultant insertion loss values of the patterned tracing papers are shown in Figure 5-12 to Figure 5-16. Note that the measurements are carried out only in the X-band.

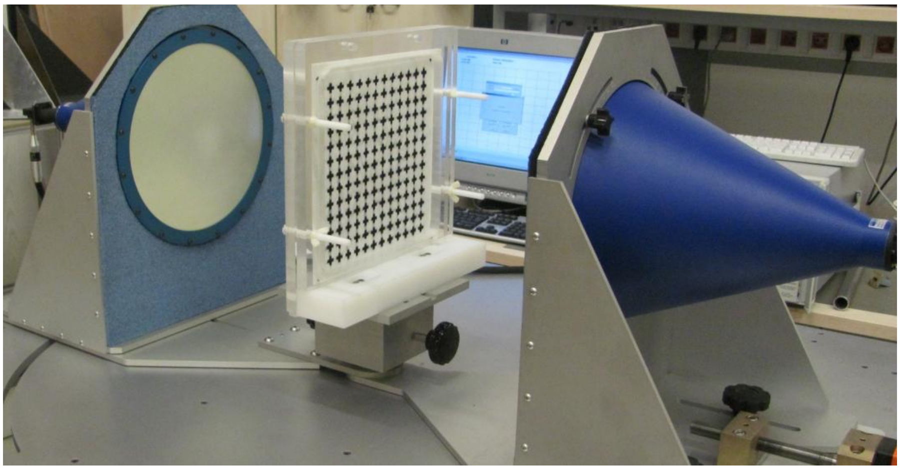

Figure 5-11 Measurement of layer 4 in free space microwave measurement system

The comparison of impregnated tracing paper measurements with desired HFSS characteristics are realized over insertion loss parameters. Unless distortions regarding pattern details occur, the discrepancy between the measurement and desired characteristics can be attributed to unrealized optimum surface resistance.

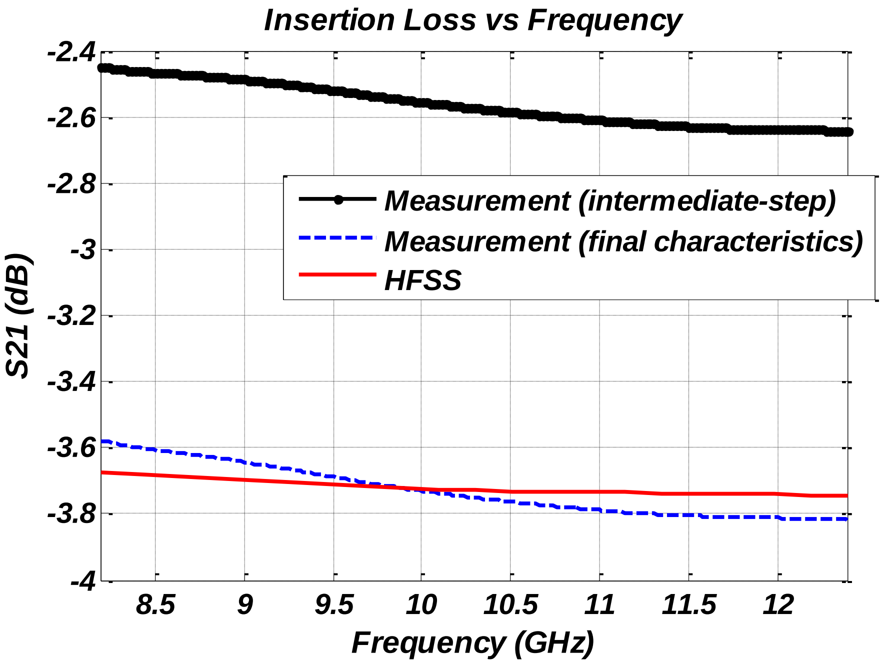

Figure 5-12 Measured insertion loss of sheet 1 after desired characteristics are reached

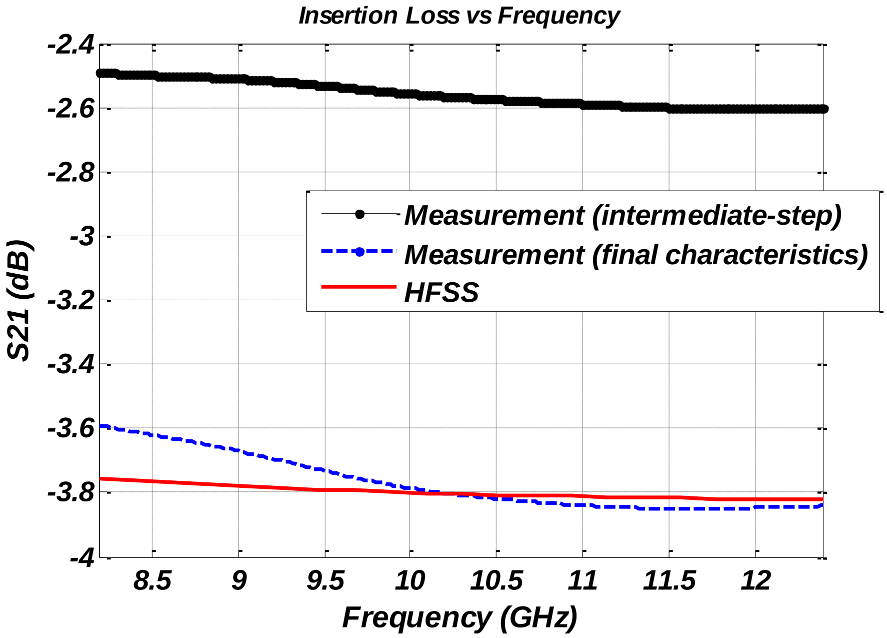

Figure 5-13 Measured insertion loss of sheet 2 after desired characteristics are reached

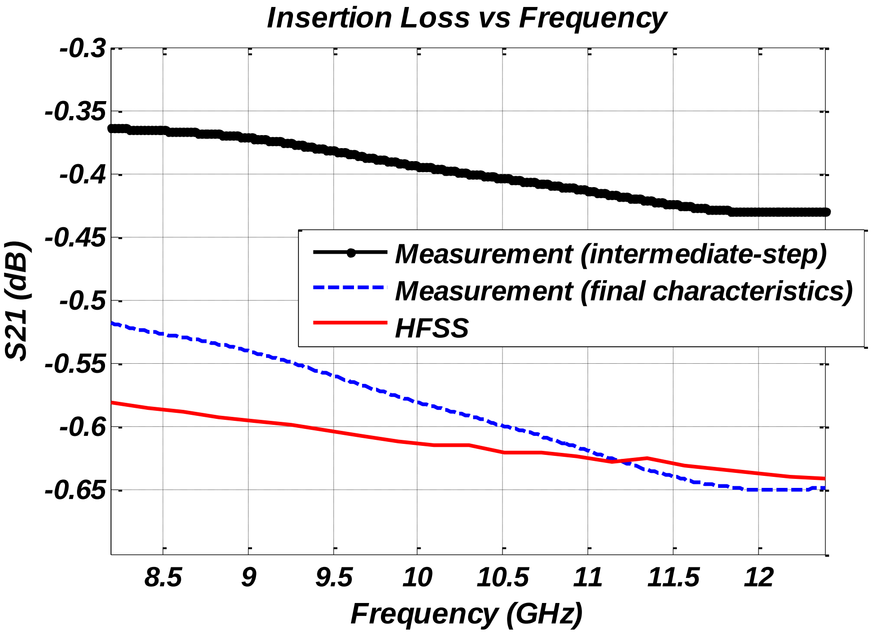

Figure 5-14 Measured insertion loss of sheet 3 after desired characteristics are reached

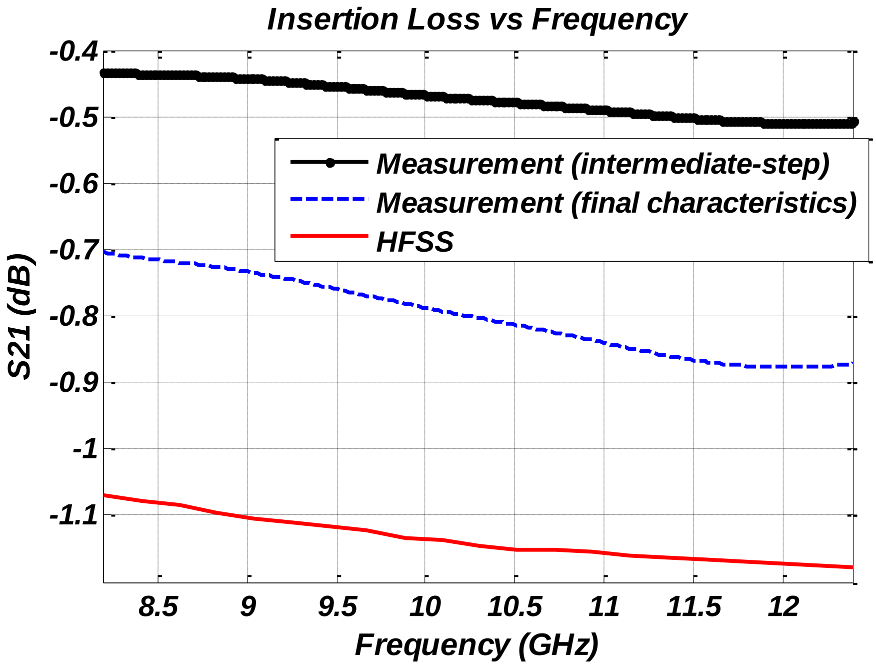

Figure 5-15 Measured insertion loss of sheet 4 after desired characteristics are reached

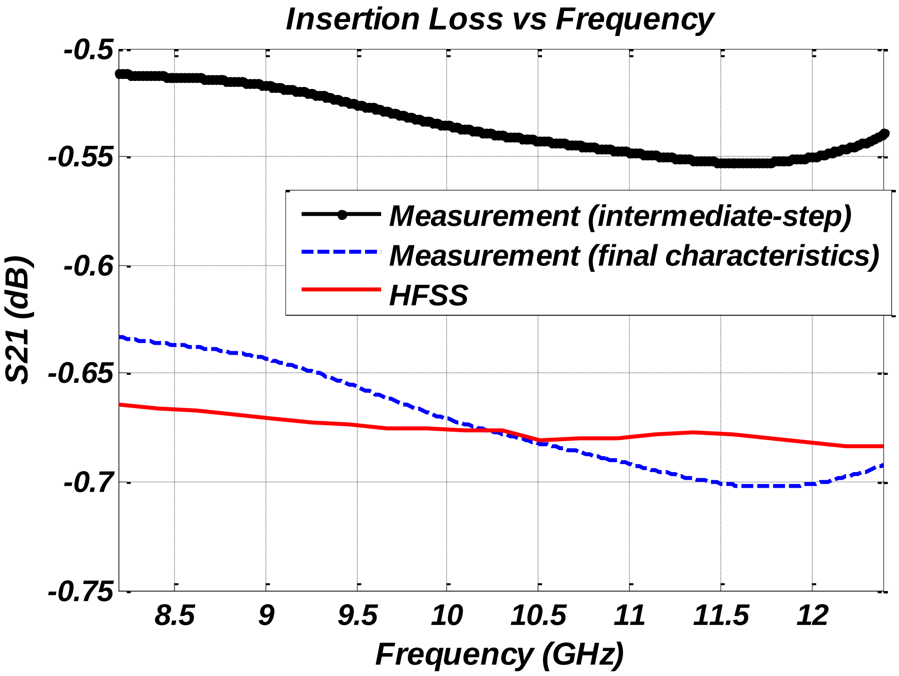

Figure 5-16 Measured insertion loss of sheet 5 after desired characteristics are reached

The patterned lossy sheets after final applications are also shown in Figure 5-17.

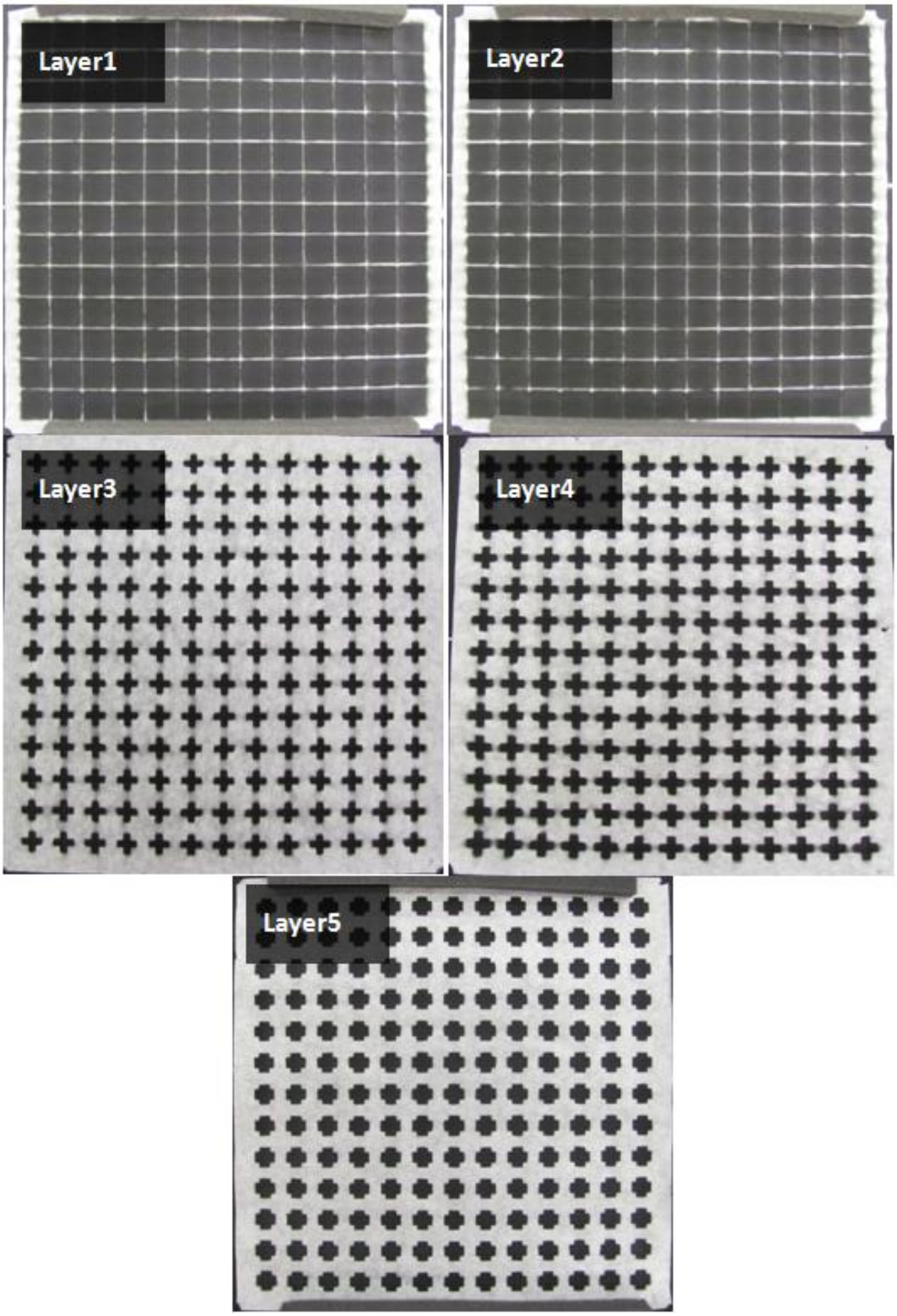

Figure 5-17 Manufactured patterned lossy sheets

As can be seen from the insertion loss graphics regarding measurement and desired (HFSS) results, for the first three and the fifth layers, desired insertion loss values are almost realized in the center of the band. The insertion loss characteristics of the sheets deviate from the desired ones throughout the frequency band of measurement such that there is not a simple offset with the two characteristics. This phenomenon is obvious, especially for the case of crossed dipoles of sheets 3 and 5, given in Figure 5-14 and Figure 5-16. This phenomenon can be devoted to following main reasons:

- Filling of the spacings between adjacent FSS cells and distortions near the edges of FSS elements due to leakage of lossy layer beneath the mask as the number of impregnation increases, as illustrated in Figure 5-18,
- Accumulation of lossy layer particles on the edges of FSS elements with an increase in the thickness of the corresponding regions resulting in lower surface resistance values (eqn. 2.14), as illustrated in Figure 5-19,
- Due to tightening of the mask details owing to lossy layer accumulation on the inner edges of the mask, formation of surface resistance taper from the edges to the center of FSS elements occurs, as illustrated in Figure 5-20.

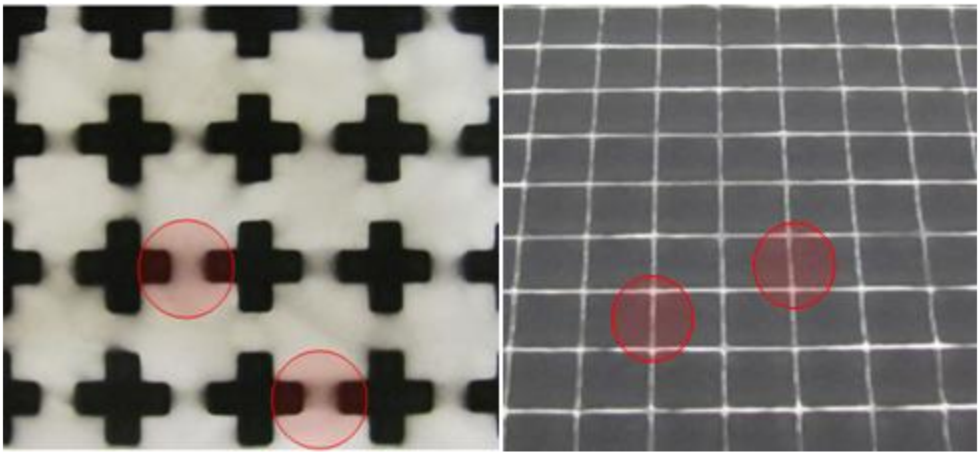

Figure 5-18 Filling of the spacings and distortions near edges as number of iterative applications increases

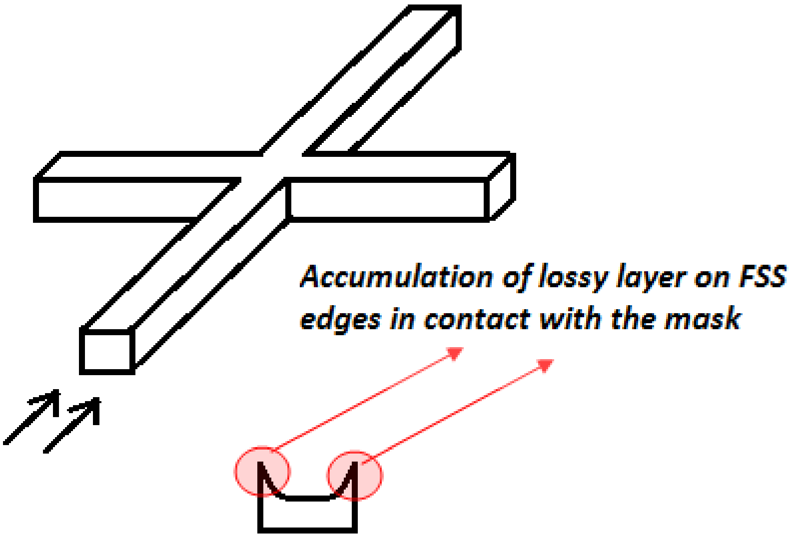

Figure 5-19 Illustration of lossy layer accumulation on FSS edges

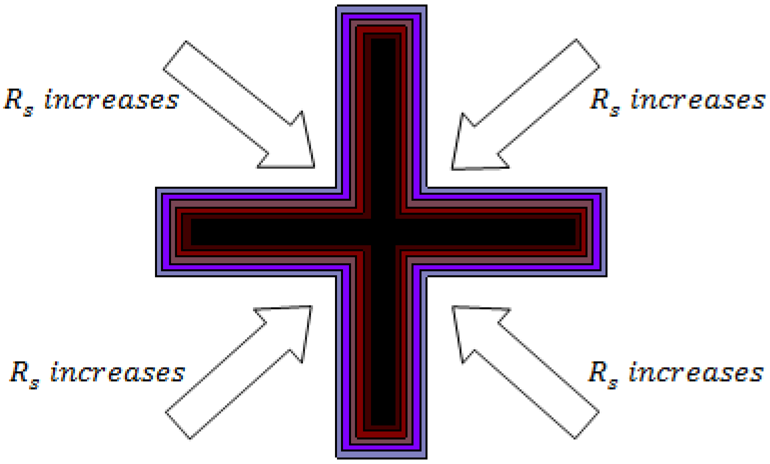

Figure 5-20 Surface resistance taper due to eventual decrease in application area of mask due to residual build up of lossy layer on the mask

Due to all reasons stated above, the impregnation process for the fourth layer is stopped without any further impregnation. The metal backed absorber is formed by bringing all the layers together as shown in Figure 5-21.

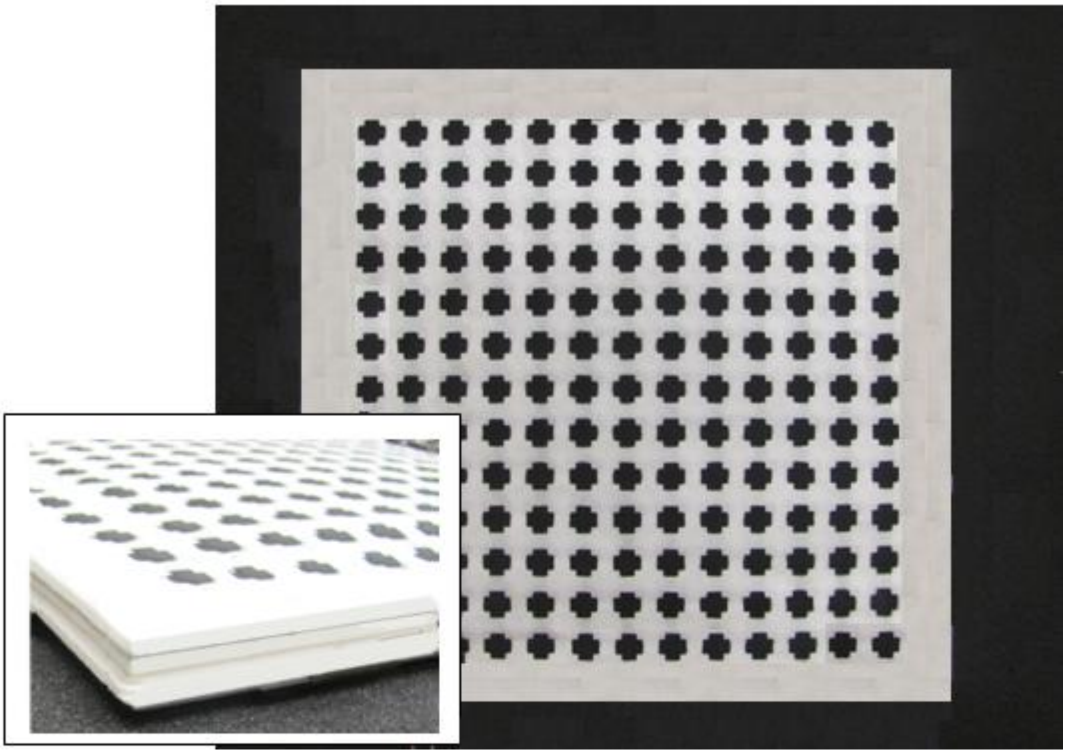

Figure 5-21 Manufactured five layered Circuit Analog RAM

The resultant circuit analog RAM with overall thickness of 14.2 mm is measured with the configuration shown in Figure 5-34. The absorber is illuminated with a horn antenna whose operational frequency band is 2 to 18 GHz. PNA series microwave network analyzer of Agilent Technologies is used for scattering measurements, [57]. The reflected signal from the structure is gated in time domain to exclude other reflections such as the ones originating from cable joints, aperture of the horn, multiple reflections in the configuration, [58]. For the reference signal, reflection from metal plate is measured, and a time domain window around the main reflection from the plate with a suitable gate width is constructed. Both signals, reference signal and the one reflected from the RAM, are transformed back to frequency domain, and the reflectivity characteristics of the RAM are obtained by referencing the metal plate reflection. The measured reflectivity characteristics of the structure together with the expected characteristics (HFSS) are shown in Figure 5-23.

Figure 5-22 Reflectivity measurement setup

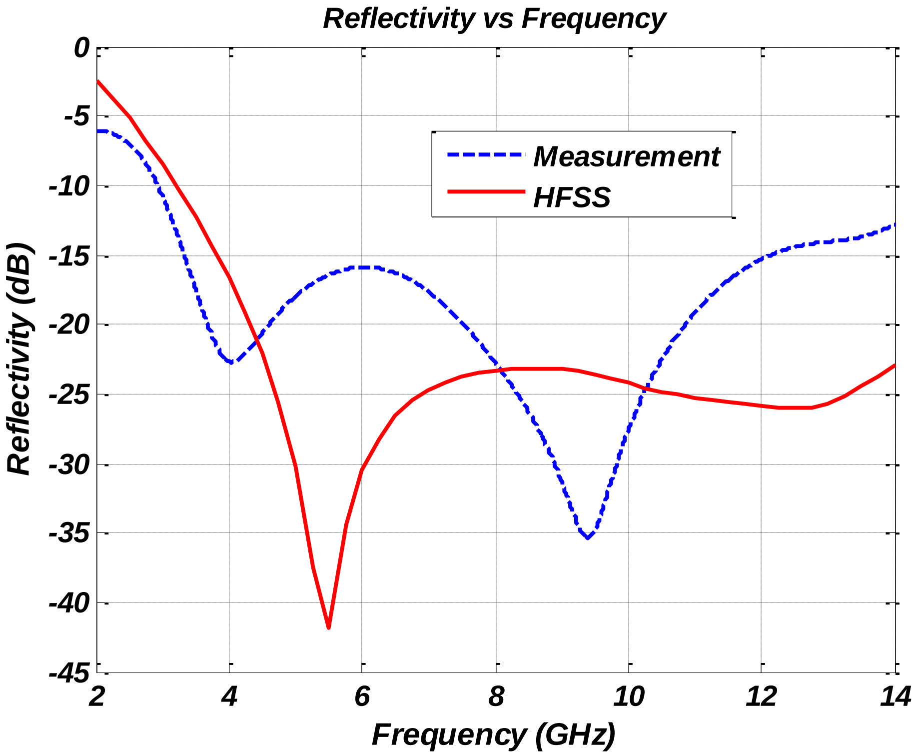

Figure 5-23 Reflectivity characteristics of the manufactured CA RAM

As can be seen from Figure 5-23, although the measured reflection minimization value is almost higher than 15 dB for the target frequency range, the results are not so consistent with the design expectations. The main reasons for this discrepancy are stated under three headings in the previous parts.

CHAPTER 6

CONCLUSIONS

A fast and efficient method for the design of multi-layered circuit analog radar absorbing structures comprising conducting layers with arbitrary geometrical patterns is introduced. The developed method gives the designer freedom for the choices of number of layers, FSS types, layer separator slab characteristics together with their thickness values. The developed method is, basically, optimization of specular reflection coefficient of a multi-layered circuit analog absorbing structure comprising of lossy FSS layers by using Genetic Algorithm and circuit equivalent models of FSS layers. After allowable LC values for candidate FSS types are gathered by altering the physical dimensions of FSS patterns, optimum FSS types and dimensions together with optimum lumped resistance values are searched by using Genetic Algorithm. The reason why Genetic Algorithm is preferred is the efficiency and speed of the method, especially for optimization problems with low number of unknowns. To realize the optimized lumped resistances, optimum surface resistance values for all FSS layers are determined iteratively with a reasonable starting point. With the proposed approach, two example circuit analog RAMs are designed and reflection characteristics are validated with HFSS by using unit cell simulations. One of the designed absorbers, which is a two-layered structure, covers the frequency band of 10-31 GHz with -15 dB reflectivity for normal incidence and a total thickness of 6.6 mm. The total thickness of the second design example is 8.77 mm and it is capable of 15 dB reflectivity minimization in the frequency band of 6 to 46 GHz. It comprises of four lossy FSS layers. To the author’s knowledge, both absorbers are superior in terms of frequency band/thickness to the ones with similar topology (multi-layered circuit analog RAMs) existing in the literature.

The proposed design approach is improved with embedding of in house developed FDTD codes for the characterization of lossy or lossless frequency selective surfaces and absorption analysis of multi-layered circuit analog absorbers. The verifications of the developed codes are realized by comparing the reflection and/or transmission characteristics of sample structures with the results obtained by HFSS. It is seen that, a high degree of consistency is achieved for FDTD solutions of these periodic structures. By embedding of these codes to the design method, a compact tool for the design of circuit analog RAMs with any number of layers, any thickness values and any frequency band of operation is realized. Moreover, capability of compensating the unpredicted coupling effects of adjacent layers is gained with the final optimization stage of the improved method. To show the capabilities of the improved method, two more circuit analog RAMs are designed with the developed codes. One of the designed absorbers covers the frequency band of 4-18 GHz with a reflectivity value of -20 dB, which is a high value for reflection minimization when compared to the absorbing structures existing in the literature. The second design example operates in the frequency band of 3-26.5 GHz with 15 dB reflection minimization for normal incidence case.

To see the production capabilities and the consistency between the measurements and design outputs, a circuit analog RAM designed with the proposed method is manufactured. The developed code for the design of multi-layered absorbers is modified in terms of allowable layer resistance values for production with technical capabilities in hand. By using absorbing layers comprising of dielectric filler particles, the lossy sheets of the five-layered absorber are manufactured from tracing papers and stacked together to constitute the absorbing structure. The measurement of the absorber is realized by illuminating the structure with a horn antenna and measuring the reflected signal by using time domain gating method to discriminate the main reflection of interest. Although a high degree of consistency is not observed with simulations, 15 dB of reflection minimization is achieved from 3.5 GHz to 12 GHz with an overall thickness of 14.2 mm, which is the widest bandwidth among the manufactured circuit analog absorbers in the literature, to the author’s knowledge.

For future plans, it is decided to improve the proposed approach for design of absorbers with desired absorption characteristics under oblique incidence cases, especially for developed FDTD codes. Also to enhance the degree of freedom for absorber design, the developed FDTD codes will be adapted to more types of frequency selective surfaces. Moreover, to validate the efficiency of the introduced methodology it is planned to design and manufacture absorbers with altering number of layers in different frequency bands.

APPENDIX A

MODIFICATIONS FOR THE DEVELOPED METHOD FOR THE DESIGN OF CIRCUIT ANALOG RAMs UNDER OBLIQUE INCIDENCES

The main consideration of the studies conducted in the thesis work is normal incidence case for the design of circuit analog absorbers. Therefore, the developed method which is introduced in Chapter 3 focuses on the normal incidence case. Although not performed, by modifying the steps of the introduced approach, it is possible to adapt the methodology to design an absorber which performs desired absorption characteristics under oblique incidence cases. The necessary modifications can be collected in the following headlines:

- Modification of the FSS layers' lumped models,
- Modifications of the electrical characteristics of separating slabs to be used for impedance transformation,
- Modification of the fitness evaluation of the individuals in Genetic Algorithm optimization step.

Modification of the FSS layers' lumped models

The LC parameters of FSS layers extracted as explained in Chapter 2 should be modified to be used under oblique incidence cases according to angle of arrival of the plane wave. For that purpose, averaging theory derived by M. I. Kontorovich can be used, [56]. In [29], Luukkonen and et al. have used the corresponding theory to derive analytical models for metal strips and square patches. According to their derivations, the necessary modifications are (shaded in gray):

for metal strips:

$$Z^{TM} = Z^{TM'}\left(1-\frac{k_0^2}{k_{eff}^2}\frac{sin^2\Theta}{2}\right) \qquad (A.1)$$

for square patches:

$$Z^{TE} = Z^{TE\prime}\frac{1}{\left(1-\frac{k_0^2}{k_{eff}^2}\frac{sin^2\Theta}{2}\right)} \qquad (A.2)$$

where, k_{eff} is the wave number of the incident wave vector in the effective host medium. For other types of FSS shapes, similar studies can be conducted to derive the necessary impedance multiplier term regarding angle of arrival.

<u>Modifications of the transmission line characteristics of separating slabs to be used for impedance transformation</u>

For multi-layered structures, to determine the input impedance (also reflection coefficient), as explained in Chapter 2, impedance transformations are used. Such a transformation is shown in Figure A-1 and eqn. A.2.

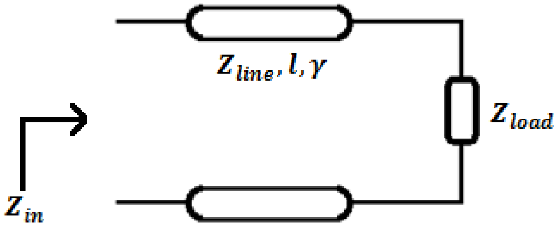

Figure A-1 Transmission line model of a shunt connected impedance

$$Z_{in} = Z_{line}\frac{(Z_{load} + Z_{line}\tanh\gamma_z l)}{(Z_{line} + Z_{load}\tanh\gamma_z l)} \qquad (A.2)$$

where

$$Z_{line} = \frac{\eta}{cos\theta}\ , \qquad for\ TM, parallel\ polarization$$

$$Z_{line} = \eta cos\theta\ , \qquad for\ TM, parallel\ polarization$$

$\gamma_z = \gamma cos\theta$

$\theta : angle\ of\ incidence$

Modification of the fitness evaluation of the individuals in Genetic Algorithm optimization step

For the case of absorber design with desired reflectivity characteristics over a specified range of angle of incidence, the fitness evaluation should be performed for every angle of interest during Genetic Algorithm optimization process. The reflection coefficient of an individual should be calculated by using the previously mentioned modifications for every incidence angle of interest. The fitness of the individual is then determined with respect to weighted mean (defined by the designer) of these reflection coefficient characteristics.

APPENDIX B

EXPLICIT FINITE DIFFERENCE APPROXIMATIONS OF MAXWELL'S CURL EQUATIONS

$$
\begin{aligned}
H^{n+\frac{1}{2}}_{x,i,j-\frac{1}{2},k-\frac{1}{2}} &= H^{n-\frac{1}{2}}_{x,i,j-\frac{1}{2},k-\frac{1}{2}} \\
&\quad - \frac{\Delta t}{\mu_{i,j-\frac{1}{2},k-\frac{1}{2}}}\left[\frac{E^{n}_{z,i,j,k-\frac{1}{2}} - E^{n}_{z,i,j-1,k-\frac{1}{2}}}{\Delta y} - \frac{E^{n}_{y,i,j-\frac{1}{2},k} - E^{n}_{y,i,j-\frac{1}{2},k-1}}{\Delta z}\right] \qquad (B.1)
\end{aligned}
$$

$$
\begin{aligned}
H^{n+\frac{1}{2}}_{y,i-\frac{1}{2},j,k-\frac{1}{2}} &= H^{n-\frac{1}{2}}_{y,i-\frac{1}{2},j,k-\frac{1}{2}} \\
&\quad - \frac{\Delta t}{\mu_{i-\frac{1}{2},j,k-\frac{1}{2}}}\left[\frac{E^{n}_{x,i-\frac{1}{2},j,k} - E^{n}_{x,i-\frac{1}{2},j,k-1}}{\Delta z} - \frac{E^{n}_{z,i,j,k-\frac{1}{2}} - E^{n}_{z,i-1,j,k-\frac{1}{2}}}{\Delta x}\right] \qquad (B.2)
\end{aligned}
$$

$$
\begin{aligned}
H^{n+\frac{1}{2}}_{z,i-\frac{1}{2},j-\frac{1}{2},k} &= H^{n-\frac{1}{2}}_{z,i-\frac{1}{2},j-\frac{1}{2},k} \\
&\quad - \frac{\Delta t}{\mu_{i-\frac{1}{2},j-\frac{1}{2},k}}\left[\frac{E^{n}_{y,i,j-\frac{1}{2},k} - E^{n}_{y,i-1,j-\frac{1}{2},k}}{\Delta x} - \frac{E^{n}_{x,i-\frac{1}{2},j,k} - E^{n}_{x,i-\frac{1}{2},j-1,k}}{\Delta y}\right] \qquad (B.3)
\end{aligned}
$$

$$
\begin{aligned}
E^{n+1}_{x,i-\frac{1}{2},j,k} &= \left[\frac{1 - \frac{\sigma_{i-\frac{1}{2},j,k}\Delta t}{2\epsilon_{i-\frac{1}{2},j,k}}}{1 + \frac{\sigma_{i-\frac{1}{2},j,k}\Delta t}{2\epsilon_{i-\frac{1}{2},j,k}}}\right] E^{n}_{x,i-\frac{1}{2},j,k} + \left[\frac{\frac{\Delta t}{\epsilon_{i-\frac{1}{2},j,k}}}{1 + \frac{\sigma_{i-\frac{1}{2},j,k}\Delta t}{2\epsilon_{i-\frac{1}{2},j,k}}}\right]\left[\frac{H^{n+\frac{1}{2}}_{z,i-\frac{1}{2},j+\frac{1}{2},k} - H^{n+\frac{1}{2}}_{z,i-\frac{1}{2},j-\frac{1}{2},k}}{\Delta y}\right. \\
&\quad \left. - \frac{H^{n+\frac{1}{2}}_{y,i-\frac{1}{2},j,k+\frac{1}{2}} - H^{n+\frac{1}{2}}_{y,i-\frac{1}{2},j,k-\frac{1}{2}}}{\Delta z}\right] \qquad (B.4)
\end{aligned}
$$

$$E^{n+1}_{y,i,j-\frac{1}{2},k} = \left[\frac{1-\dfrac{\sigma_{i,j-\frac{1}{2},k}\Delta t}{2\epsilon_{i,j-\frac{1}{2},k}}}{1+\dfrac{\sigma_{i,j-\frac{1}{2},k}\Delta t}{2\epsilon_{i,j-\frac{1}{2},k}}}\right] E^{n}_{y,i,j-\frac{1}{2},k} + \left[\frac{\dfrac{\Delta t}{\epsilon_{i,j-\frac{1}{2},k}}}{1+\dfrac{\sigma_{i,j-\frac{1}{2},k}\Delta t}{2\epsilon_{i,j-\frac{1}{2},k}}}\right]\left[\frac{H^{n+\frac{1}{2}}_{x,i,j-\frac{1}{2},k+\frac{1}{2}} - H^{n+\frac{1}{2}}_{x,i,j-\frac{1}{2},k-\frac{1}{2}}}{\Delta z} - \frac{H^{n+\frac{1}{2}}_{z,i+\frac{1}{2},j-\frac{1}{2},k} - H^{n+\frac{1}{2}}_{z,i-\frac{1}{2},j-\frac{1}{2},k}}{\Delta x}\right] \tag{$B.5$}$$

$$E^{n+1}_{z,i,j,k-\frac{1}{2}} = \left[\frac{1-\dfrac{\sigma_{i,j,k-\frac{1}{2}}\Delta t}{2\epsilon_{i,j,k-\frac{1}{2}}}}{1+\dfrac{\sigma_{i,j,k-\frac{1}{2}}\Delta t}{2\epsilon_{i,j,k-\frac{1}{2}}}}\right] E^{n}_{z,i,j,k-\frac{1}{2}} + \left[\frac{\dfrac{\Delta t}{\epsilon_{i,j,k-\frac{1}{2}}}}{1+\dfrac{\sigma_{i,j,k-\frac{1}{2}}\Delta t}{2\epsilon_{i,j,k-\frac{1}{2}}}}\right]\left[\frac{H^{n+\frac{1}{2}}_{y,i+\frac{1}{2},j,k-\frac{1}{2}} - H^{n+\frac{1}{2}}_{y,i-\frac{1}{2},j,k-\frac{1}{2}}}{\Delta x} - \frac{H^{n+\frac{1}{2}}_{x,i,j+\frac{1}{2},k-\frac{1}{2}} - H^{n+\frac{1}{2}}_{x,i,j-\frac{1}{2},k-\frac{1}{2}}}{\Delta y}\right] \tag{$B.6$}$$

The corresponding difference equations are referenced from [36].

APPENDIX C

DERIVATION OF EFFECTIVE CONDUCTIVITY FOR FDTD EQUATIONS AT DIELECTRIC INTERFACES

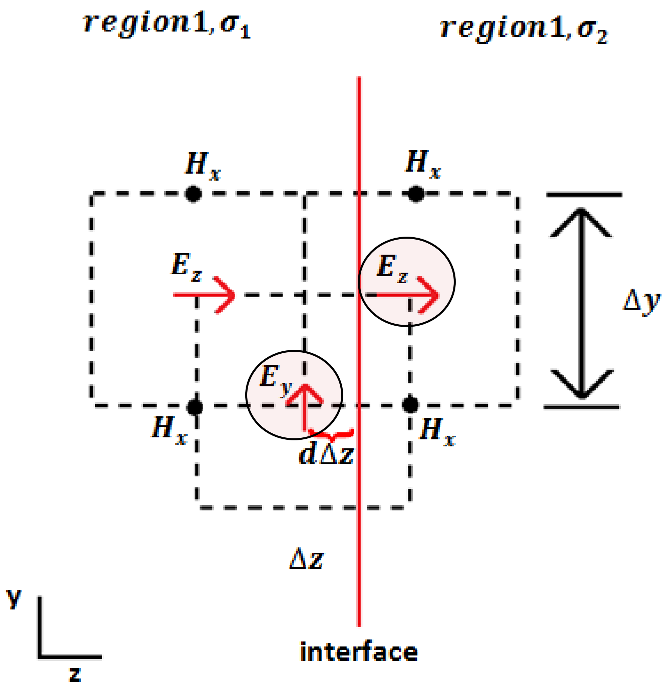

Figure C- 1 Placement of electric and magnetic field nodes near a dielectric interface for the case of 2-D $\mathbf{TE_x}$ polarization

The temporal approximation of the Ampere's law in integral form

$$\frac{\partial}{\partial t}\iint_S \boldsymbol{D}\cdot \boldsymbol{dS} = \oint_C \boldsymbol{H}\cdot \boldsymbol{dl} - \sigma \iint_S \boldsymbol{E}\cdot \boldsymbol{dS} \qquad (C.1)$$

yields when discretized in time

$$\iint_S \boldsymbol{D}^{n+1}\cdot \boldsymbol{dS} = \iint_S \boldsymbol{D}^{n}\cdot \boldsymbol{dS} + \Delta t \oint \boldsymbol{H}^{n+\frac{1}{2}}\cdot \boldsymbol{dl} - \sigma\Delta t \iint_S \boldsymbol{E}^{n+\frac{1}{2}}\cdot \boldsymbol{dl} \qquad (C.2)$$

For the tangential component of the electric field near the interface, shaded in Figure C- 1 with $'\mathrm{E_y}'$, discretization of the spatial integrals in *(B.2)* yields *(B.3)*. The fact that E_y is continuous at the interface and maintains the second-order spatial accuracy for its piecewise constant representation over each cell is used to obtain the corresponding equation.

$$\begin{aligned}
&\epsilon_1 E_{y,j,k}^{n+1}\left(\frac{1}{2}+d\right)\Delta z+\epsilon_2 E_{y,j,k}^{n+1}\left(\frac{1}{2}-d\right)\Delta z \\
&\qquad =\epsilon_1 E_{y,j,k}^{n}\left(\frac{1}{2}+d\right)\Delta z+\epsilon_2 E_{y,j,k}^{n}\left(\frac{1}{2}-d\right)\Delta z+\Delta t\left[H_{x,j,k+\frac{1}{2}}^{n+\frac{1}{2}}-H_{x,j,k-\frac{1}{2}}^{n+\frac{1}{2}}\right] \\
&\qquad -\sigma_1\Delta t\left(\frac{(E_{y,j,k}^{n+1}+E_{y,j,k}^{n})}{2}\right)\left(\frac{1}{2}+d\right)\Delta z \\
&\qquad -\sigma_2\Delta t\left(\frac{(E_{y,j,k}^{n+1}+E_{y,j,k}^{n})}{2}\right)\left(\frac{1}{2}-d\right)\Delta z \qquad (C.3)
\end{aligned}$$

Rearranging *(B.3)*, we obtain

$$\begin{aligned}
E_{y,j,k}^{n+1}=&\left[\frac{1-\Delta t\dfrac{\sigma_1\left(\frac{1}{2}+d\right)+\sigma_2\left(\frac{1}{2}-d\right)}{2[\epsilon_1\left(\frac{1}{2}+d\right)+\epsilon_2\left(\frac{1}{2}-d\right)]}}{1+\Delta t\dfrac{\sigma_1\left(\frac{1}{2}+d\right)+\sigma_2\left(\frac{1}{2}-d\right)}{2[\epsilon_1\left(\frac{1}{2}+d\right)+\epsilon_2\left(\frac{1}{2}-d\right)]}}\right]E_{y,j,k}^{n} \\
&+\frac{\dfrac{\Delta t}{\Delta z\left[\epsilon_1\left(\frac{1}{2}+d\right)+\epsilon_2\left(\frac{1}{2}-d\right)\right]}}{1+\Delta t\dfrac{\sigma_1\left(\frac{1}{2}+d\right)+\sigma_2\left(\frac{1}{2}-d\right)}{2[\epsilon_1\left(\frac{1}{2}+d\right)+\epsilon_2\left(\frac{1}{2}-d\right)]}}\left[H_{x,j,k+\frac{1}{2}}^{n+\frac{1}{2}}-H_{x,j,k-\frac{1}{2}}^{n+\frac{1}{2}}\right] \qquad (C.4)
\end{aligned}$$

If we equate *(B.4)* to 2D version of the finite difference equation of a standard cell given in *(B.5)*

$$E_{y,j,k}^{n+1}=\left[\frac{1-\left(\Delta t\dfrac{\sigma^*}{2\varepsilon^*}\right)}{1+\left(\Delta t\dfrac{\sigma^*}{2\varepsilon^*}\right)}\right]E_{y,j,k}^{n}+\left[\frac{\dfrac{\Delta t}{\varepsilon^*\Delta z}}{1+\Delta t\dfrac{\sigma^*}{2\epsilon^*}}\right]\left[H_{x,j,k+\frac{1}{2}}^{n+\frac{1}{2}}-H_{x,j,k-\frac{1}{2}}^{n+\frac{1}{2}}\right] \qquad (C.5)$$

the average conductivity and permittivity values to be used for tangential electric field components in the cells regarding the sheet's edge interfaces yields

$$\sigma^{*} = \sigma_1\left(\frac{1}{2}+d\right)+\sigma_2\left(\frac{1}{2}-d\right) \qquad (C.6a)$$

$$\varepsilon^{*} = \epsilon_1\left(\frac{1}{2}+d\right)+\epsilon_2\left(\frac{1}{2}-d\right) \qquad (C.6b)$$

For the normal components of the electric field at the sheet interface, while discretizing the spatial integrals given in *(B.1)*, the discontinuity of the normal electric field at the boundary should be taken into account. This inherent discontinuity leads the z-component of the electric field highlighted in Figure C- 1 to be written as

$$E_{z,j,k} = dE_{z1,j,k} + (1-d)E_{z2,j,k} \qquad (C.7)$$

where $E_{z1,j,k}$ and $E_{z2,j,k}$represent the average values of $E_{z,j,k}$ in the sub-cells in regions 1 and 2, respectively.

The difference equations for these sub-regions for the corresponding cell are:

$$E_{z,1,j,k}^{n+1}(d) = d\left[E_{z,1,j,k}^{n} - \frac{\Delta t}{\epsilon_1 \Delta y}\left[H_{x,j+\frac{1}{2},k}^{n+\frac{1}{2}} - H_{x,j-\frac{1}{2},k}^{n+\frac{1}{2}}\right] - \frac{\sigma_1}{\epsilon_1}\Delta t\left[\frac{(E_{z,1,j,k}^{n+1}+E_{z,1,j,k}^{n})}{2}\right]\right]$$

$$(C.8a)$$

$$E_{z,2,j,k}^{n+1}(1-d)$$
$$= (1-d)\left[E_{z,2,j,k}^{n} - \frac{\Delta t}{\epsilon_2 \Delta y}\left[H_{x,j+\frac{1}{2},k}^{n+\frac{1}{2}} - H_{x,j-\frac{1}{2},k}^{n+\frac{1}{2}}\right] - \frac{\sigma_2}{\epsilon_2}\Delta t\left[\frac{(E_{z,2,j,k}^{n+1}+E_{z,2,j,k}^{n})}{2}\right]\right]$$

$$(C.8b)$$

Rearranging *B.8a* and *B.8b*, yields

$$(d)E_{z,1,j,k}^{n+1} = d\frac{\left(1-\frac{\sigma_1\Delta t}{2\epsilon_1}\right)}{\left(1+\frac{\sigma_1\Delta t}{2\epsilon_1}\right)}E_{z,1,j,k}^{n} - d\left[\frac{\frac{\Delta t}{\epsilon_1\Delta y}}{\left(1+\frac{\sigma_1\Delta t}{2\epsilon_1}\right)}\left(H_{x,j+\frac{1}{2},k}^{n+\frac{1}{2}} - H_{x,j-\frac{1}{2},k}^{n+\frac{1}{2}}\right)\right] \qquad (C.9a)$$

$$\begin{aligned}(1-d)E_{z,2,j,k}^{n+1} = (1-d)&\frac{\left(1-\frac{\sigma_2\Delta t}{2\epsilon_2}\right)}{\left(1+\frac{\sigma_2\Delta t}{2\epsilon_2}\right)}E_{z,2,j,k}^{n} \\ &- (1-d)\left[\frac{\frac{\Delta t}{\epsilon_2\Delta y}}{\left(1+\frac{\sigma_2\Delta t}{2\epsilon_2}\right)}\left(H_{x,j+\frac{1}{2},k}^{n+\frac{1}{2}} - H_{x,j-\frac{1}{2},k}^{n+\frac{1}{2}}\right)\right] \qquad (C.9b)\end{aligned}$$

If we combine *B.9a* and *B.9b*, the normal component of the electric field yields:

$$\begin{aligned}E_{z,1,j,k}^{n+1} &= E_{z,1,j,k}^{n+1}(d) + E_{z,2,j,k}^{n+1}(1-d) \\ &= d\frac{\left(1-\frac{\sigma_1\Delta t}{2\epsilon_1}\right)}{\left(1+\frac{\sigma_1\Delta t}{2\epsilon_1}\right)}E_{z,1,j,k}^{n} + (1-d)\frac{\left(1-\frac{\sigma_2\Delta t}{2\epsilon_2}\right)}{\left(1+\frac{\sigma_2\Delta t}{2\epsilon_2}\right)}E_{z,2,j,k}^{n} \\ &\quad - \left(H_{x,j+\frac{1}{2},k}^{n+\frac{1}{2}} - H_{x,j-\frac{1}{2},k}^{n+\frac{1}{2}}\right)\left[d\frac{\frac{\Delta t}{\epsilon_1\Delta y}}{\left(1+\frac{\sigma_1\Delta t}{2\epsilon_1}\right)} + (1-d)\frac{\frac{\Delta t}{\epsilon_2\Delta y}}{\left(1+\frac{\sigma_2\Delta t}{2\epsilon_2}\right)}\right]\end{aligned}$$

$$(C.10)$$

If we equate (*B.10)* to 2D version of the finite difference equation of a standard cell given in *(B.5)*, which is:

$$\begin{aligned}E_{z,j,k}^{n+1} = &\left[\frac{1-\left(\Delta t\frac{\sigma^*}{2\varepsilon^*}\right)}{1+\left(\Delta t\frac{\sigma^*}{2\varepsilon^*}\right)}\right]\left(E_{z,1,j,k}^{n+1}(d) + E_{z,2,j,k}^{n+1}(1-d)\right) \\ &+ \left[\frac{\frac{\Delta t}{\varepsilon^*\Delta z}}{1+\Delta t\frac{\sigma^*}{2\epsilon^*}}\right]\left[H_{x,j+\frac{1}{2},k}^{n+\frac{1}{2}} - H_{x,j-\frac{1}{2},k}^{n+\frac{1}{2}}\right] \qquad (C.11)\end{aligned}$$

It is clear that it is not possible to define average permittivity and conductivity values for the normal component of the electric field regarding the cells located in the interface.

REFERENCES

[1] Paul Saville, “Review of Radar Absorbing Materials”, Technical Memorandum, Defence R&D Canada, January 2005.

[2] Cihangir Kemal Yuzcelik, “Radar Absorbing Material Design”, Msc. Thesis, Naval Postgraduate School, September 2003.

[3] William H. Emerson, “Electromagnetic Wave Absorbers and Anechoic Chambers Through the Years,” *IEEE Transactions on Antennas and Propagation*, Vol. 21, No. 4, pp. 484-490, July 1973.

[4] H. A. Tanner, US Patent 2977591, 1961.

[5] H. Nornikman, P.J Soh, A.A.H Azremi, M.S Anuar, “Performance Simulation of Pyramidal and Wedge Microwave Absorbers,” Third Asia International Conference on Modeling & Simulation, pp. 649-654, 2009.

[6] Brian T. Dewitt, Walter D. Burnside, “Electromagnetic Scattering by Pyramidal and Wedge Absorber,” *IEEE Transactions on. Antennas and Propagation*, Vol. 39, No. 7, pp. 971-984, July 1988.

[7] Halpern, O.; Johnson, M. H. J.; Wright, R. W., US Patent 2951247, 1960.

[8] Jones, A. R.; Wooding, E. R., “A Multi-Layer Microwave Absorber,” *IEEE Transactions on Antennas and Propagation*, Vol. 12, No. 4, pp. 508-509, July 1964.

[9] Salisbury, W. W., US Patent 2599944, 1952.

[10] Severin, H., “Nonreflecting Absorbers for Microwave Radiation”, *IRE Transactions on Antennas and Propagation*, Vol. 4, No. 3, pp. 385-392, 1956.

[11] Leendert J. du Toit, "The Design of Jaumann Absorbers," *IEEE Antennas and Propagation Magazine*, Vol. 36, No. 6, December 1994.

[12] Dallenbach, W.; Kleinsteuber, W. Hochfreq. u Elektroak 1938, 51, 152.

[13] John L. Wallace, "Broadband Magnetic Microwave Absorbers: Fundamental Limitations," *IEEE Transactions on Magnetics*, Vol. 29, No. 6, November 1993.

[14] Mayer, US Patent 5872534, 1999.

[15] Eugene F. Knott, John F. Schaeffer, Michael T. Tuley, Radar Cross Section, Artech House, 1st edition, United States of America, 1985.

[16] "Eccosorb NZ Thin Ferrite Absorber for 50 MHz to 15 GHz," Technical Bulletin 8-2-17, Emerson and Cuming, May 1979.

[17] M. B. Amin, and J. R. James, "Techniques for Utilization of Hexagonal Ferrites in Radar Absorbers, Part 1 Broadband Planar Coatings," The Radio and Electronic Engineer, Vol. 51, No. 5, pp. 209-218, May 1981.

[18] Alireza Kazem Zadeh, and Anders Karlsson, "Capacitive Circuit Method for Fast and Efficient Design of Wideband Radar Absorbers," *IEEE Transactions on Antennas and Propagation*, Vol. 57, No. 8, pp. 2307-2314, August 2009.

[19] Filippo Costa, Agostino Monorchio, and Giuliano Manara, "Analysis and Design of Ultra Thin Electromagnetic Absorbers Comprising Resistively Loaded High Impedance Surfaces," *IEEE Transactions on Antennas and Propagation*, Vol. 58, No. 5, pp. 1551-1558, 2010.

[20] Filippo Costa, Agostino Monorchio, and Giuliano Manara, "An Equivalent Circuit Model of Frequency Selective Surfaces Embedded within Dielectric Layers," *IEEE Antennas and Propagation Society International Symposium*, Charleston, US, 2009.

[21] Egemen Yildirim, Ozlem Aydin Civi, “Design of a wideband radar absorbing structure,” *Proceedings of the 5th European Conference on Antennas and Propagation (EUCAP)*, pp. 1324-1327, April 2011.

[22] David M. Pozar, Microwave Engineering, John Wiley & Sons Inc., 2nd Edition, United States of America, 1998.

[23] Online help of HFSS®, Technical notes on Units of Impedance Boundaries.

[24] N. Marcuwitz, Waveguide Handbook, Peter Peregrinus Ltd., December 1985.

[25] R. J. Langley and E. A. Parker, “Equivalent Circuit Model for Arrays of Square Loops,” *Electronics Letter*, Vol. 18, No. 7, pp. 294-296, April 1982.

[26] R. J. Langley and A. J. Drinkwater, "An Improved empirical model for the Jerusalem cross," *IEE Proceedings*, Vol. 129, No. 1, February 1982.

[27] R. 1. Langley and E. A. Parker, "Double-square frequency selective surfaces and their equivalent circuit," *Electronic Letters*, Vol. 19, No. 17, pp. 675-677, 1983.

[28] S. B. Savia and E. A. Parker, “Equivalent circuit model for super dense linear dipole FSS,” *IEEE Proceedings on Microwave and Antennas Propagation*, Vol. 150, No. 1, February, 2003.

[29] Luukkonen, Simovski, Granet and et al., “Simple and Accurate Analytical Model of Planar Grids and High-Impedance Surfaces Comprising Metal Strips or Patches,” *IEEE Transactions on Antennas and Propagation*, Vol. 56, No. 6, June, 2008.

[30] Ansoft HFSS®, <http://www.ansoft.com/products/hf/hfss/>.

[31] Zhongxiang Shen, Boyu Zheng, Zhilin Mei, Juan Yang and Wei Tang, “On the Design of Wide-band and Thin Absorbers Using the Multiple Resonances Concept,” *Proceedings of International Conference on Microwave and Millimeter Wave Technology*, Vol. 1, pp. 32-35, April 2008.

[32] Tao Wang, Yan Nie and Rongzhou Gong, "Synthesis Design of Metamaterial Absorbers Using a Genetic Algorithm," *Proceedings of International Symposium on Signals, Systems and Electronics*, Vol. 1, pp. 1-4, September 2010.

[33] Yahya Rahmat Samii and Eric Michielssen, Electromagnetic Optimization by Genetic Algorithm, Wiley-Interscience, July 1999.

[34] K.S. Yee, "Numerical solution of initial boundary value problems involving Maxwell's equations in isotropic media," *IEEE Transactions on Antennas and Propagation,* Vol. 14, 302-7, 1996.

[35] Matthew N. O. Sadiku, Numerical Techniques in Electromagnetics, CRC Press, 2nd Edition, USA, 2001.

[36] Fan Yang and Yahya Rahmat-Samii, Electromagnetic Bandgap Structures in Antenna Engineering, Cambridge University Press, 2nd Edition, October 2008.

[37] Allen Taflove and Susan C. Hagness, Computational Electromagnetics for RF and Microwave Engineering, Artech House, 2nd Edition.

[38] F. M. Tesche, "On the inclusion of loss in time-domain solutions of electromagnetic interaction problems," *IEEE Trans. Electromagn.Compat.,* Vol.32, pp. 1-4, Feb. 1990.

[39] Kyung Suk Oh, Jose E. Schutt-Aine, "An Efficient Implementation of Surface Impedance Boundary Conditions for the Finite-Difference Time-Domain Method," *IEEE Transactions on Antennas and Propagation,* Vol. 43, No. 7, July 1995.

[40] C. F. Lee, R. T. Shin, and J. A. Kong, "Time Domain Modeling of Impedance Boundary Condition," *IEEE Transactions on Microwave Theory and Techniques*, Vol. 40, No. 9, September 1992.

[41] Mikko K. Karkkainen, "FDTD Modeling of Arrays and Grids of Lossy Conductors Based on Impedance Sheet Conditions," *IEEE Transactions on Antennas and Propagation*, Vol. 52, No. 9, September 2004.

[42] J. H. Beggs, R. J. Luebbers, K. S. Yee, and K. S. Kunz, “Finite-difference time-domain implementation of surface impedance boundary conditions,” *IEEE Transactions on Antennas and Propagation*, Vol. 40, pp. 49-56, January 1992.

[43] Lin-Kin Wu, Liang-Tung Han, “Implementation and Application of Resistive Sheet Boundary Condition in the Finite-Difference Time-Domain Method,” *IEEE Transactions on Antennas and Propagation*, Vol. 40, No. 6, pp. 628-633, June 1992.

[44] J. G. Maloney, and G. S. Smith, “The Efficient Modeling of Thin Material Sheets in the Finite-Difference Time-Domain (FDTD) Method,” *IEEE Transactions on Antennas and Propagation*, Vol. 40, No.3, pp. 323-330, March 1992.

[45] Q. X. Chu, and H. Ding, “Second-Order Accurate FDTD Equations at Dielectric Interfaces,” *Microwave and Optical Technology Letters*, Vol. 49, No. 12, pp. 3007-3011, 19-22 December 2007.

[46] H. Ding, and Q. X. Chu, “An Improved Second-Order Accurate FDTD Equations at Dielectric Interfaces,” *Asia-Pacific Microwave Conf. Proc.* 5 (2005), 2870-2872.

[47] K. P. Hwang, and A. C. Cangellaris, “Effective Permittivites for Second-Order Accurate FDTD Equations at Dielectric Interfaces,” *IEEE Microwave and Wireless Components Letters*, Vol. 11, No. 4, pp. 158-160, April 2001.

[48] J. A. Roden, S. D. Gedney, M. P. Kesler, J. G. Maloney, and P. H. Harms, “Time-domain analysis of periodic structures at oblique incidence: orthogonal and nonorthogonal FDTD implementations,” *IEEE Transactions on Microwave Theory and Techniques*, Vol. 46, No. 4, 420-7, 1998.

[49] A. Aminian and Y. Rahmat-Samii, “Spectral FDTD: a novel computational technique for the analysis of periodic structures,” *IEEE APS Int. SYMP. Dis.*, Vol. 3, pp. 3139-3142, June 2004.

[50] F. Yang, J. Chen, R. Qiang, and A. Elsherbeni, “FDTD analysis of periodic structures at arbitrary incidence angles: a simple and efficient implementation of the periodic boundary conditions," *IEEE APS Int. SYMP. Dis.*, Vol. 3, pp. 2715-2718, 2006.

[51] B. Engquist, and A. Majda, "Absorbing boundary conditions for the numerical simulations of waves," *Math. Comput*, Vol. 31, 629-51, 1977.

[52] G. Mur, "Absorbing boundary conditions for the finite difference approximation of the time-domain electromagnetic field equations," *IEEE Transactions on Electromagnetic Compatibility*, Vol. 23, pp. 377-382, 1981.

[53] J. P. Berenger, "A perfectly matched layer for the absorption of electromagnetic waves," *J. Computational Physics*, Vol. 114, pp. 185-200, 1994.

[54] S. D. Gedney, "An anisotropic PML absorbing media for FDTD simulation of fields in lossy dispersive media," *Electromagnetics*, Vol. 16, pp. 399-415, 1996.

[55] Rohacell HF product information, <http://www.rohacell.com/sites/dc/Downloadcenter/Evonik/Product/ROHACELL/product-information/ROHACELL%20HF%20Product%20Information.pdf>, last accessed on 21/11/2011.

[56] S. A. Tretyakov, Analytical Modeling in Applied Electromagnetics, Norwood, MA: Artech House, 2003.

[57] Agilent Technoloies, <http://www.agilent.com/>, last accessed on 16/02/2012.

[58] D. Rytting, "Let time domain response provide additional insight into network behaviour," *RF & Microwave Measurement Symposium and Exhibition*.